TEXTURAL AND GEOCHEMICAL INVESTIGATION OF THE PEACH SPRING TUFF CA-NV-AZ, USA: EVIDENCE FOR DYNAMIC PRE-SUPERERUPTION PROCESSES

By

Michelle Lee Foley

Thesis

Submitted to the Faculty of the

Graduate School of Vanderbilt University

in partial fulfillment of the requirements for

the degree of

MASTER OF SCIENCE

in

Earth and Environmental Sciences

August 11, 2017

Nashville, Tennessee

Approved:

Calvin F. Miller, Ph.D.

Guilherme A.R. Gualda, Ph.D.

“Test ideas by experiment
and observation. Build on those ideas that
pass the test, reject the ones that fail. Follow the
evidence wherever it leads, and question
everything.”
- Neil deGrasse Tyson

ACKNOWLEDGEMENTS

I have to begin by thanking my undergraduate advisor, Andrew H. Wulff, for giving me the encouragement and tools necessary to become a geologist and prolific researcher. I have to thank the Vanderbilt REU: Before and After a Supereruption and the numerous, marvelous – but often bizarre - people involved for without that experience, I would obviously not be where I am today. With that, I owe a special gratitude to Charles Ferguson for the unforgettable field excursions and the generous input on this thesis. I have to especially thank the VU EES department including graduate students, faculty, staff (Jewell Beasley-Stanley), and undergraduates for the countless memorable experiences I've had during my Masters journey. I thank my committee members Calvin Miller, Guil Gualda, and Simon A.F. Darroch for the often convoluted but spirited guidance. I am forever in debt to Calvin Miller for the time spent guiding me through my Masters career, whose insight extends far beyond that of academics, and who never ceases to amaze me. I also owe a big thank you to Guil Gualda for including this lonely outsider within the Gualda exclusive Hummus Pummus group and for the infinite amount of knowledge and time you have lent to me. I thank all the members of the MESSY! research group for the countless interesting and valuable conversations. I thank Aaron Covey and Richard Bradshaw for their substantial lab assistance. I owe a special thanks to the rock stars Brandt Gibson, Izzy Weisman, Brooke Patton and Rachel Shumaker for keeping me (more or less) sane during these past two year. And lastly, I must thank my parents and family for providing me with the opportunity to study what I am passionate about and the continuous support.

Funding for this project was provided by NSF grants EAR-0911726 and EAR-1263310, as well as Vanderbilt University.

TABLE OF CONTENTS

Page

LIST OF TABLES

LIST OF FIGURES

CHAPTER 1

INTRODUCTION

1.1 Overview

Considerable scientific interest in recent decades has centered on what have been called supereruptions (defined as explosive eruptions that yield >450 km^3 of pyroclastic material [in dense rock equivalent, DRE]; Rampino and Self 1992; Sparks et al., 2005; Miller & Wark, 2008). Investigations of supereruption products have demonstrated the variability within products of single eruptions as well as from eruption to eruption. Diverging views on the origins of these giant eruptions and the processes that they reflect have emerged from these studies. Specific questions that are critical for this thesis include: (1) How do the eruptions and systems that produce super-sized deposits work? (2) What is the nature in space and time of the systems from which they erupt? And (3) what dynamic processes are implied by the answers to questions (1) and (2)?

In detail, nearly every eruptive product is different, but broadly speaking the deposits show a dichotomy between being relatively unzoned, crystal-poor and fairly homogeneous (e.g. Taupo Volcanic Zone, Wilson, 2008) and quite variable, with well-defined zonation (compositionally and thermally) stratigraphically as well as temporally (e.g. Bishop Tuff, Hildreth & Wilson, 2007; Ammonia Tanks Tuff, Deering et al., 2011; Bandelier Tuff, Wolff & Ramos, 2003). Another important subgroup of unzoned deposits includes the "monotonous intermediates" (relatively unzoned ignimbrites of crystal-rich dacite - up to 45% vol crystals; Hildreth, 1981) whose eruptibility should be inhibited by the high fraction of solid particles and

high effective viscosity. Of particular relevance to this study are those eruptions that have compositionally distinct early-erupted, crystal poor and highly silicic tuff and late-erupted crystal-rich and less silicic tuff. What is to be determined is what does the deposit zonation (compositionally, thermally, and crystal fraction) say about the organization of and processes within the magma body (or bodies) that fed the eruption.

Common silicic, crystal-poor deposits clearly suggest that extraction of large quantities of highly silicic, viscous melt happens. Determining the processes governing the formation of these large evolved silicic melts in the shallow crust and how they relate to their later erupted crystal rich less silicic erupted counterpart has important implications for understanding crustal evolution as well as determining the potential hazards that these eruptions pose. Several chemical indicators hint that the contrasting deposits are related – at least in part – by crystal-liquid fractionation within the magma chamber (*in situ* differentiation; Hildreth, 1981, 2004; Bachmann & Bergantz, 2008a).

One model that accounts for large volumes of crystal-poor melt generated on geologically relevant timescales is the mush model of Bachmann & Bergantz (2004). The model posits a lens of crystal-poor melt underlain by a bed of cognate crystals, or cumulate (Hildreth, 2004; Wolff et al., 2015) (**Figure 1A**). In situ crystal-liquid separation occurs most efficiently at an intermediate crystal fraction stage (~45-65% crystals). These intermediate crystal fraction conditions favor processes of hindered settling, microsettling, and/or high permeability compaction to extract crystal-poor and highly evolved melts from the relatively high permeability crystal mush zones (Bachmann & Bergantz, 2004).

This simple, single chamber geometry for the mush model arose post the "Big Tank" magma chamber model, envisioned for the example of Long Valley, California in the early

1980s. Since then, a range of magma reservoir geometries and histories have been proposed; a currently popular "complex magma reservoir" is imagined where multiple discrete magma lenses are tapped during a single eruption (Cooper et al., 2012; Cashman & Giordano, 2014; Gualda & Ghiorso, 2013) (**Figure 1B**). Determining the shape, size, and state of magma bodies in the Earth's crust remains a key topic for investigation. There is now a general consensus that magma reservoirs (or chambers, or bodies) comprise rheologically distinct materials including melt-rich magma; crystal mush (barely eruptible, up to 50-60% crystals); immobile and uneruptable , crystal-rich "rigid sponge;" and rock (e.g. Hildreth, 2004). Considerable uncertainty remains regarding the distribution of these materials in space and time (Fig. 1; cf. Miller, 2016).

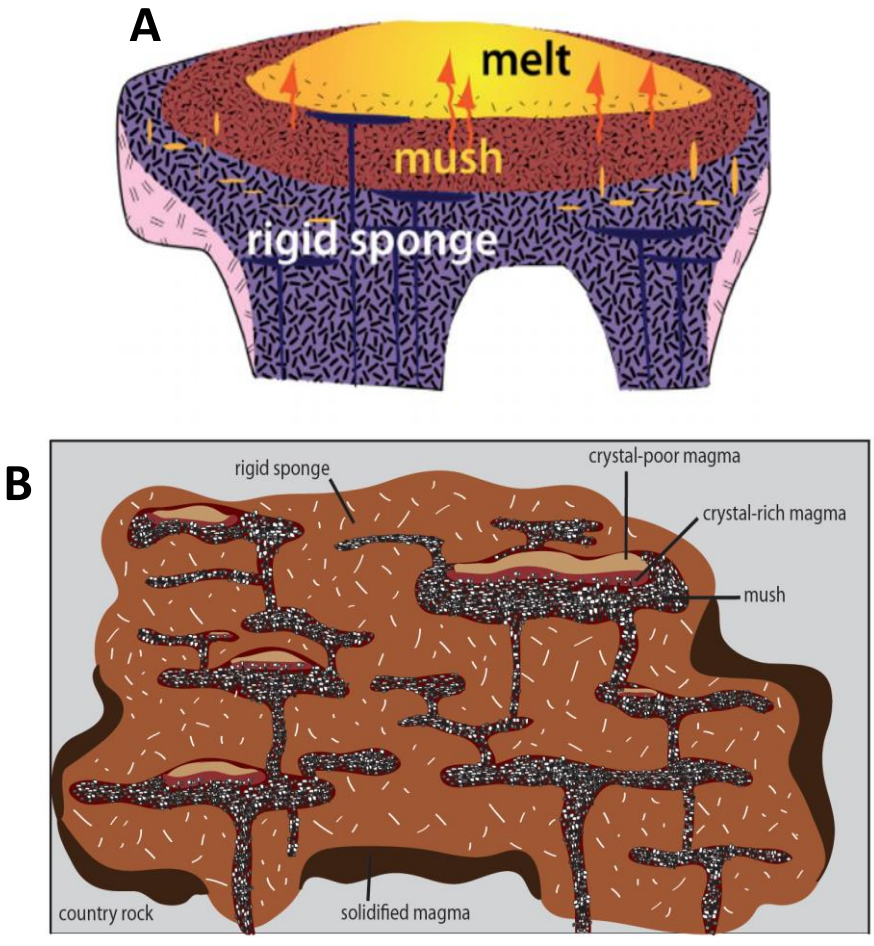

Figure 1. (A) Simple, single chamber model; taken from Cashman & Giordano (2014), modified from Hildreth (2004). A lens of crystal poor melt (<~15% crystals) forms over the mush, constituting ~50-60% crystals, which grades into rigid sponge (~60-100% crystals). (B) Complex magma reservoir; the distribution of rheologically different material varies across space and time; modified from Cashman & Giordano (2014).

Reservoir geometry is particularly important when determining the potential hazard of the magma reservoir and its likelihood of eruption. The distribution of eruptible magma, which includes both crystal-poor, melt-rich material and crystal mush, is likely to vary in distribution in space and time. An important focus of this thesis will be to consider the processes that can lead to the formation of a substantial volume of eruptible magma in shallow chambers that feed eruptions. The duration of construction and crystal fractions at any given time remain controversial and likely vary across different volcanic settings. Broadly speaking, these issues divide adversaries into two camps: those who advocate "cold-storage" versus those who favor "warm-storage". Cold-storage advocates suggest that magma systems spend much of their thermal lifetime in a crystal-rich, even subsolidus, and ineruptible state - backed by U-series dating and diffusion profile and crystal-size distribution modeling (e.g. Cooper and Kent, 2014; Cooper, 2017). In contrast, warm-storage advocates suggest eruptible magma is stored beneath a volcano for much of its lifetime ($> 10^5$ y), which is supported by prolonged records of zircon growth (e.g. U-Pb and U-series dating; Barboni et al., 2016). While the lifetime at any given physical state of a given chamber remains unclear, magmatic replenishment has been proposed as the main mechanism for sustained lifetimes of these systems, as well as an eruption promoting mechanism.

A recharge event - injection of new magma into the system - can add mass and thermal energy. The added heat may induce partial dissolution of crystals in the resident magma, thus reducing its crystal fraction and strength and resulting in rejuvenation. The effect that such an event will have on an existing magma body will be a function of the current state of the resident magma (e.g. crystal fraction, location/depth in the crust) and of the properties of the invading recharge (e.g. composition, temperature). The energy provided by replenishment is

crucial in sustaining systems that would otherwise be short-lived in the upper crust due to loss of heat and potentially in rejuvenating moribund magma bodies (Koyaguchi & Kaneko, 2000).

Many large silicic eruptions show evidence for triggering by intrusion of hotter, more mafic magma (e.g. Sparks et al., 1977; Pallister et al., 1992; Bachmann & Bergantz, 2003; Bindeman & Valley, 2003; Kennedy & Stix, 2007). Evidence for reheating is apparent in the erupted produced where phenocrysts exhibit textures of partial dissolution (e.g. Carpenter Ridge Tuff, CO; Bachmann et al., 2014; Ammonia Tanks Tuff; Deering et al. 2011). Rejuvenation as a result of recharging events can lead to a reduction in the crystal fraction below the mechanical lock point and effectively increase the internal overpressure; thermo-mechanical reactivation may be particularly important in eruption of "monotonous intermediates," (e.g. Fish Canyon Tuff, Bachmann et al., 2002; Masonic Park Tuff, Sliwinski et al., 2017). Ultimately, understanding the thermo-mechanical behavior of magmas in large upper crustal reservoirs is important for evaluating eruption potential and triggering mechanisms for these large superbodies and the timescales associated with rejuvenation events.

1.2 Geological Background

The Peach Spring Tuff (PST) is a supereruption sized pyroclastic deposit located in the southwestern USA. The outflow sheet extends across southern Nevada, southeastern California, and northwestern Arizona, covering an area of ~32,000 km^2 (**Figure 2**); its lateral extent made it the key stratigraphic marker for the Colorado River and Central Mojave extensional terrain (Buesch 1992; Glazner et al., 1986). Buesch (1992) estimated that the PST outflow had a

volume at least 640 km^3 (DRE), making it by far the largest eruption within the Northern Colorado River extensional corridor.

The location of the caldera was constrained to be in the vicinity of the CA-AZ-NV intersection based on a number of early studies (e.g. Hillhouse & Wells, 1991), but the caldera was not identified until recently. During mapping in the Black Mountains, Arizona, Ferguson identified a large portion of the source of the PST, the Silver Creek caldera, and later discovered a second, smaller, tectonically transported fragment in the Sacramento Mountains, California (Ferguson 2008; Ferguson et al., 2013). The outflow sheet is estimated to have traveled more than 170 km (corrected for post-eruption extension) away from the source caldera (AZ, USA) (Glazner et al., 1986; Ferguson et al., 2013; cf. Roche et al., 2016).

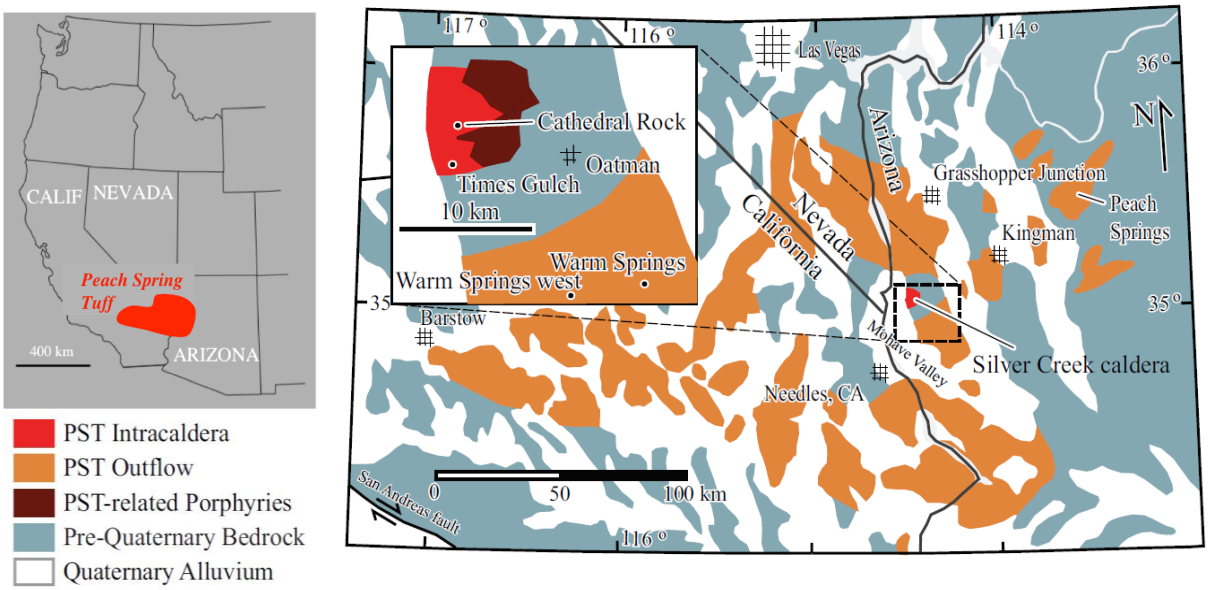

Figure 2. (top left) outflow areal extent mark of the Peach Spring Tuff. (top right) Generalized geologic map showing the outflow area covered by the associated volcanic units of the Peach Spring Tuff; insert map shows source Silver Creek caldera and intracaldera volcanics.

The eruption was established as Early Miocene in age by initial studies (e.g. Glazner et al., 1986; Young & Brennan, 1974) and dated at ca. 18.5 Ma by Nielson et al. (1990) using the sanidine $^{40}Ar/^{39}Ar$ dating technique. Ferguson et al. (2013) determined a more precise age of 18.78 ±0.02 Ma (the older age is a result of the revised age for the Fish Canyon sanidine flux monitor and is consistent with the results of Nielson et al.,1990). The outflow has generally been considered to comprise a single cooling unit (e.g. Young & Brennan, 1974; Glazner et al., 1986; Buesch & Valentine, 1986; Buesch, 1992). Varga et al. (2004), however, have suggested that there are two distinct, locally discernible cooling units in PST sequences in the Black Mountains.

Pamukcu et al. (2013) show that the PST is chemically and thermally zoned, where the predominant outflow consists of an earlier erupted phenocryst-poor, high-silica rhyolite and the caldera fill is phenocryst-rich trachyte. Textural evidence including resorption features on phenocrysts and Ti-rich rims of zircon crystals indicated the intracaldera trachyte was affected by a late-stage heating event; Pamukcu et al (2013) speculate that trachyte represents cumulate material, and that the heating event remobilized this cumulate and may have triggered the eruption (Pamukcu et al.. 2013). The PST itself is relatively uniform in isotopic compositions of both whole rocks and zircons across the trachyte-to-high-silica rhyolite range of elemental compositions, particularly when compared to other units within the Colorado River Extensional Corridor (McDowell et al., 2016).

Ferguson & Cook (2015) distinguished four zones, Tp1-4, of the Peach Spring ignimbrite where it is well exposed in the Kingman, AZ, area in sections that reach 100 m in thickness (**Figure 3**). In some locations, a well-developed black vitrophyre occurs very close to the basal contact of the lowest welded zone (Ferguson & Cook's Sawmill zone, Tp3). Overall the lower four zones are phenocryst-poor (2-15%); there is an upward trend of increasing phenocryst

content from base to top in the full section recorded for the bulk tuff (Ferguson et al., 2013). The lower four zones contain phenocrysts of sanidine, plagioclase, very sparse quartz, amphibole, biotite, relatively abundant sphene (titanite), and other accessories (magnetite, ilmenite, allanite, chevkinite, apatite, zircon).

The fifth and uppermost zone of the PST, the Warm Spring Zone (WSZ, Tp5), is named for its most complete known exposure in the Warm Springs Wilderness, southern Black Mountains. The transition into this zone is marked where phenocryst content reaches >~35% modally in the bulk tuff and pumice/fiamme. The increase in phenocryst content occurs rapidly across the contact, accompanied by an abrupt increase in welding from poorly to non-welded Hilltop (Tp4) into densely-welded with a central vitrophyre horizon present in some outcrops. This transition also marks a chemical distinction, with rhyolite below and trachyte above (Foley et al., 2014). Tp5 is very similar in composition, texture, and phenocryst content (~>35%) to the intracaldera trachyte.

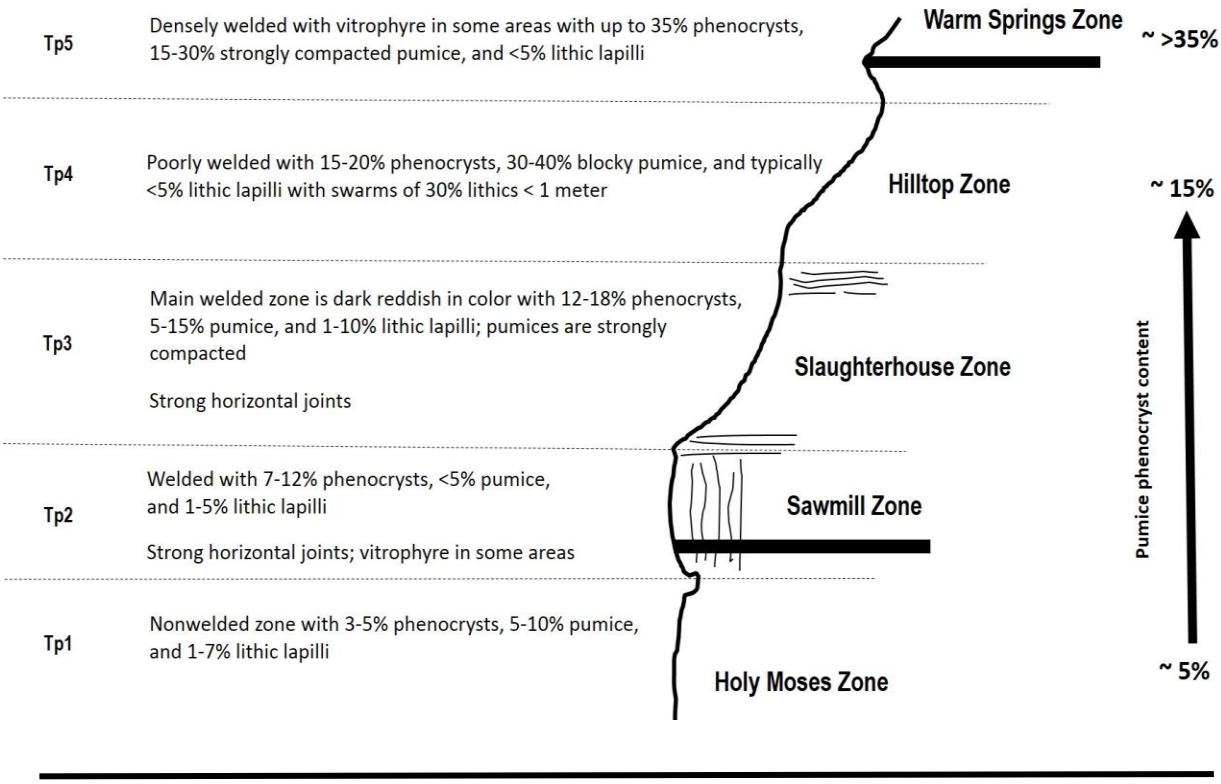

Figure 3. Generalized stratigraphy of the five zones of Peach Spring Tuff zones as defined by Ferguson & Cook (2015). Two vitrophyre are discernable in some locations within the Sawmill and Warm Springs Zone. Pumice phenocryst content increase upward through the lower four and then an abrupt increase occurs at the transition into the Warm Springs Zone.

1.3 Thesis Focus

In suggesting the possibility that intracaldera PST trachyte may represent a basal chamber cumulate, remobilized by a heating event that may have triggered the eruption, Pamukcu et al., (2013) laid the groundwork for this investigation. The recognition that trachytic pumice and fiamme similar to the intracaldera material, though volumetrically very minor, are present and commonly very fresh and unaltered in the outflow (Foley et al., 2014), suggested that continued study was potentially fruitful. This thesis presents the first detailed field, petrological, and geochemical characterization of the crystal-rich pumice and fiamme from the outflow of the PST and expands upon the existing data set for the more typical outflow rhyolite and intracaldera trachyte. Through this study I aim to assess the processes that formed and modified the late-erupted, crystal-rich PST material and to determine how it relates to the magma chamber processes that preceded the eruption.

Key questions I aimed to address are:

1. What processes formed and modified the cumulate of PST?

2. How diverse in texture, composition, and phase composition are the crystal-rich Tp5 type pumice and fiamme?

3. What were the pre-eruptive conditions?

4. How does the Tp5 (± intracaldera) compare to the high-silica rhyolite (Tp1-Tp4) PST?

And, more generally:

5. What can I say about the PST with respect to these processes and how does it compare to other super-eruptive systems?

CHAPTER 2

SAMPLING AND METHODS

2.1 Field Sites

We collected most samples from localities proximal to the source of PST, Silver Creek caldera (**Figure 4**). We focused on Tp5, the only part of the outflow that is trachytic in bulk composition and with pumice and fiamme populations dominated by trachyte. Tp5 has only been identified within 30 km of the caldera. In contrast, rhyolite outflow extends 250 km to the west (present day, post extension). The volume of this capping unit is estimated to constitute only ~1% of the entire erupted outflow (Ferguson, 2016).

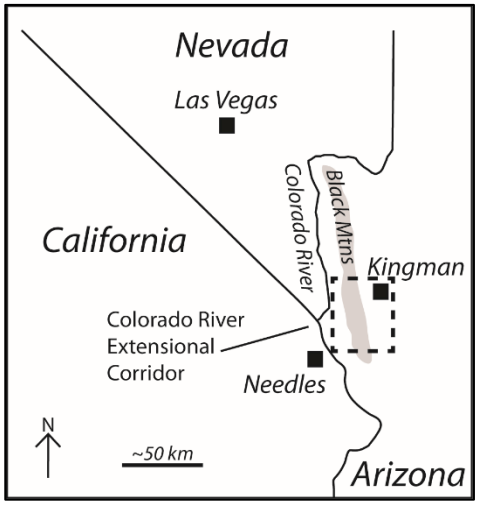

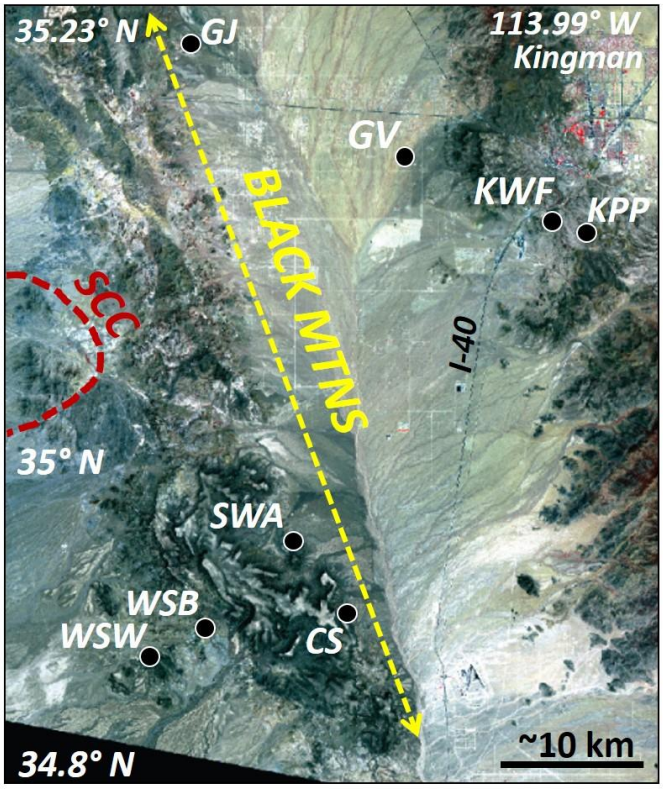

Figure 4. (top) Southern Black Mountains are located within the Northern Colorado River Extensional Corridor; dashed outline corresponds to sample locator map. (right) Locations for all samples analyzed in this study and a list of abbreviated names can be found in Table 1. A list of every sample name and location collected in this study is found in **Appendix A**.

The best preserved full section of the entire proximal outflow PST sheet is located at Warm Springs Butte (WSB) in the southern Black Mountains (**Figure 5a**); half of the samples for this study are from this location. The entire section of PST at WSB is 140 m (Ferguson et al., 2013). The five zones established by Ferguson & Cook (2015) in the Kingman area appear to be present at this location, but a very thick middle section is obscured by intense vapor phase alteration and largely inaccessible because it is mostly exposed in vertical cliffs. We infer that this portion of the section includes Tp3, much of Tp2, and possibly the lower Tp1. Much of what we interpret to be Tp4 is well exposed as weakly to non-welded rhyolitic tuff. The section is capped by approximately 30 m of strongly, mostly orange Tp5 with a prominent black vitrophyre horizon. The original contact between Tp5 and Tp4 is lost due to faulting at the

location where samples were collected, but it appears to be preserved elsewhere on the butte within un-faulted sections (**Figure 5b, c**).

The Tp4-Tp5 contact is well exposed 3.5 km to the west at in the Warm Springs West area (**Figure 5d**). Here, the contact appears to be gradational over a few meters, from pale-gray, non-welded tuff with uncompressed pumice to welded, orange tuff. As at WSB, the orange welded tuff grades rapidly into black vitrophyre. We interpret the gradational contact with rapid increase in welding to indicate that a very hot Tp5 pyroclastic density current (PDC) was deposited atop already partially cooled Tp4 tuff, which represented the top of what was probably a single massive PDC (Roche et al., 2016). The Tp5-Tp4 contact likely marks a short hiatus between the eruption of the dominant outflow zone (the lower four zones of the PST) and emplacement of the upper, capping Tp5.

An isolated, fault-bounded exposure of Tp5 is present in Golden Valley (GV), northwest of Kingman (Ferguson, 2016; Barry et al., 2015). The black trachyte vitrophyre is well exposed here.

At some other proximal exposures of PST, sparse trachytic and similar low-silica rhyolite (LSR) pumice and fiamme are present in lower zones of rhyolitic tuff, along with typical high-silica rhyolite (HSR) pumice (locations GJ [Grasshopper Junction Quad], SWA [northeastern Warm Springs Wilderness], CS [Caliche Spring], KP [south of Kingman]). At Caliche Spring, trachyte pumice is present in what appears to be uppermost Tp4, but there is no evidence of increased welding that would suggest the presence of an overlying Tp5.

Typical high-silica rhyolite (HSR) pumice and fiamme samples were collected from two locations. The Kingman Wind Farm (KWF) samples were included in this study to look at changes in phenocryst content and geochemical signatures within pumice and fiamme for the

lower four PST zones. The section at KWF is much thinner than typical outflow for the Kingman, AZ area (as little as 20 m), resulting from deposition over a high point in paleotopography. The lower four zones are all exposed but very thin at KWF (Ferguson & Cook, 2015); vapor phase alteration and welding are consequently less intense than elsewhere. Phenocryst abundance in pumice increases upwards in section, from ~5% in the lowermost Tp1 zone to ~15% within Tp4.

Geochemical analyses and sample descriptions for this study were based predominantly on fiamme or pumice, because pumice and fiamme provide the most reliable information on magma chemistry and textures. In hand samples, Tp5 pumice are often tan-orange and crystal-rich (~35%) - a stark contrast when compared to the crystal-poor (~2-15%) typical white or gray of the high-silica rhyolite pumice. For a hand sample description samples in **Table 1, see Appendix B**.

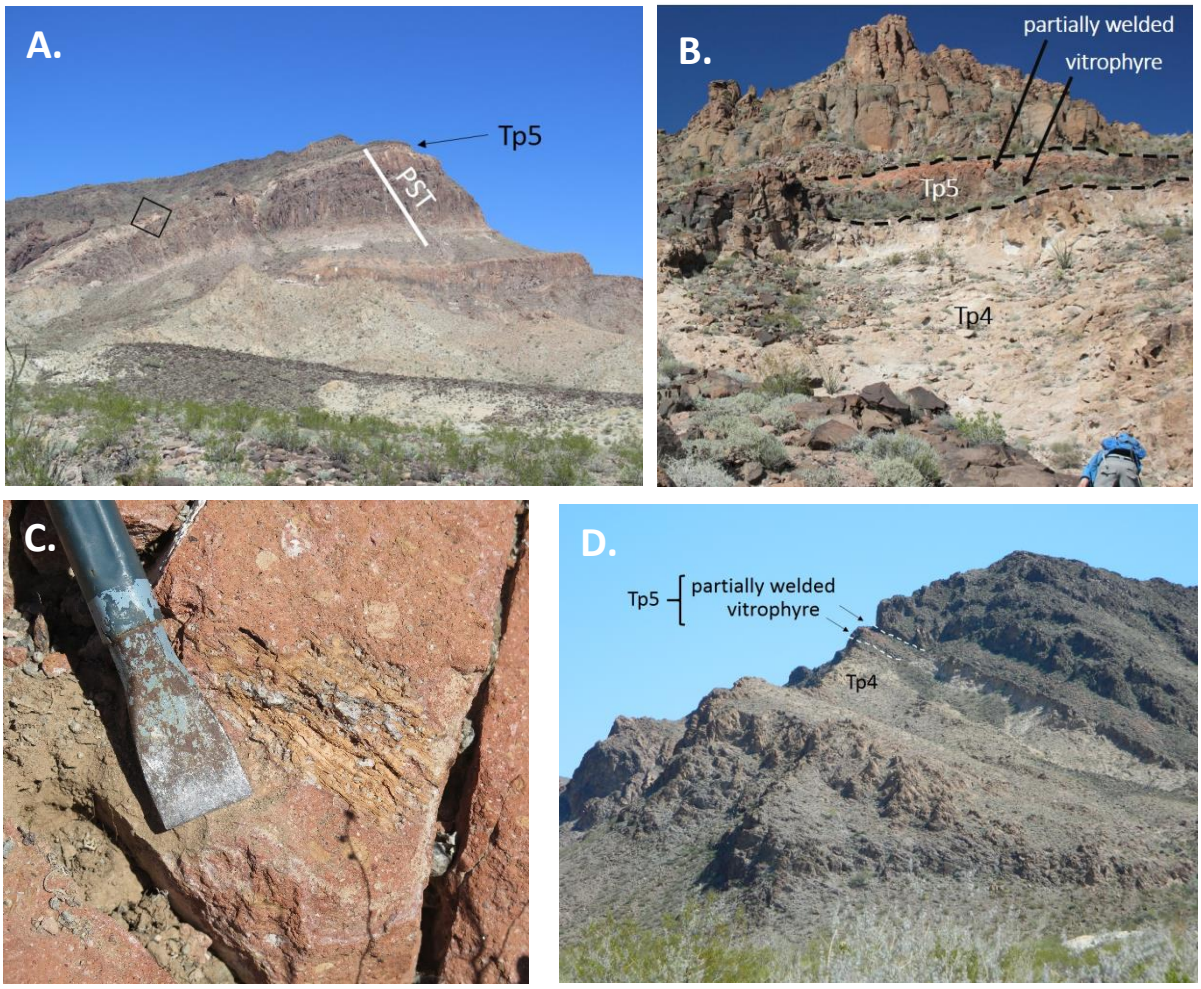

Figure 5. (A) PST section at Warm Springs Butte; black outlined box corresponds to image B; (B) the contact between Tp5 and Tp4 at WSB; a central vitrophyre horizon is present; (C) Tp5 crystal-rich pumice at WSB section; (D) The original depositional contact between Tp4 and Tp5 is visible at Warm Springs West.

Table 1

Sample Name	Map location name	Map Unit (Ferguson & Cook 2015)	Easting	Northing	Sample Type	Analyses performed
WSB Fo 1	Warm Springs Butte	Tp5	0744321	3865844	fiamme	t, s, x, l
WSB Fo 3	Warm Springs Butte	Tp5	0744314	3865777	fiamme	t, s, x, l
WSB Fo 3b	Warm Springs Butte	Tp5	0744314	3865777	fiamme	t, s, x, l
WSB Fo 7	Warm Springs Butte	Tp5	0744314	3865919	vitrophyre	t, s, x,
WSB Fo 8	Warm Springs Butte	Tp5	0744327	3865824	fiamme	t, s, x,
WSB Fo 20	Warm Springs Butte	Tp5	0744300	3865830	fiamme	t, s, x, l
WSB Fo 23	Warm Springs Butte	Tp5	0744331	3865815	fiamme	t, s, x, l
WSB Fo 27	Warm Springs Butte	Tp4	0744237	3865851	pumice	pc, t, s, x
WSB Fo 28	Warm Springs Butte	Tp5	0744233	3865884	bulk tuff	t, x
WSB Fo 29	Warm Springs Butte	Tp5	0744233	3865884	bulk tuff	t, x
WSB Fo 31	Warm Springs Butte	Tp5	0744328	3865934	fiamme	t, s
CS Fo 1	Caliche Spring	-	0753916	3867319	pumice	t, s
CS Fo 4	Caliche Spring	-	0753916	3867319	pumice	t, s
CS Fo 6	Caliche Spring	-	0753916	3867319	pumice	t, s
KPP MF 2	Kingman Property	Tp3	0773097	3892663	pumice	pc, t, s, x
KPP MF 5	Kingman Property	Tp3	0773092	3892663	pumice	pc, t, s, x
GJ Fo 1	Grasshopper Junction	-	0739594	3905378	vitrophyre	t, s, x, l
GJ Fo 2	Grasshopper Junction	-	0739609	3905153	bulk tuff with fiamme	t, x
SWA Fo 1A	Warm Springs Wilderness	-	0749241	3873031	pumice	pc, t, x
KWF Fo 1E	Kingman Wind Farm	Tp1	0766601	3893556	pumice	pc, t, s, x, l
KWF Fo 2A	Kingman Wind Farm	Tp2	0766755	3893404	pumice	pc, t, s, x, l
KWF Fo 3B	Kingman Wind Farm	Tp2	0766755	3893404	bulk tuff with fiamme	t, s, x, l
KWF Fo 4	Kingman Wind Farm	Tp2	0766755	3893404	vitrophyre	t, x
KWF Fo 5	Kingman Wind Farm	Tp4	0766731	3893434	pumice	t, s, x
KWF Fo 10	Kingman Wind Farm	Tp3	0767507	3894356	pumice	pc, t, s, x
PSTSWA01A*	Warm Springs Wilderness	-	0749409	3872740	pumice	t, s, x, l
MLPT 5D*	Caliche Springs	-	0753850	3867388	pumice	t, s, x, l
28556-P1*	Warm Springs Butte	-	0744123	3865671	pumice	t, s, x, l

Table 1. UTM coordinates are in 11S, NAD 83. PST zones are listed where locations have been professionally mapped and assigned. *pc* – pumice cleaning; *t* – thin section; *s* – SEM analyses; *x* – whole-rock analyses; *l* – LA-ICPMS glass analyses. All samples collected for this study and locations can be found in **Appendix A**.

2.2 Analytical Methods

We chose representative samples from each locality for petrographic inspection and geochemical analysis. A summary of analytical methods for each sample is listed in **Table 1**. Phenocryst assemblages were determined by optical microscopy of thin sections and electron microscopy. Twenty total pumice and fiamme samples were selected for whole-rock compositional analysis. Eight pumice were crushed using agate mortar and pestle and cleaned prior to analysis using three successive ultrasonic baths: deionized water, 0.1 M HCl with 2% H_2O_2, and deionized water. We assumed that porosity was reduced sufficiently by welding of the twelve fiamme samples to minimize secondary alteration, so these samples were not cleaned.

Samples chosen for whole-rock analysis were sent to Activation Laboratories (Canada) for major and trace elements analysis. Elemental abundances were measured using a combination of fusion inductively coupled plasma mass spectrometry (FUS-ICP-MS), total digestion ICP (TD-ICP), and instrumental neutron activation analysis (INAA). New analyses from this study were combined with the preexisting PST data set compiled by Frazier (2013). Samples analyzed for this study include eight high-silica rhyolites and twelve trachytes. Analyses are predominantly of pumice and fiamme, but seven are bulk tuff samples. Bulk whole-rock tuff samples were analyzed where fiamme and pumice were not discernable or large enough for individual analyses; sample types are marked in **Table 1.**

Major element compositions of glasses and phenocryst phases were measured at Vanderbilt University using an Oxford X-max 50-mm2 EDS attached to a Tescan Vega 3 LM Variable Pressure SEM. An accelerating voltage of 15-16 kV and specimen current of

~$1*10^{-9}$ was used for SEM analyses. The RGM-1 USGS rhyolite glass standard was used as a secondary standard for all analyses. The SPI #02753-AB mineral standards were used as secondary standards for analyses of minerals.

Trace element concentrations for glasses were measured by laser ablation ICP-MS at Vanderbilt University, using a Photon Machines Excite 193 nm excimer laser and Thermo iCAP Q quadrupole ICP-MS. For each analysis, a 50 x 50 μm square laser spot size is ablated for 30 s at a pulse frequency of 10 Hz. NIST 610 is used as the primary standard and NIST 612 and RGM-1 are used as secondary standards. ^{28}Si is used as an internal standard, using average sample SiO_2 contents as determined for each sample by SEM-EDS analysis prior to trace element collection. In samples where multiple composition domains are identified within a sample, the average SiO_2 concentration within each domain is used as the internal standard.

A table of example SEM-EDS RMG-1 standard glass analyses, SPI #02753-AB mineral standard analyses for minerals also present in the PST, and example NIST 610, NIST 612, and RGM-1 laser ablation ICP-MS concentrations can be found in **Appendix C**.

2.3 Diffusion Timescales

2.3.1 Silicate Diffusion

The diffusion between two glasses in contact can be used to constrain the timescales of magma mingling. For diffusion of major elements, only one element is necessary to calculate diffusion timescale lengths since net diffusion is set by the slowest diffuser (Baker 1990). Experimentally determined silicon diffusivities are utilized in diffusion calculations for this study.

2.3.2 Diffusion Coefficient

Though silicon diffusion in the melt varies as a function of composition, this variability is relatively small according to the experimental results of Baker (1991). For simplicity, this minor variability can be neglected and diffusivity can be treated as a constant. The Arrhenius equation that I use for diffusion calculations was taken from Baker (1991), based on similarity in conditions and melt compositions in this study to those in PST. The equation used was calculated for experimental glasses with starting compositions of 65 and 75 wt % SiO_2. At 70 wt % SiO_2, 3 wt % H_2O and 1 GPa, the diffusion coefficient for silica diffusion follows:

$$D = 2.583 * 10^{-8} \exp\left(-\frac{126.6}{RT}\right)$$

where D is the diffusivity coefficient in m^2/s, the activation energy is in kJ/mol, R is in J/mol*K, and T is in Kelvin. This equation allows for calculation of the diffusion coefficient at desired temperatures. While the silica and water contents in the experiments on which the equation is based are similar to those measured and estimated during development of the diffusion profiles that I studied, 1 GPa is much higher than the likely pressure at the time the mingling of melts

took place. However, it has been shown experimentally that pressure has a minor effect on the diffusion of silica when compared to the effects of composition, temperature, and water content of the melt (Baker, 1990, 1991).

2.3.3 Imaging Techniques and Methods

SEM-EDS maps were acquired using 15 kV for the electron beam accelerating voltage and a 256 μm field of view to give a resolution of 0.25 microns per pixel. The contacts were oriented perpendicular to the scanning direction in the SEM to maximize sharpness and avoid possible changes in beam intensity over time. For each EDS map, an average of 3750 - 9775 frames at 10 μm/pixel are collected. An increase in time results in a reduction in noise and higher signal; however, increasing time runs the risk of beam shift, due to instabilities in the electron beam when sitting in one location over multiple hours, or sample damage over the course of acquisition.

2.3.4 Melt Diffusion Modeling

The methods outlined in Gualda et al. (2012a and 2016) were adopted and modified in order to model melt diffusion. Unlike the treatment of Gualda et al. (2012a & 2016) while modeling trace elements within a pure phase of constant composition, additional cautionary considerations must be taken when modeling across melts of variable compositions. Timescales of diffusion can be calculated based on compositional data acquired through SEM-EDS elemental maps. Quantitative compositional line profiles are acquired from the 2D maps of selected areas that were chosen where a contact was visible in BSE between contrasting glass compositions. The sharpness between these contacts of chemically distinct zones can constrain

residence times. For each contact, eleven parallel profiles are extracted and relaxation times were calculated for each. The profiles were selected to be approximately orthogonal to the contact between the different zones; however, departures from orthogonal are small and the effect on calculated times can be effectively neglected (Gualda & Sutton, 2016).

Timescales for magma interaction were determined using a 1D model where diffusion proceeds between two semi-infinite regions of initially different composition until concentration is equal across the domains (**Figure 6**). At initial contact (time = 0) between two melts, the concentration profile at the contact is best approximated as a step function. As time progresses, the profile begins to relax and the rates of homogenization are controlled by diffusion between the two melts. While this treatment is not entirely an accurate representation of natural processes, the step function is a good approximation. The overestimated timescales resulting from the use of a step function will be negligible for the glass contacts considered.

We note that D will vary depending on the Si concentration in the melt such that the local diffusivities will vary along our initial profile. Preliminary numerical modeling exercises show that this effect will result in an asymmetry in the concentration profile; high Si content is associated with a low D value, which results in sharper corners at high concentration when compared to low concentration. For our purposes, this effect is negligible in determining time-scales, but further work might explore the impact more thoroughly. Based on these preliminary findings, we treat diffusion as being constant.

This diffusion problem has a well-known solution, where the degree of smoothing depends on the product of the diffusion coefficient (D) and time (t). The resulting concentration (C) profile as a function of distance (x) is described by a complementary error function (erfc) that spreads with time. A least-squares minimization procedure is used to find the

complementary error function that best matches each observed profile, by varying the concentration in the far field (c[-∞], c[+∞]), the center of the diffusion profile (x_c), and the diffusion length scale (√Dt) (Gualda et al., 2012a). Extracting the value of (2√Dt), a timescale can be calculated using a set diffusion coefficient (D) based on the Arrhenius equation of Baker (1991).

$$c(x) = \frac{1}{2}\mathrm{erfc}\left(\frac{x - x_c}{2\sqrt{Dt}}\right) * \left(c[-\infty] - c[+\infty]\right) + c[+\infty]$$

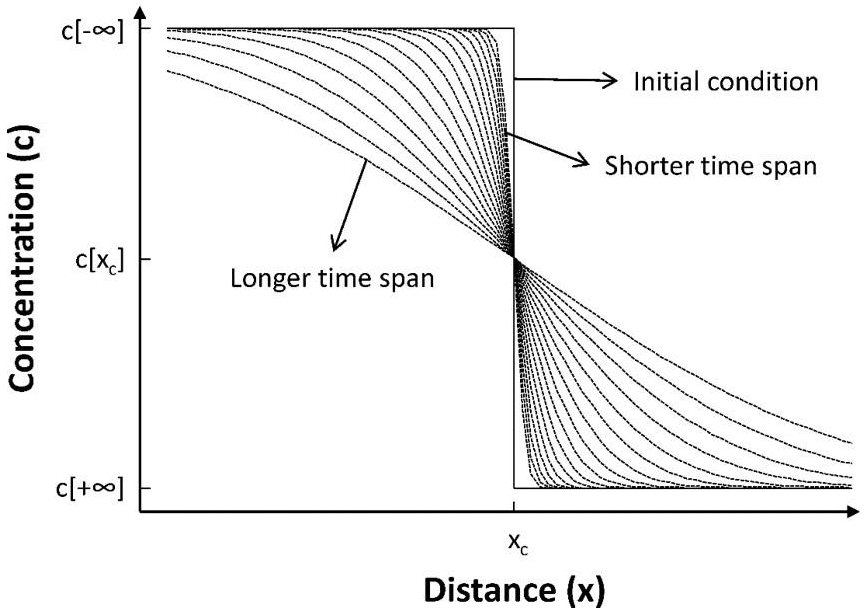

Figure 6. 1D diffusion model. We assume an initially infinitely sharp step function boundary. As time progresses, the profile becomes progressively less sharp. The resulting damped curve is described by a complementary error function (erfc). We use a least-squares procedure to find the best-fit erfc function and extract the value of (2√Dt). Using experimentally derived values of the diffusion coefficient D, we can calculate the residence times of a given contact.

2.4 Rhyolite-MELTS Modeling

Thermodynamic and geochemical modeling of the trachytic pumice and fiamme from the Tp5 zone of the Peach Spring Tuff was conducted using rhyolite-MELTS (Gualda et al., 2012b). I generated a series of rhyolite-MELTS modeling using bulk whole-rock composition of trachytic fiamme, expanding upon the modeling of Foley et al. (2014). Rhyolite-MELTS cannot be used to model the crystallization sequence of the cumulate, but was used to constrain conditions of interest (e.g. temperature, H_2O) by matching observed with model glass compositions with those that produced the observed liquid to solid ratio and phenocryst assemblage; this treatment is similar to Pamukcu et al. (2013) for estimating onditions for the intracaldera trachyte. Rhyolite-MELTS simulations were run over a range of total H_2O (1, 2, 3, 5, and 8 wt %) at pressures varying from 200 to 250 MPa, and from liquidus temperature until fully crystallized. Determining the input for model simulations was achieved by combining the pressure simulation results of Pamukcu et al. (2015) with the temperatures calculated from zircon and apatite saturation thermometry, estimates of crystal-liquid fraction, and glass analyses from each sample.

2.5 Trace Element Modeling

We generated a series of simple trace element models to test the plausibility of generating the compositions of the high-silica rhyolite via melt extraction of the trachyte cumulate. In our models, we assume perfect fractional crystallization from melt with the composition of mean PST. In detail, this is clearly an oversimplification, but the models provide a reasonable test of

the hypothesis that fractional crystallization of a PST-like parent magma can explain the composition of PST trachyte.

The input to the models (**Table 2**) included (1) the composition of PST as the parental (~bulk magma chamber) melt composition (three estimates that span the range within which the mean erupted PST is likely to lie; Frazier, 2013); (2) phenocryst modes in crystallizing assemblages (three modes were used, based on observed major phenocryst abundances and plausible ranges of abundances of observed accessories); (3) partition coefficients determined for PST (rhyolite glass vs. phenocryst rims; Padilla & Gualda, 2016); (4) remaining fraction of original melt estimated from rhyolite-MELTS modeling (Gualda et al., 2012b)(eighteen models, varying H_2O abundance and bulk magma composition); and (5) the fraction of trapped melt in cumulate based on mean trachyte and high-silica rhyolite compositions and mass balance.

Table 2

A. Rhyolite-MELTS starting compositions: Parental PST (~bulk magma chamber) starting compositions

	Rhyolite-MELTS Starting Parental PST Compositions					
	HSR~60%, Trachyte~30%, LSR~10%				HSR~75%, Trachyte~15%, LSR~10%	HSR~25%, Trachyte ~65%, LSR ~10%
SiO_2	72.25	72.25	72.25	72.25	73.29	69.82
TiO_2	0.32	0.32	0.32	0.32	0.28	0.42
Al_2O_3	14.31	14.31	14.31	14.31	13.82	15.45
Fe_2O_3	1.91	1.91	1.91	1.91	1.67	2.46
FeO						
MnO	0.07	0.07	0.07	0.07	0.07	0.07
MgO	0.37	0.37	0.37	0.37	0.30	0.53
CaO	1.01	1.01	1.01	1.01	0.91	1.25
Na_2O	3.61	3.61	3.61	3.61	3.55	3.76
K_2O	6.10	6.10	6.10	6.10	6.07	6.17
P_2O_5	0.05	0.05	0.05	0.05	0.04	0.08
H_2O	2	3	4	5	3	3

Table 2A. Rhyolite-MELTS input for model parental PST compositions. We attempted to constrain the mean composition of the PST, using the mean compositions of the high-silica rhyolite (Low-Zr, this study), low-silica rhyolite (High-Zr, this study), and the trachyte samples and our rough estimate of the relative abundance each type represents of the total volume of the PST. Because of the uncertainties, we calculated three different estimated means.

B. Phenocryst Modes

Phase	Mode #1	Mode #2	Mode #3
Sanidine	0.7	0.58	0.694
Plagioclase	0.154	0.25	0.17
Biotite	0.12	0.15	0.1
Apatite	0.003	0.002	0.002
Zircon	0.001	0.001	0.001
Sphene	0.001	0.002	0.002
Chevkinite	0.0006	0.001	0.001
Magnetite	0.02	0.014	0.03
(Quartz)	0	0	0
Total	1	1	1

Table 2B. Three different starting phenocryst modes were estimated to determine bulk partition coefficients.

C. Bulk Partition Coefficient and Mean PST HSR concentration

	Mean PST HSR (Frazier 2013)	Bulk D mode #1	Bulk D mode #2	Bulk D mode #3
U	5.46	0.06	0.06	0.07
Th	31.24	0.21	0.33	0.32
Nb	34.28	0.37	0.48	0.43
Rb	207.00	0.43	0.42	0.40
Y	32.00	0.94	1.20	1.21
Sc	3.74	2.75	3.21	2.91
Sr	30.00	6.28	6.91	6.42
Ba	51.00	9.65	8.81	9.62
La	64.04	2.61	3.99	3.99
Ce	118.07	2.61	3.97	3.97
Pr	12.82	2.04	2.97	2.97
Nd	39.86	2.57	3.68	3.68
Sm	7.20	2.36	3.36	3.37
Eu	0.55	3.83	4.69	4.68
Gd	5.83	1.90	2.67	2.66
Tb	0.94	1.82	2.37	2.38
Dy	5.40	1.55	1.93	1.94
Ho	1.07	1.11	1.42	1.43
Er	3.18	0.92	1.22	1.23
Tm	0.50	0.71	0.93	0.94
Yb	3.26	0.68	0.82	0.83
Lu	0.49	0.59	0.74	0.75

Table 2C. Eighteen trace element models for cumulate and extracted melt were generated by combining each starting parental compositions with the three estimated bulk partition coefficients.

CHAPTER 3

RESULTS

3.1 Textures and Phase Assemblage

Although the phenocryst assemblages differ only slightly, the proportions and compositions of phases in the high-silica rhyolite and trachyte contrast strongly. Furthermore, each sample is unique in proportions of phenocrysts and textures. Based on visual estimates using petrographic and scanning electron microscopy, phenocryst abundance is ~30-35% in the trachytic fiamme and pumice and ~2-15% in high-silica rhyolite.

3.1.1 Feldspar

Sanidine is the most abundant mineral in both the high-silica rhyolite and trachytic pumice and fiamme (roughly a 2:1 ratio to plagioclase). Phenocrysts range in size from ~0.2 to 5 mm, but tend to be larger in the trachyte. Sanidine in the trachyte exhibits a variety of textures reflecting disequilibrium; phenocrysts are variably rounded and often embayed (**Figure 11b.**), unlike the typical euhedral form in the high-silica rhyolite PST samples. Sparse rapakivi texture phenocrysts (plagioclase mantling rounded sanidine cores) are present in trachyte samples. Compositions are mostly ~Or_{48-60} for both cores and rims of both trachytes and HSRs. Sanidine in HSR is on average slightly more sodic than that in trachyte, but overlap is almost complete (**Figure 7**). Phenocrysts do not exhibit strong zoning in Na and K in either the high-silica

rhyolite or the trachyte. However, Ba concentrations, which are commonly measurable by SEM in trachytes (up to 3.5 wt % BaO; **Figure 11c.**), reveal distinct zoning: Ba-enrichment is more commonly preserved in rims, though some phenocryst show fluctuating BaO zoning from core to rim. Barium is not detectable in HSRs.

Plagioclase phenocrysts range from ~0.1 to 2 mm in maximum dimension. Phenocrysts in trachytic samples range from sub-euhedral to anhedral; some show sieve textures and embayment (**Figures 11a. 11f**), but they generally show much less pronounced dissolution features than the sanidine. Within the high-silica rhyolite, phenocrysts are euhedral. Plagioclase within trachytic samples are distinctly more calcic (mostly ~An33-47) than plagioclase in high-silica rhyolite (mostly ~An23-28; **Figure 8**). Phenocryst do not exhibit strong zoning in Ca and K in either the high-silica rhyolite or trachyte.

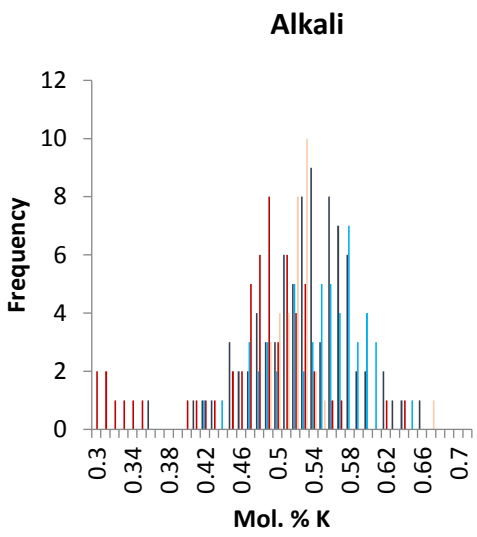

Figure 7. Histogram mol % K of alkali feldspars in trachyte versus high-silica rhyolite. Sanidine in HSR is on average more sodic than in trachyte.

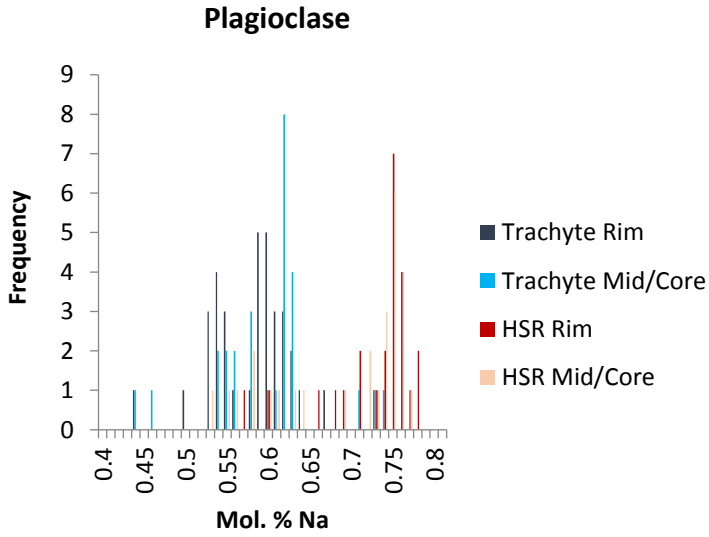

Figure 8. Histogram mol % Na of plagioclase compositions in trachyte versus high-silica rhyolite. Slight bimodal populations appear between trachyte and HSR plagioclase.

3.1.2 Biotite

Biotite is the dominant ferromagnesian phase in trachyte samples, but subequal in proportions to amphibole in HSR. Sizes range from 0.1 to 1.5 mm. Phenocrysts are sub-euhedral to anhedral with common embayment in trachyte (**Figure 11e**) and generally euhedral in HSR. Biotite TiO_2 concentrations distinguish two populations: (a) high TiO_2, ranging from 5 wt % to 8.5 wt %, and (b) low TiO_2, ~3-4 wt % (**Figure 9**). The remarkably TiO_2-rich phenocrysts are predominantly found within trachyte, but low TiO_2 biotite is rarely present. Similarly, the low TiO_2 biotite are typical for the high-silica rhyolite samples, but high TiO_2 biotite are also found within stratigraphically higher HSR zones (Tp3 and Tp4). Compositions of biotite display a range in Mg# for both populations, but predominantly cluster within 0.65 – 0.75 for the trachytic samples. Like sanidine, trachytic biotite phenocrysts are often zoned in BaO, reaching 3.7 wt% (**Figure 11d.**). Inclusions of accessory phases (e.g. apatite, zircon, chevkinite, Fe-Ti oxides) are commonly found in biotite.

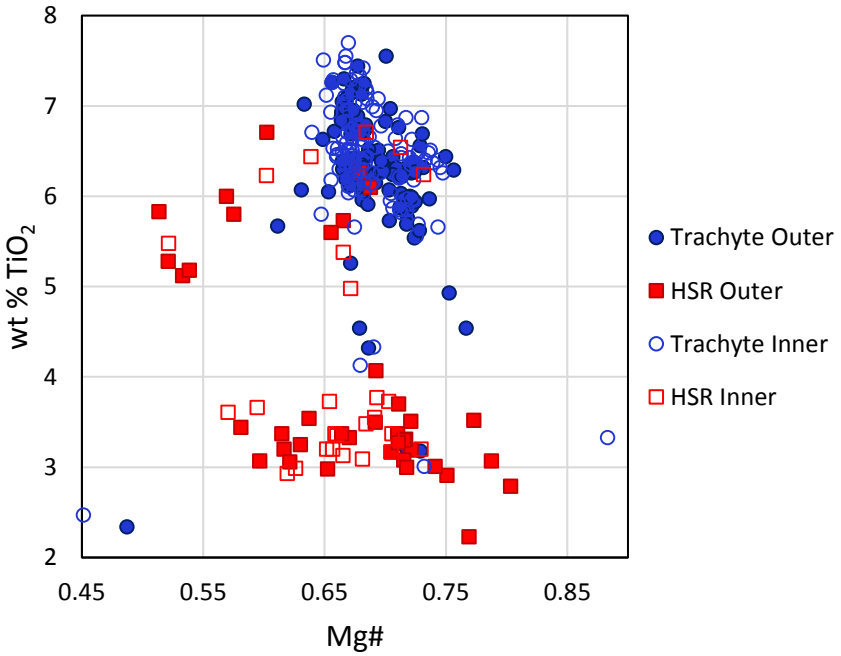

Figure 9. Biotite compositions of TiO_2 wt % vs Mg# in trachyte versus high-silica rhyolite. Outer rims of biotite are plotted with closed symbols and mid to inner core compositions are plotted with open symbols. Trachyte biotite are primarily >5 wt % TiO_2 compared to the typical low <4 wt % TiO_2.

3.1.3 Other Major Phases

Clinopyroxene is the other major phase found in trachytic samples, but it is absent in the high-silica rhyolite. Most phenocrysts are small (~0.5-1 mm) and subhedral. All are augite in composition, averaging Ca_{83} Mg_{80} Fe_{26}, with minor Na and Al substitutions (Na_{05} and Al_{10}). Phenocrysts are commonly found in clusters (glomerocrysts) with other major and accessory phases (**Figure 11f**).

Amphibole is rare in the trachyte samples, but two thin sections have a single phenocryst; in both cases, the amphibole is enclosed by high-silica rhyolite glass. Conversely, amphibole is a common major phase in the high-silica rhyolite samples. All amphiboles are compositionally hornblende and are relatively unzoned; sizes range from ~0.5 mm to 1 mm.

Rare quartz is present in the high-silica rhyolite, but absent from the trachyte. Phenocryst are typically euhedral and range in size ~100 μm to 1 mm.

3.1.4 Accessories

Accessory phases in the trachyte constitute ~≤ 3% modally of the phenocryst content, but are more abundant compared to the high-silica rhyolite samples (~1%). Accessory phases include Fe-Ti oxides (ilmenite, magnetite), sphene, apatite, zircon, and chevkinite. Sphene is rare in trachyte samples, but is an abundant accessory in the high-silica rhyolite and can reach up to 1-mm. Fe-Ti oxides commonly show variable reaction and disequilibrium textures, including rounded edges. Accessories commonly are clustered together with major phases (Pamukcu et al., 2013) (**Figure 11f.)**.

3.1.5 Glass

Glasses in the trachytic pumice and fiamme exhibit variable mingling textures in thin section. Similar to the coloration seen in hand-sample, unwelded trachytic pumice are orange in plane polarized light whereas high-silica rhyolite glasses are clear to grey. The degree of vesiculation is variable among samples of both trachyte and high-silica rhyolite pumice – mostly depending upon the degree of compression the sample experienced during the cooling history of the ignimbrite.

Two samples (WSB Fo 1 and WSB Fo 31) contain multiple glass populations visible in thin section. Glass textures preserved in these samples show obvious glass (melt) interactions, but the scale and degree of glass mingling varies. The contrast of a light tan to brown colored glass with the predominant pale glass matrix of the fiamme is apparent in plane polarized light (**Figure 10a., 10b., 10d**). The glasses show prominent intermingling and swirling textures. The light-tan glass is also preserved as thin rinds that rimming individual phenocryst as well as entire clusters of phenocrysts. The two glasses are readily distinguished in SEM-BSE images that reveal strong compositional contrast (**Figure 10c**). Contacts between the two glasses are very sharp (**see 3.3 Timescales of Diffusion**), unlike the blurred contact between the glass matrix and the third glass population present in WSB Fo 31. This glass, which is comparatively higher in SiO_2, is only distinguishable by compositional analyses. Its abundance is considerably smaller than the other two glasses and its distribution throughout the fiamme is not systematic.

Elemental compositions of all glasses are discussed in following sections.

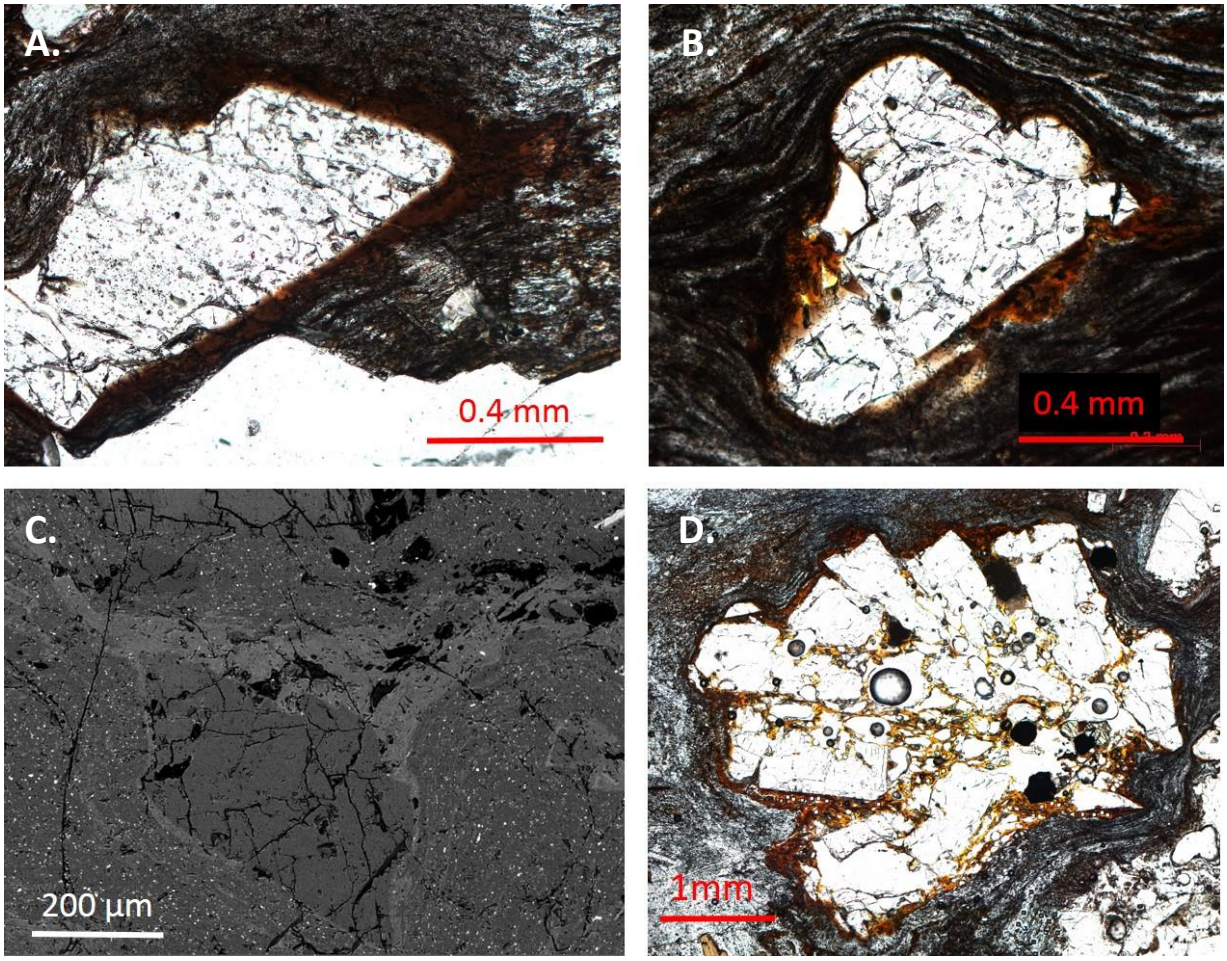

Figure 10. (A and B). Plane polarized light image showing thin glass rind encompassing feldspars in sample WSB Fo 1. (C) SEM-EDS image showing glass rind around feldspar in WSB Fo 1 and apparent contrast in composition. (D) Cluster (glomerocryst) of major and accessory phases enclosed within brown glass found in fiamme of WSB Fo 31.

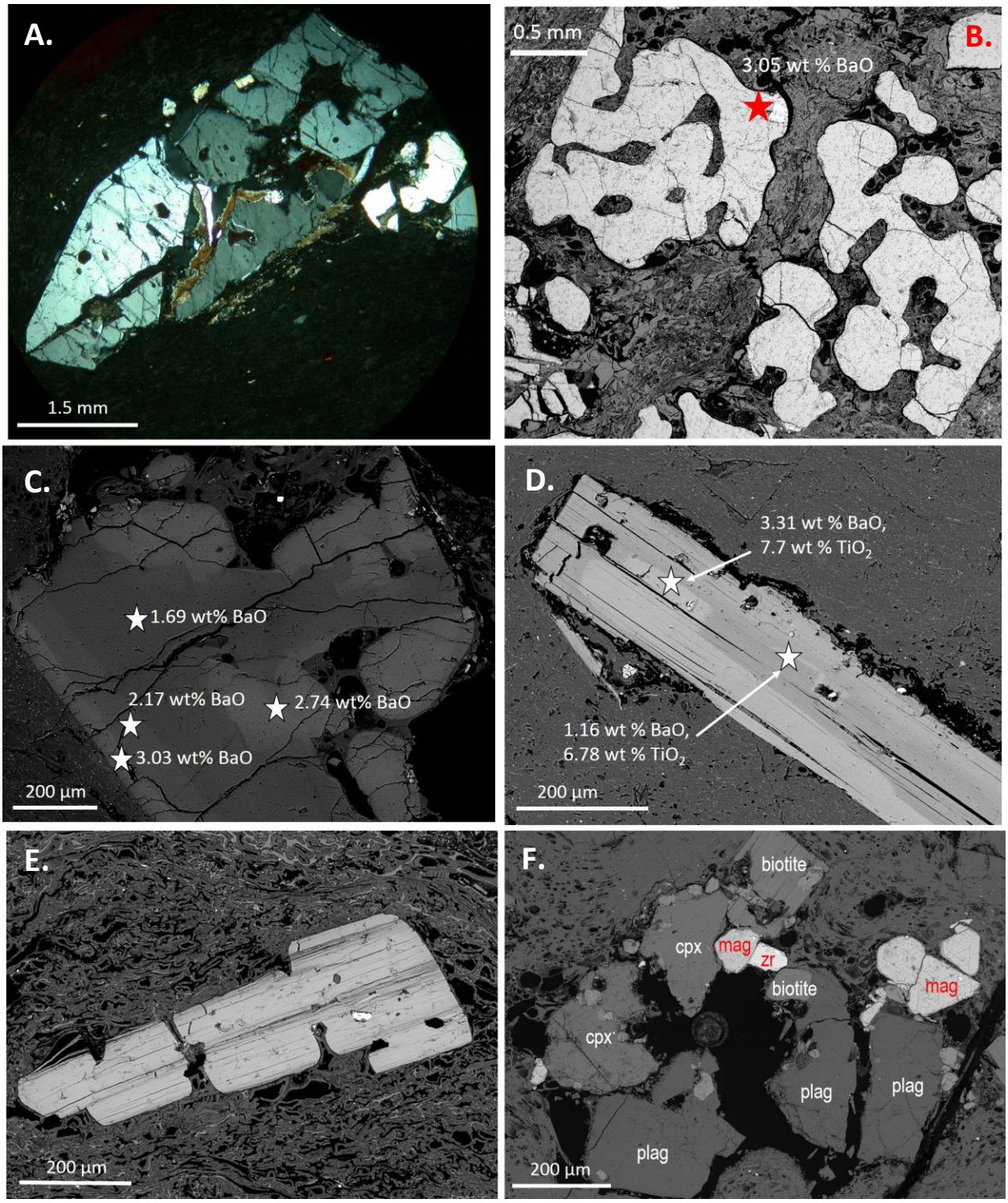

Figure 11. (A) WSB Fo 3 large (>4 mm) plagioclase in plane polarized light with rounding and embayments; (B) SWA Fo 1A extreme sanidine embayment and Ba-enriched zones; (C) WSB Fo 31 sanidine with similar embayments, rounding and Ba-enriched zones (D) high TiO_2 biotite in WSB Fo 31 also showing Ba-enrichment; (E) SWA Fo 1A biotite embayments; (F) glomerocryst of major phases and accessories in WSB Fo 3.

3.2 Major and Trace Elemental Geochemistry

3.2.1. Whole rock (pumice and fiamme) chemistry

Silica concentrations of pumice and fiamme range from 64 wt % to 76 wt % (major element oxides normalized to 100% anhydrous). In this thesis, I adopt a whole rock compositional classification similar to, but modified from, Pamukcu et al. (2013) and Frazier (2013), Although the considerable range in major element oxide compositions supports useful, simple groupings, compositions are more meaningfully distinguished using trace elements as well as major elements. Most notably, concentrations of Zr and rare earth elements (REE) are clearly divided into two groups, one with moderate concentrations and the other with high to extreme abundances (s**ee Fig. 12**). The lower Zr, REE group are all rhyolites (all >71 wt% SiO_2, almost all >73.5%), whereas the higher Zr, REE group is made up of low-SiO_2 rhyolites and trachytes (<73.5 wt% SiO_2). Zirconium distinguishes the two groups especially well: all in the low-trace-elements group have <300 ppm Zr, and all in the high group have >400 ppm. I will maintain the tripartite nomenclature of Pamukcu et al. (2013) and Frazier (2013): trachyte, low-Zr, and high-Zr – but modified slightly to reflect the clear distinction in trace element concentrations. In this scheme, low-Zr and high-Zr overlap in SiO_2: the former have >71 wt% SiO_2 and <300 ppm Zr, and the latter 70-73.5 wt% SiO_2 and >400 ppm Zr. Trachytes have <70 wt% SiO_2 and >400 ppm Zr (**Figure 12**). While the High-Zr rhyolite samples represent an important process of the magma evolution, they are relatively minor and will be considered broadly within high-silica rhyolite (HSR) nomenclature during discussion throughout this thesis. A table of major and trace element elemental chemistry for each sample and the corresponding classification can be found in **Appendix B**.

Major elements vary regularly with SiO_2. As SiO_2 increases, Al_2O_3, CaO, Fe_2O_3(T), TiO_2, and P_2O_5 decrease monotonically (**Figure 12**). Alkali concentrations do not in general vary greatly and do not correlate well with SiO_2. All samples have very high K_2O concentrations, almost all having >5 wt%. Na_2O is generally between 3 and 4 wt%, but some Low-Zr have concentrations that are well below 3 wt%; we interpret these low concentrations to reflect alteration of the samples (McCracken 2012, Pamukcu et al 2015). As noted above, trace elements concentrations are extremely, but systematically, variable (**Figure 12**). Low-Zr samples have very low Ba and Sr (respectively ~15-200 ppm, 10-60 ppm [one outlier at 135 ppm – altered?]), moderately high Rb (120-260 ppm), and moderate Zr (170 – 270 ppm). Rare earth elements, especially light REE (LREE), are also moderate in concentration (e.g. Ce 90-150 ppm). High-Zr samples are similar to the Low-Zr samples in their low concentrations of Sr (15 – 40 ppm) and Ba (30 - 210 ppm) and moderately high Rb (140 – 200 ppm), but they have much higher Zr (440-510 ppm) and REE (e.g. Ce 190-230 ppm). Trachyte samples show a broader range in concentrations than High-Zr and Low-Zr. Rubidium concentrations are generally lower (80 – 160 ppm) with the exception of an anomalously high concentration in one sample (320 ppm – GJ Fo1). Ba and Sr concentrations range from slightly to much higher (220 – 2850 and 90-480 ppm, respectively). Zirconium and REE concentrations are also much higher (420-760 ppm, 270-340 ppm [Ce], respectively). All but two trachytic samples have Zr/Hf ratios >40 and approach 50, substantially higher than the chondritic and typical crustal values of 35-40. In contrast, all Low-Zr samples have ratios of 25-35. The Zr/Hf ratios of High-Zr are high and nearly uniform (40-42).

Trachytic samples are enriched in LREE relative to Low-Zr and High-Zr and have the smallest negative Eu anomalies (Eu/Eu* = 0.53-0.99) (**Figure 13**). All three compositional types

have similar heavy REE (HREE) abundances. Low-Zr samples have the lowest HREE and the largest negative Eu anomalies (0.21-0.39). High-Zr samples are intermediate in LREE and most show distinct enrichment in middle REE (MREE); their Eu anomalies are similar to those in Low-Zr (0.24-0.29).

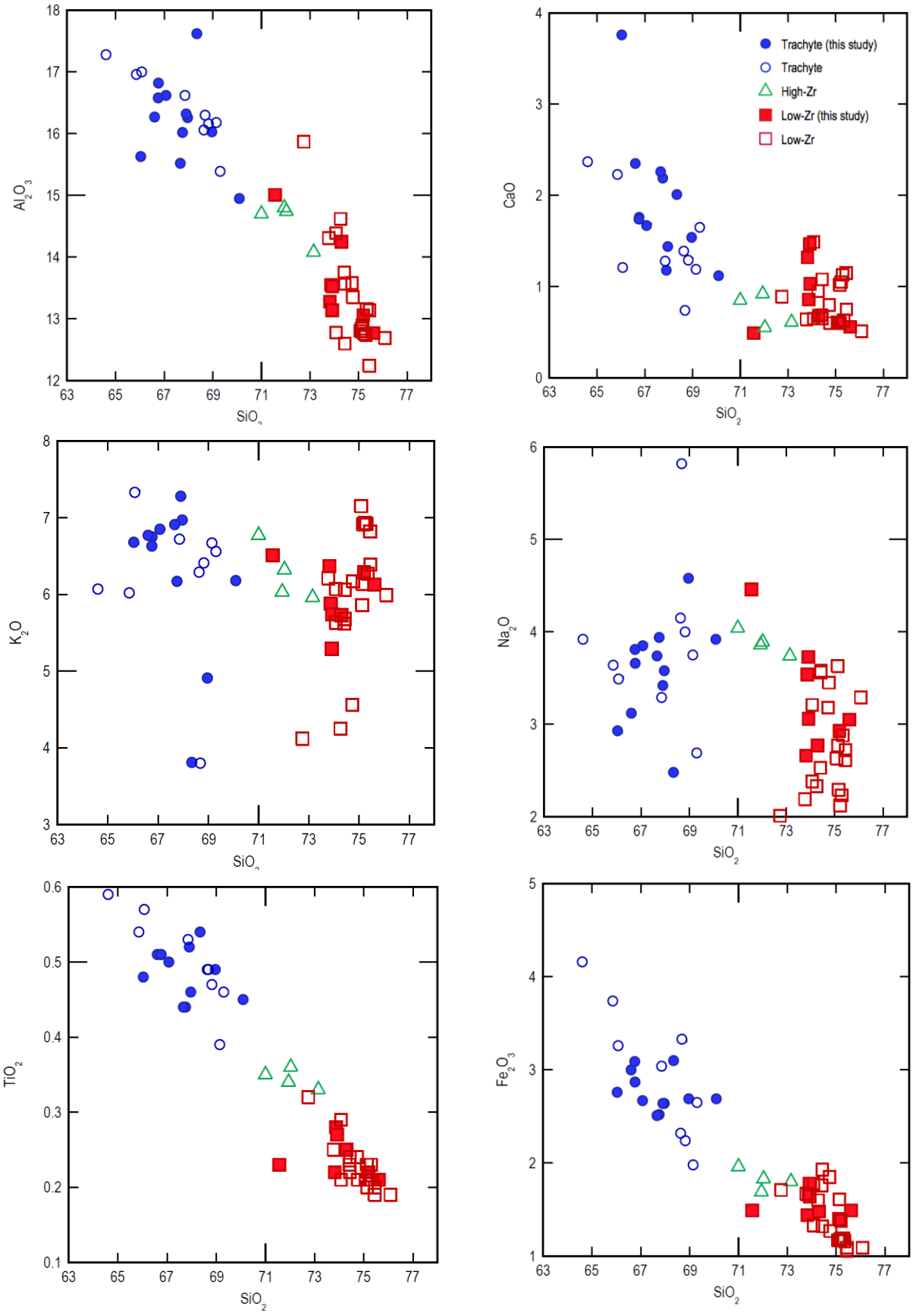
Trachyte (this study)
Trachyte
High-Zr
Low-Zr (this study)
Low-Zr
Al2O3
CaO
K2O
Na2O
TiO2
Fe2O3
SiO2

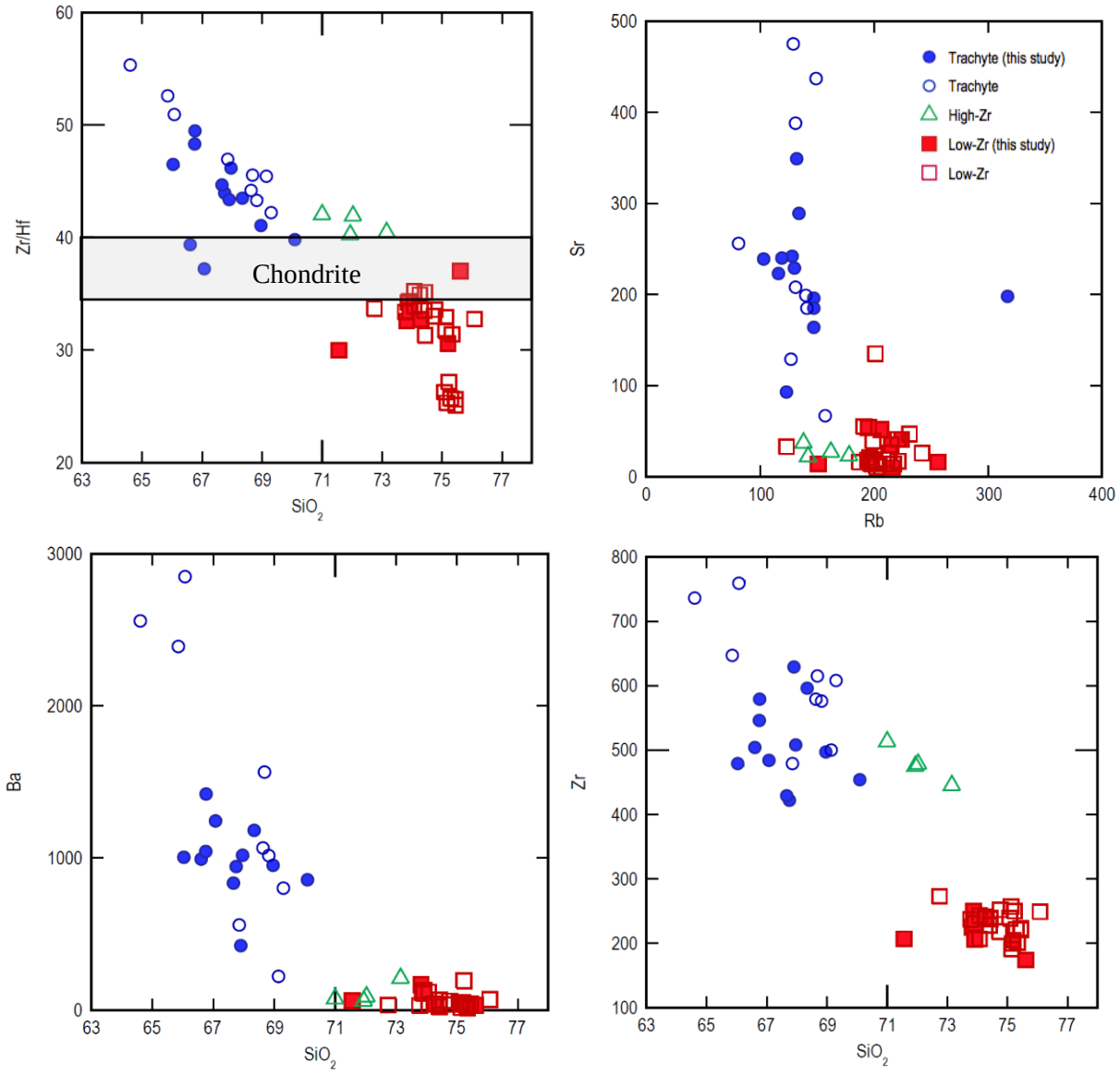
Zr/Hf
SiO2
Chondrite
Sr
Rb
Trachyte (this study)
Trachyte
High-Zr
Low-Zr (this study)
Low-Zr
Ba
SiO2
Zr
SiO2

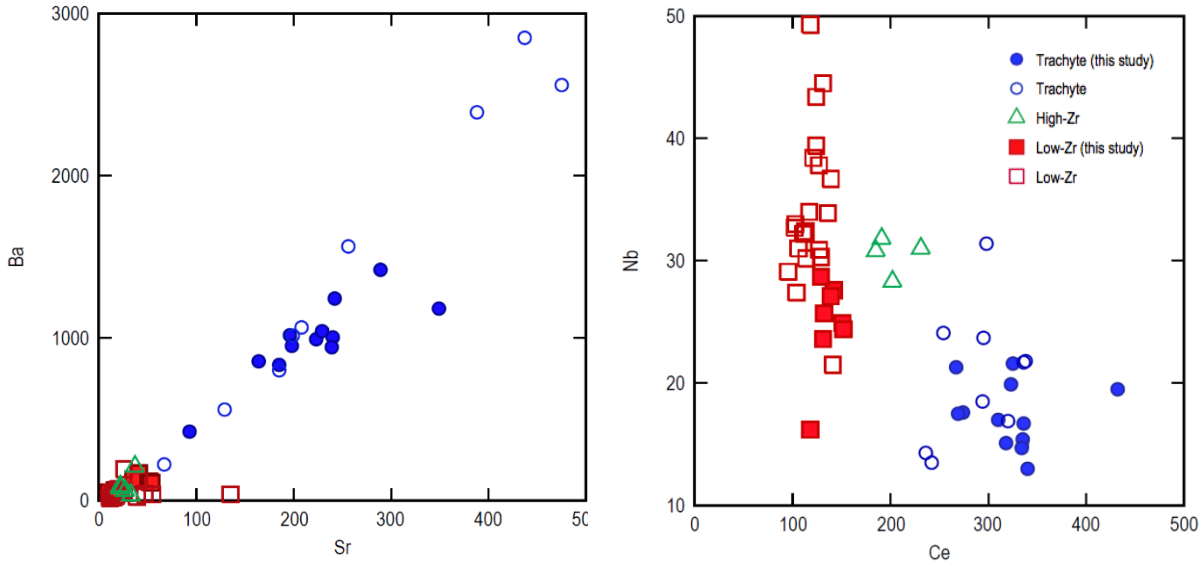

Figure 12. Whole-rock major and trace element variations in pumice and fiamme. Closed symbols correspond to samples included in this study; open symbols include those of Frazier (2013).

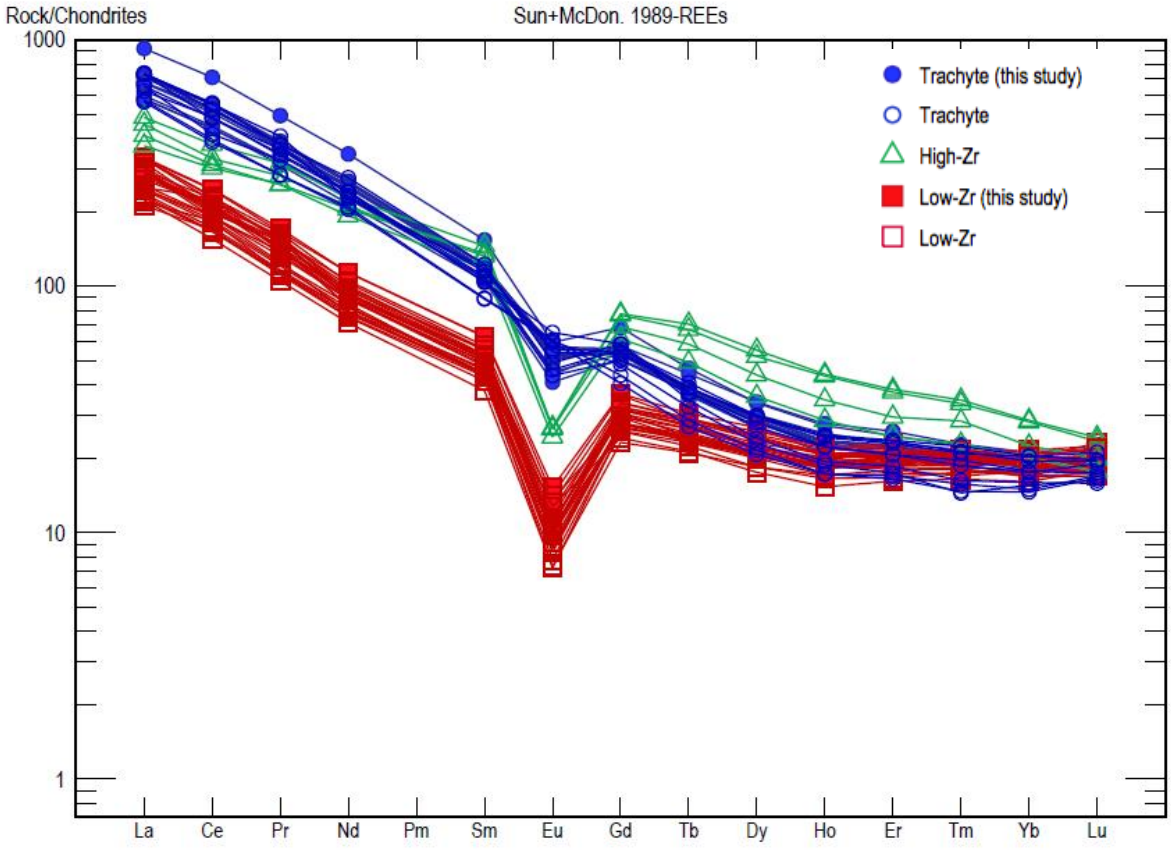

Figure 13. Average REE concentrations for each bulk whole-rock sample. The trachyte sample show the most enrichment in Light REE, compared to the High-Zr and Low-Zr rhyolites. The trachyte and Low-Zr rhyolite have similar concentrations of Middle REE, but the High-Zr rhyolites show distinct enrichment in Middle REE.

3.2.2 Glasses

Major element concentrations of glasses are grouped into Low-Zr rhyolite and trachyte based on the whole-rock composition as described above (no samples of High-Zr rhyolite were analyzed as part of this study). Only those samples that have both glass and whole-rock analyses are plotted in the figures 13-15 (four Low-Zr rhyolites, nine trachyte). One sample that lacks a whole-rock analysis is included because of its significance throughout the rest of this study (WSB Fo 31); based on its phenocrysts and glass composition, it is plotted confidently as trachyte.

Silica in glasses ranges from 64 wt % to 78 wt % (**Figure 14**). Glass in samples that are trachytic in whole-rock composition range in SiO_2 from 66 wt % to 75 wt%; most fall into two clusters, one at ~67.5±1 wt% and the other, more abundant, at ~72±1 wt%. Major elements including Al_2O_3, CaO, TiO_2, MgO, and FeO decrease monotonically with increasing SiO_2 content. The trends for Na_2O and K_2O are similar to those seen in whole-rock plots where there is no strong contrast in concentrations among trachytic through Low-Zr glasses. A/CNK ratios are variable but cluster between 0.95 – 1.10. Outlier values above 1.1 and below 0.9 are not likely magmatic but probably result from secondary alteration (Pamukcu et al., 2015). One sample (GJ Fo 1) plots as an individual cluster with uniquely high Na_2O and low K_2O. All Low-Zr samples are tightly clustered at 76.7±0.7 wt%, and they also fall within a narrow range for most other major elements. Na_2O and K_2O both exhibit considerable variability (2.5-4 and 5-7 wt% respectively) and they display a tight negative correlation. We interpret this range to reflect alkali exchange alteration and infer that the higher Na_2O and lower K_2O values reflect the magmatic compositions (Pamukcu et al., 2015).

The Low-Zr samples cluster tightly in trace element concentrations, but there is a large range in compositions in trachytic samples (**Figure 15** Low-Zr concentrations range 2 – 15 ppm for Ba, 1 – 9 ppm for Sr, 200 – 270 ppm for Rb, and 100 – 140 ppm for Zr. For the trachytic samples, concentrations range from 65 – 4100 ppm for Ba, 20 – 330 ppm for Sr, 130 – 180 for Rb, and 320 – 830 ppm Zr. The mean glass REE patterns are nearly identical for all Low-Zr samples (**Figure 16**). As with whole-rock analyses, Low-Zr are lowest in LREE and MREE and have the largest negative Eu anomalies (Eu/Eu* = 0.22-0.25). The LREE and MREE in the trachyte glasses are much higher, and HREE only slightly higher. Eu anomalies are much smaller (0.40-0.97) in trachyte. A table of average trace element concentrations for all samples can be found in **Appendix E**.

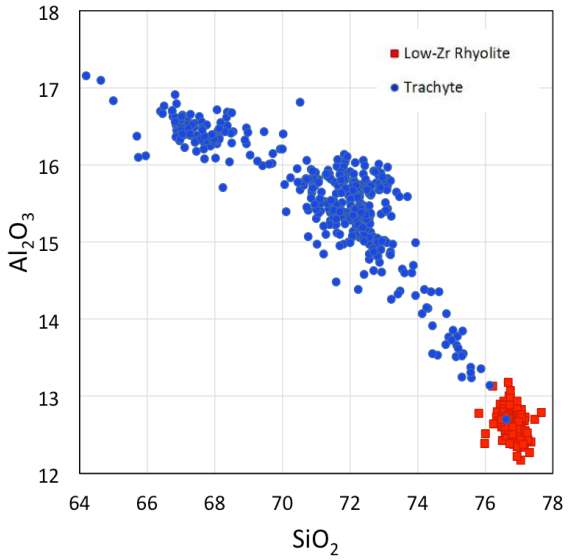
Low-Zr Rhyolite
Trachyte
Al2O3
SiO2

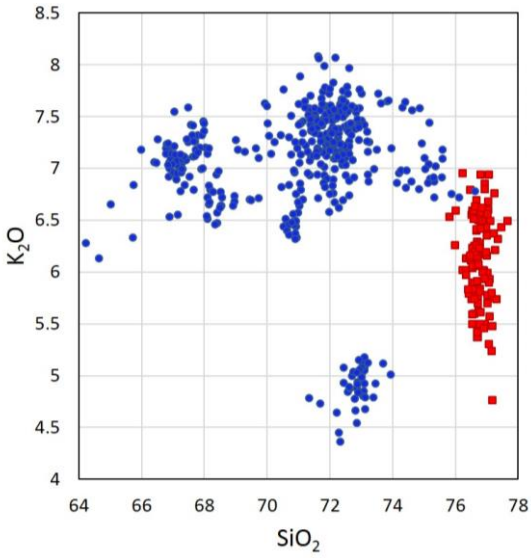
K2O
SiO2

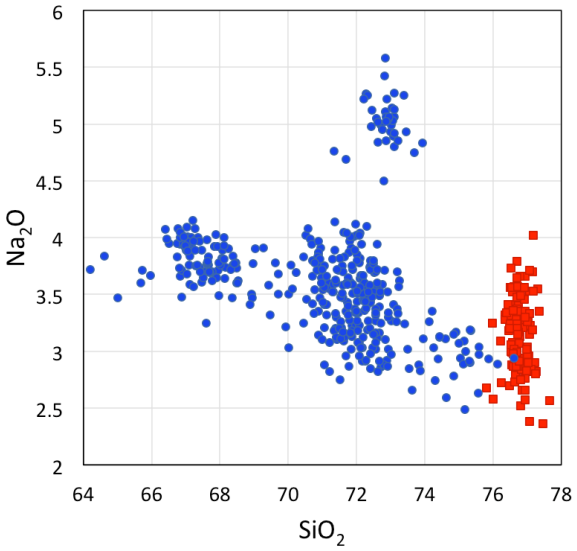
Na2O
SiO2

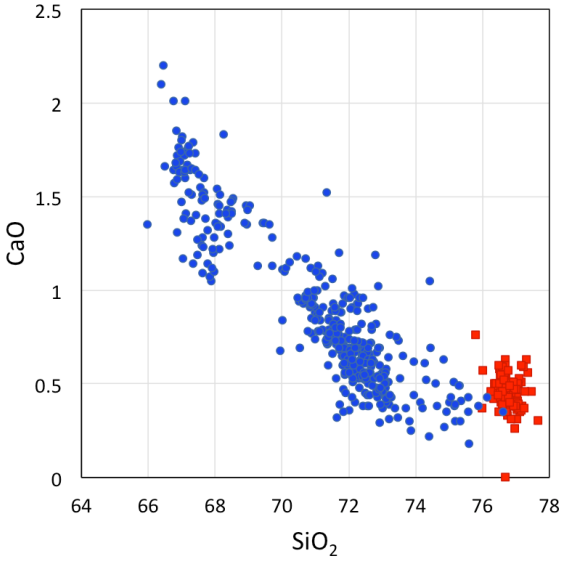
CaO
SiO2

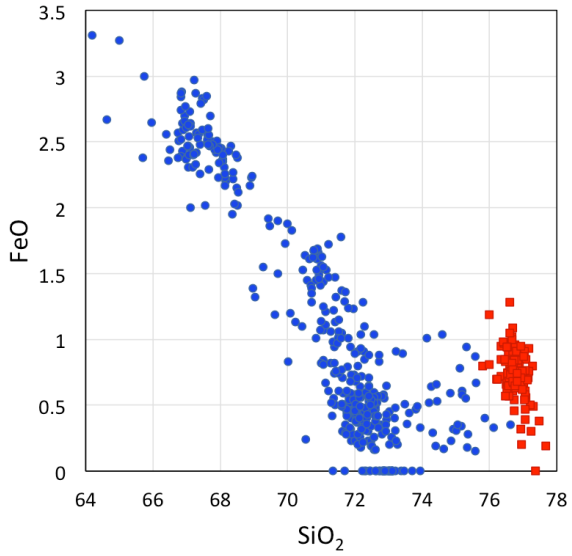
FeO
SiO2

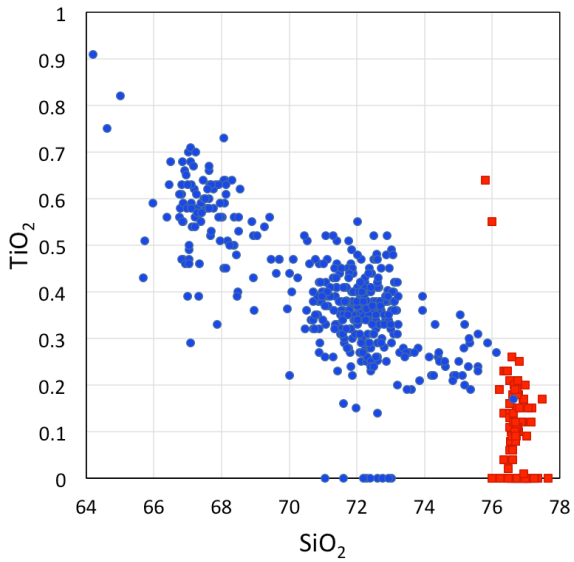
TiO2
SiO2

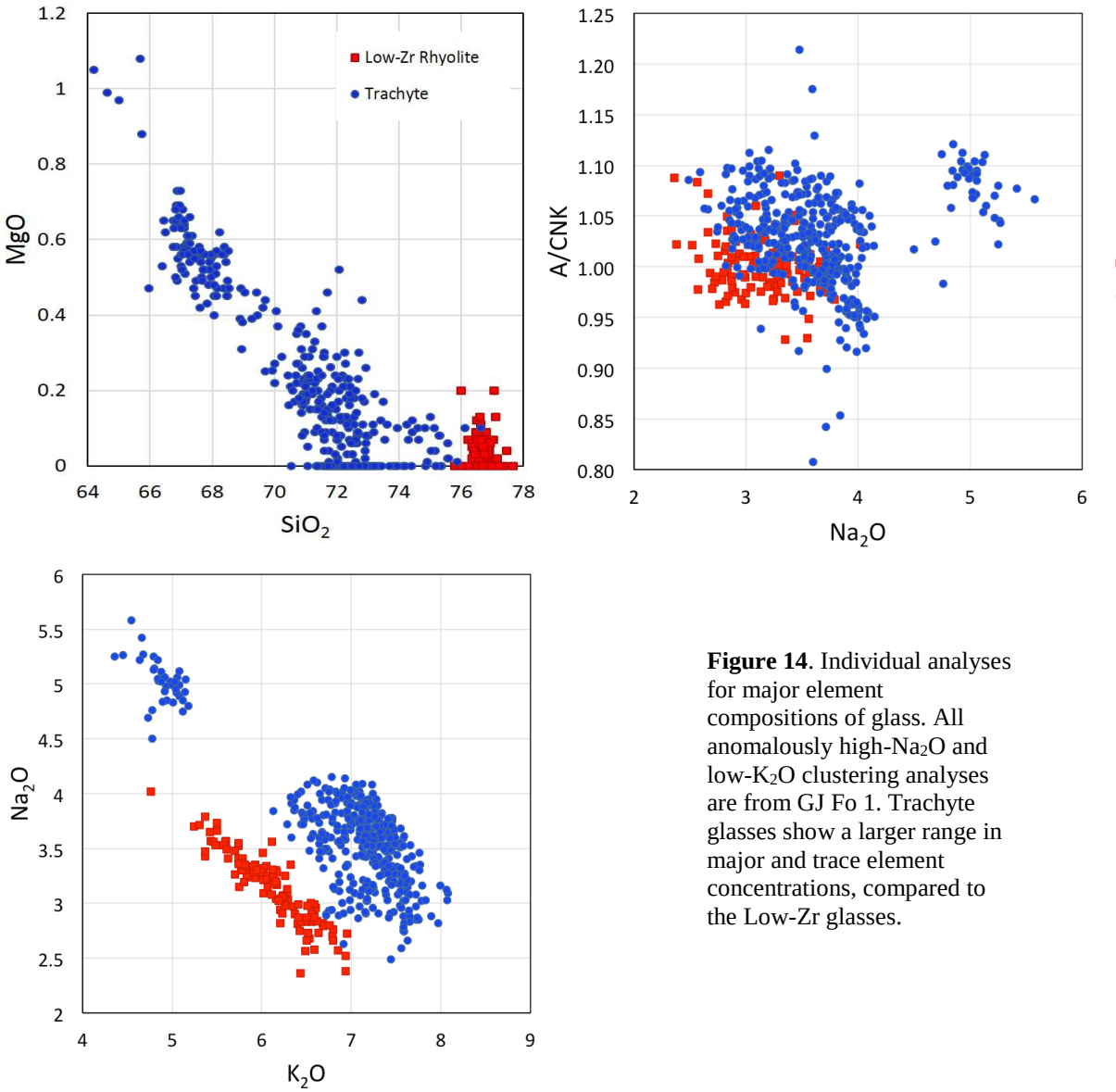

Figure 14. Individual analyses for major element compositions of glass. All anomalously high-Na_2O and low-K_2O clustering analyses are from GJ Fo 1. Trachyte glasses show a larger range in major and trace element concentrations, compared to the Low-Zr glasses.

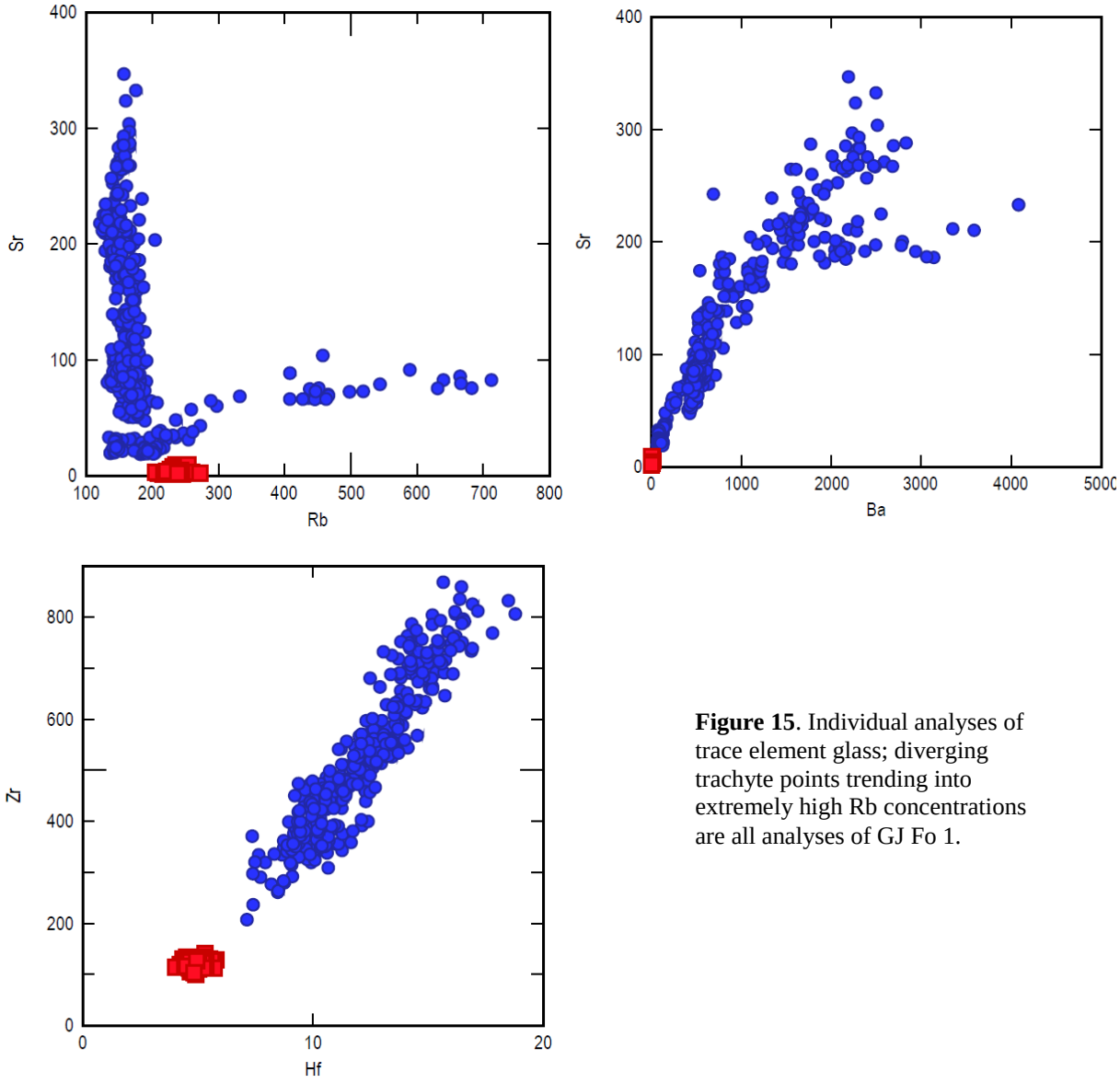

Figure 15. Individual analyses of trace element glass; diverging trachyte points trending into extremely high Rb concentrations are all analyses of GJ Fo 1.

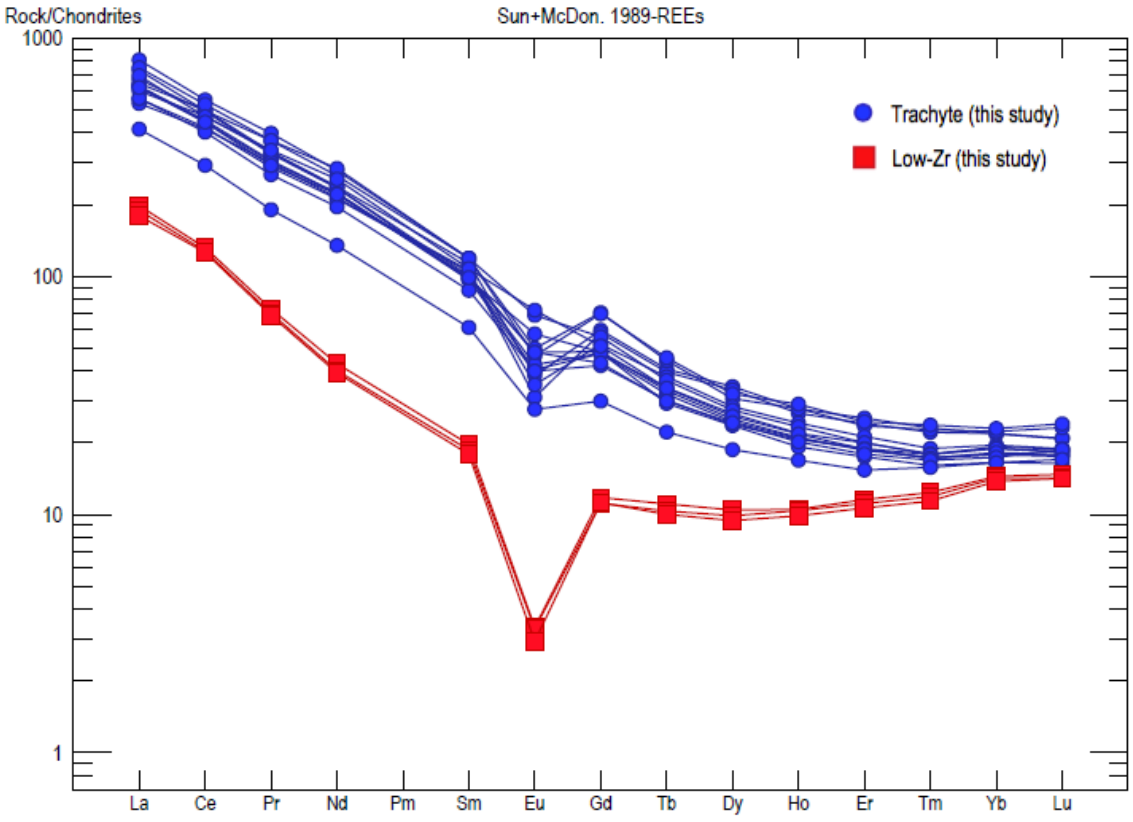

Figure 16. Average glass REE concentrations for each sample. Trachyte glasses show variable enrichment compared to the distinctly uniform Low-Zr rhyolites.

3.2.3 Samples with Multiple Glass Populations

Multiple glass populations that are readily distinguishable in thin section and by SEM in BSE images are found in two samples: WSB Fo 1 and WSB Fo 31. These populations are grouped as A (<70 % SiO_2 in WSB Fo 1; <69 % SiO_2 in WSB Fo 31), B (70-74 wt % SiO_2 in WSB Fo 1; 69-73 % in WSB Fo 31), and C (73-75 wt % SiO_2 [WSB Fo 31 only]) (**Figure 17**). In both fiamme, the matrix is predominantly group B glasses, which are similar to those in other trachytic samples. In group C glasses SiO_2 contents are equal to the less silicic Low-Zr whole rocks, but they are substantially lower than Low-Zr glasses. Likewise, other major element contents span a range between those of trachyte and Low-Zr glasses.

Group A trace element concentrations range 1070- 4100 ppm for Ba, 180- 350 ppm Sr, 133- 180 ppm Rb, and 600- 870 ppm Zr (**Figure 18**). Group B concentrations range 490- 1440 ppm Ba, 80- 240 ppm Sr, 140- 180 ppm Rb, and 280- 730 ppm Zr. Group C concentrations range 410- 1880 ppm Ba, 870- 220 ppm Sr, 155- 190 ppm Rb, and 210- 550 ppm Zr. Group A glasses are the most enriched in LREE and MREE and show the smallest Eu anomaly (Eu/Eu* 0.84-0.98) (**Figure 19**). REE in group B are similar to group A, but show a larger Eu anomaly (0.72-0.73) than group A. REE in group C are more enriched than Low-Zr glass, but poorer in LREE and MREE than group A and B glasses. The Eu anomaly in group C is larger (0.65) than both A and B, but it is smaller than that in typical Low-Zr.

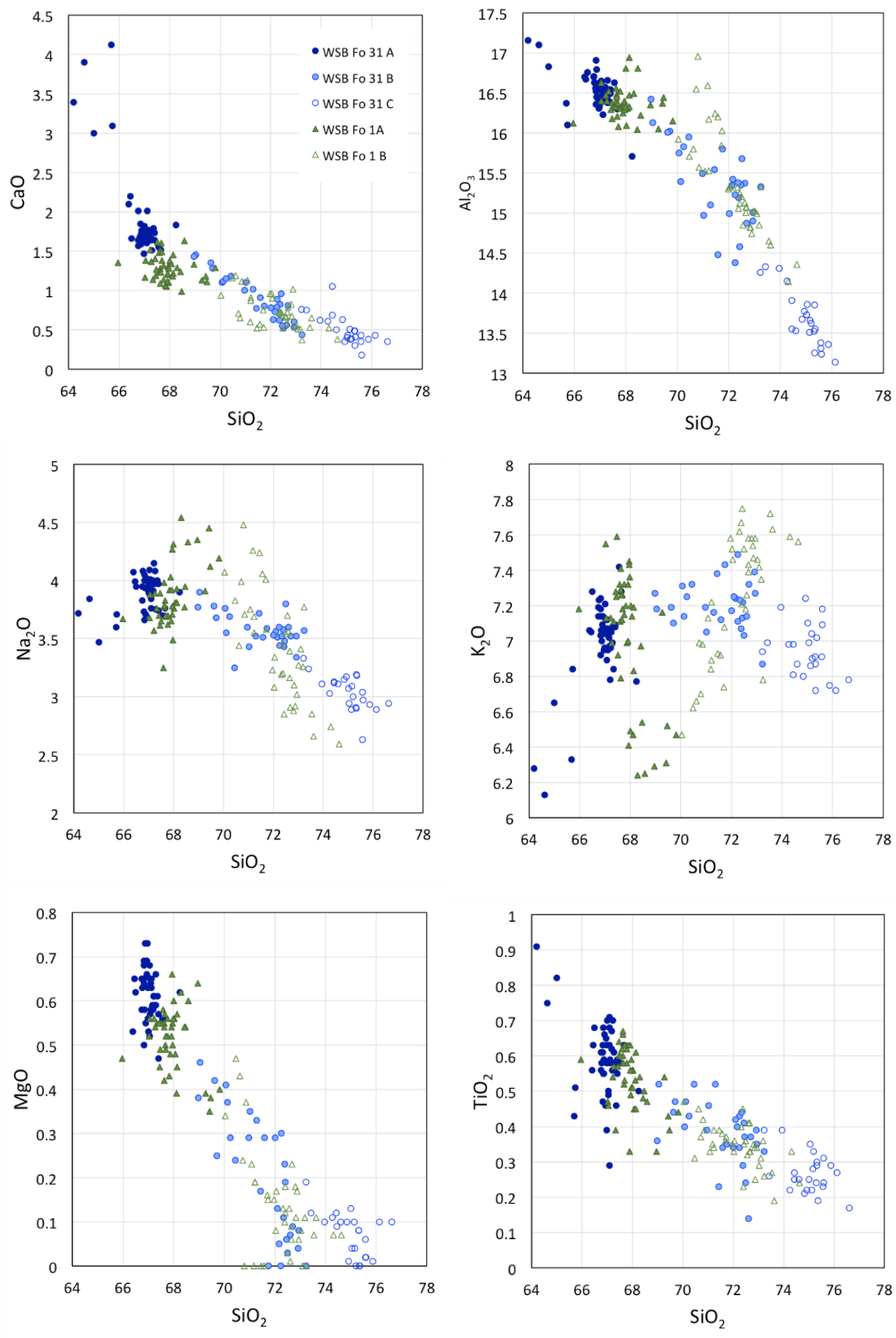
WSB Fo 31 A
WSB Fo 31 B
WSB Fo 31 C
WSB Fo 1A
WSB Fo 1 B
CaO
SiO2
Al2O3
Na2O
K2O
MgO
TiO2

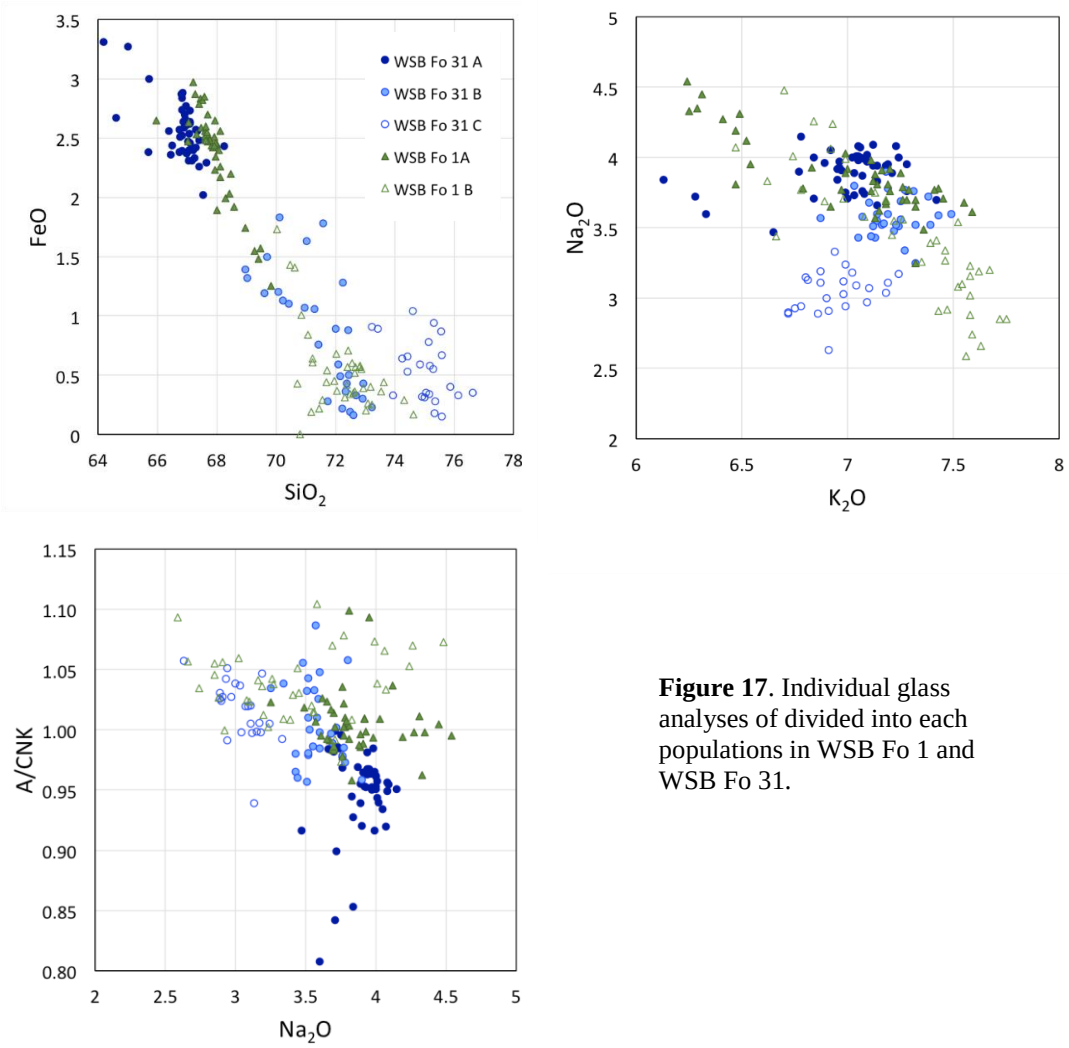

Figure 17. Individual glass analyses of divided into each populations in WSB Fo 1 and WSB Fo 31.

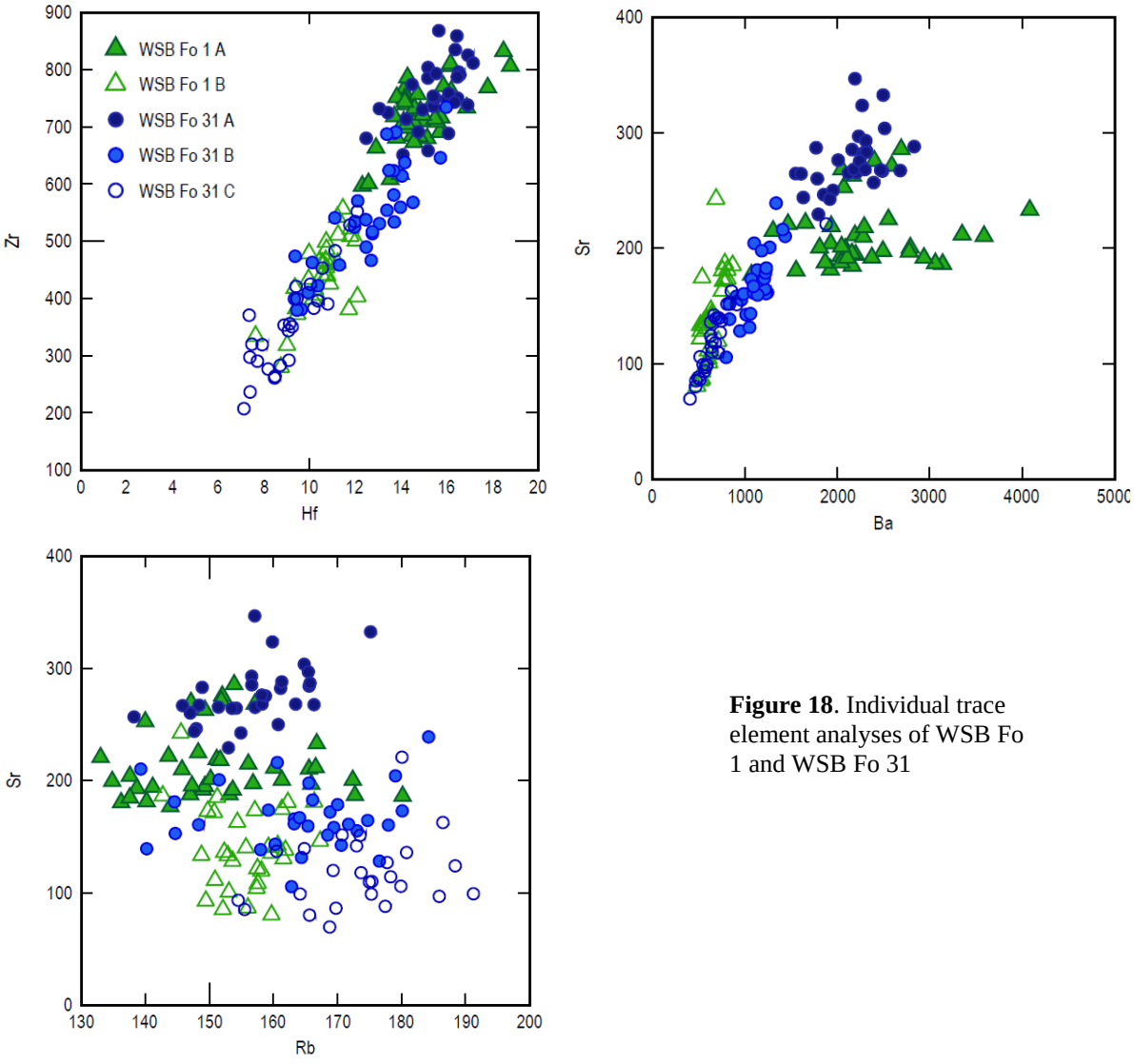

Figure 18. Individual trace element analyses of WSB Fo 1 and WSB Fo 31

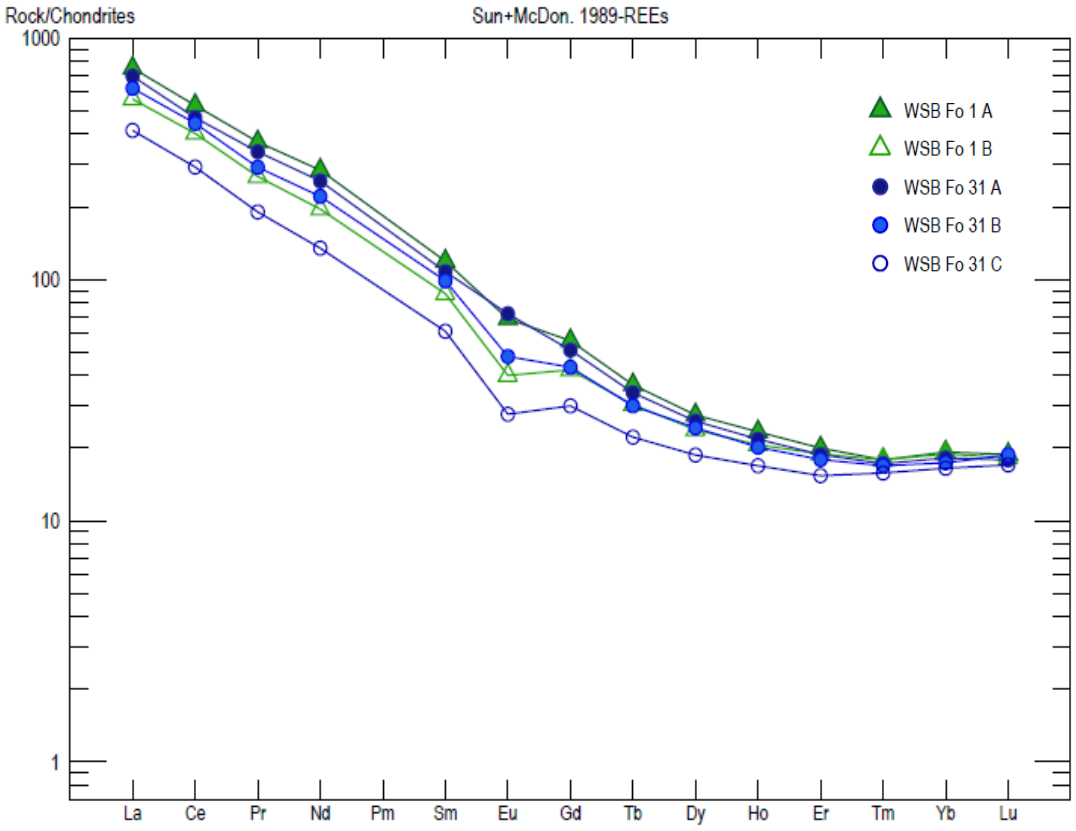

Figure 19. Average glass REE concentrations of WSB Fo 1 and WSB Fo 31. Group A glasses have the highest concentrations of REE and exhibit the smallest Eu anomaly. The REE patterns of Group B are most similar to those of trachytic pumice and fiamme. Group C glasses are more enriched in REE, compared to typical Low-Zr rhyolite.

3.3 Timescales of Diffusion

Three EDS-maps were selected between glasses of 66 and 72 wt % SiO_2 (the A to B contact) within one sample (WSB Fo 31). They were imaged and subsequent profiles fit to calculate timescales of diffusion. The visibility of the contrasts between glasses of 66 and 72 wt % SiO_2 in SEM-BSE images is likely a result of higher FeO concentration in the lower SiO_2 glass (~2.5 wt % FeO compared to ~1 wt %), since the relative brightness of a material in SEM-BSE is a function of mean atomic number (higher-mean atomic number materials are brighter).

The diffusion coefficient calculated using the Arrhenius equation of Baker (1991) range from $4.18*10^{-15}$ at 700°C to $1.67*10^{-13}$ at 1000°C. The characteristic diffusive length scale ($L = 2\sqrt{Dt}$) ranged from 0 to 2.3 μm from all profiles measured (n=77; average 0.81 μm). Based on the calculated temperatures using zircon saturation thermometry for these two glasses, an average temperature of 900°C was selected to estimate timescales (**see 4.1.1 Zircon and Apatite Saturation Thermometry**). Calculated timescales of relaxation ranged from 10 s to effectively 0 seconds (0.0001s), suggesting very short time of contact.

Two elemental maps were selected where the glass of 66 wt % SiO_2 was preserved rimming a phenocryst within the host glass matrix of 72 wt % SiO_2 (**Figure 20**). A total of 3733 EDS map frames at 10 μs/pixel were collected for Map 1 and at a resolution of 0.25 microns per pixel (**Figure 21**); two diffusional profiles were selected and graphed to show how the characteristic diffusive length scale varies depending on location of the profile selected. Map 2 was imaged at a different location and for 8000 frames (10 μs/pixel, resolution of 0.25 microns per pixel); although the spatial resolution increased, the diffusive length scale and times calculated did not change (**Figure 22**). **Table 4** includes a summary of the times calculated for

the four profiles with varying temperatures (700 – 1000 °C at 100 °C intervals). Further discussion on the interpretation and implications of these calculated timescales is continued in the next section.

Potential uncertainties with the timescales calculated could arise from two different sources. First, since the equation of Baker (1991) used to calculate the diffusion coefficient is based on experimental data, it is possible that this equation is not sufficient to model conditions of diffusion between these natural glasses. Another source of error could arise from the imaging technique, such that the spectral resolution of the detector could lead to blurring of contacts.

Though temperature is known to have a significant effect on diffusivities, for the diffusion lengths measured, the resulting times vary negligibly with varying temperatures (700-1000 °C), as it is apparent in **Table 3**. The difference in increasing total acquisition times also had little effect on diffusive length scales calculated from diffusion profiles, and therefore on timescales calculated (Map 1 versus Map 2).

Table 3.

T (°C)	Diffusion Coefficient	Map A Profile A		Map A Profile B	
		L (um)	Time (s)	L (um)	Time (s)
700	4.18E-15	1.57	147.0	6.37E-04	2.43E-05
800	1.80E-14		34.1		5.66E-06
900	6.01E-14		10.2		1.69E-06
1000	1.67E-13		3.7		6.10E-07

Table 3. Summary of timescales calculated for each diffusion profile at varying temperatures. 900 °C was selected to estimate timescales of diffusion based on average temperatures calculated from zircon and apatite saturation thermometry between the A-B glasses of WSB Fo 31.

Table 3 cont.

T (°C)	Diffusion Coefficient	Map B Profile C		Map B Profile D	
		L (um)	Time (s)	L (um)	Time (s)
700	4.18E-15	0.03	6.67E-02	0.9	48.6
800	1.80E-14		1.55E-02		11.3
900	6.01E-14		4.64E-03		3.4
1000	1.67E-13		1.4		0.8

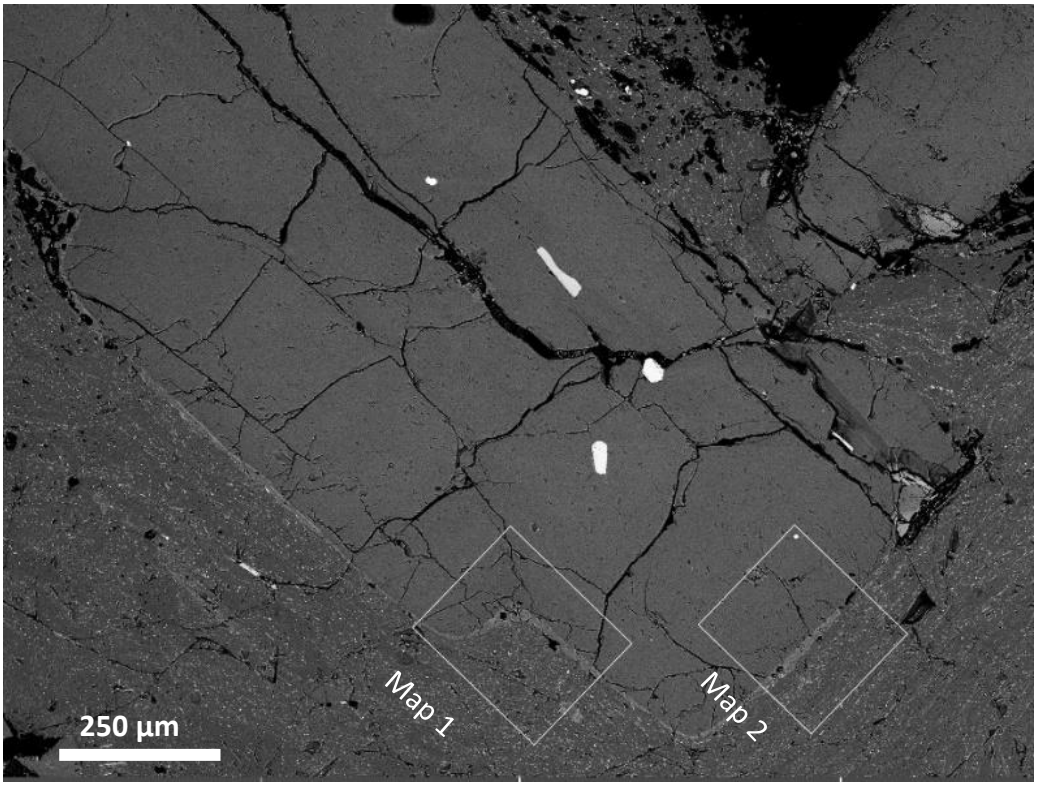

Figure 20. Large plagioclase phenocryst within fiamme of WSB Fo 31 that contains three individual glass populations. Plagioclase has a thin rind of lower, ~66 wt % SiO_2 glass (Group A), surrounded by a host matrix of the ~72 wt % SiO_2 (Group B) glasses. Outlines show areas of maps selected for SEM-EDS map. Two profiles are fitted to each contact to estimate timescales of diffusion.

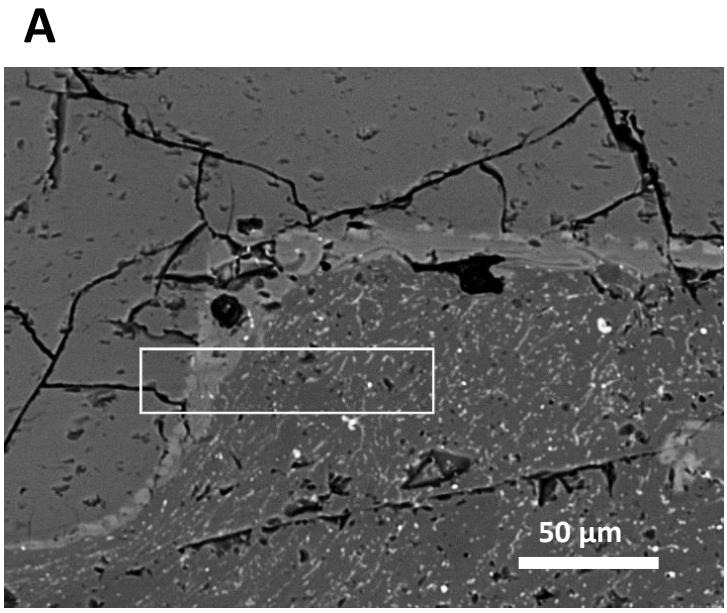

Figure 21. (A) SEM-BES image of area showing outline of EDS-Map 1; (B) Profile A location with corresponding diffusional profile and calculated characteristic diffuse length scale and time; (C) Profile B. Both images have a resolution of 0.25 microns per pixel

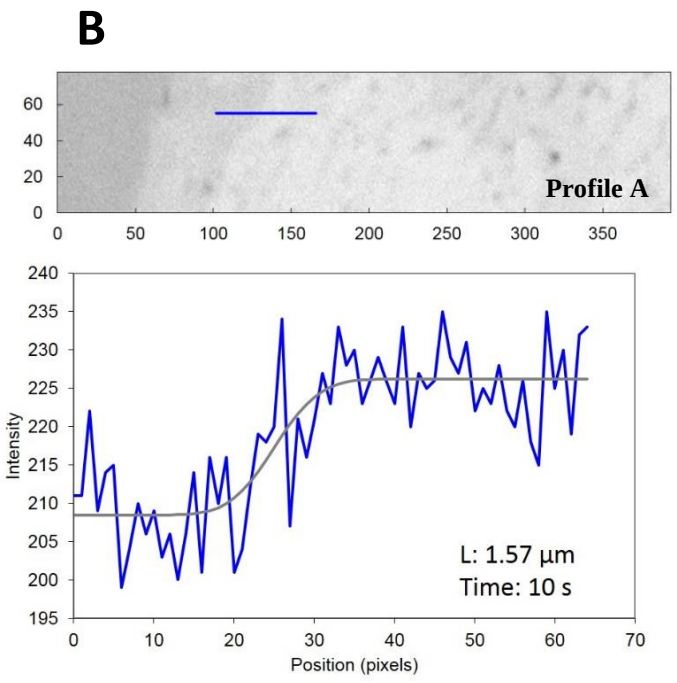

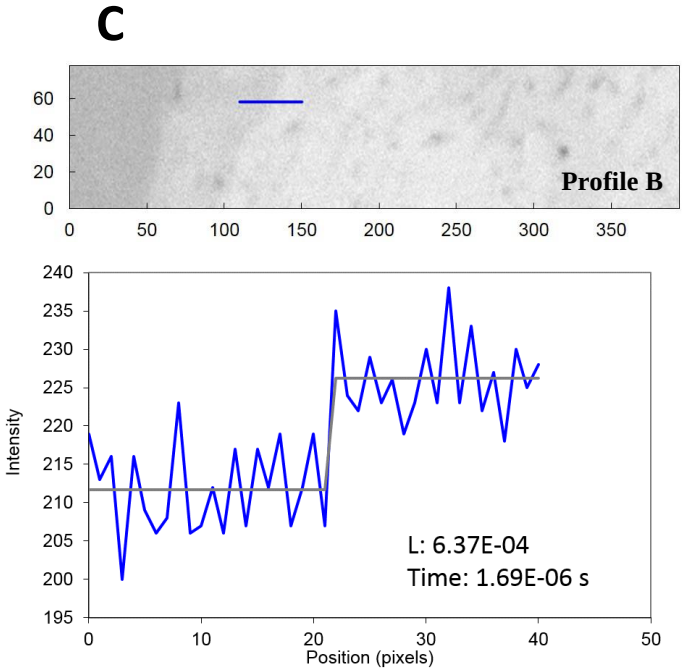

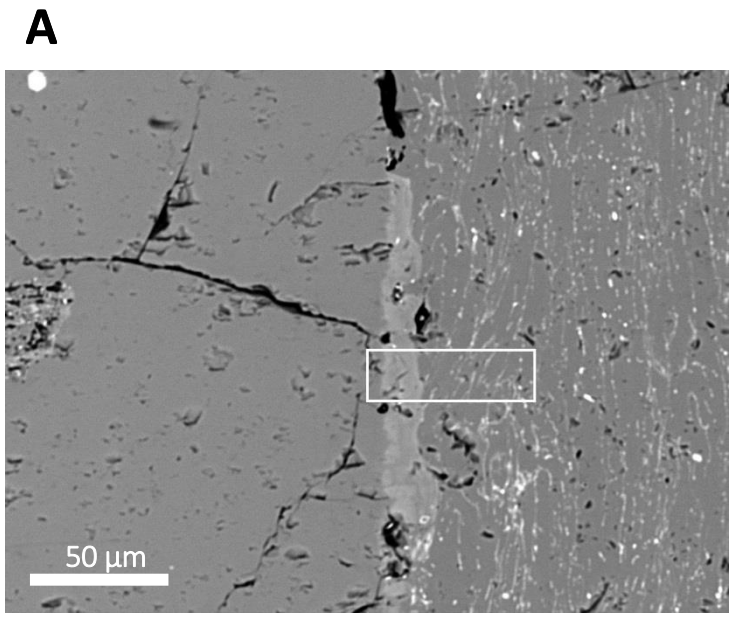

Figure 22. (A) SEM-BES image of area showing outline of EDS-Map 2; (B) Profile C location with corresponding diffusional profile and calculated characteristic diffuse length scale and time; (C) Profile D. Both images have a resolution of 0.25 microns per pixel

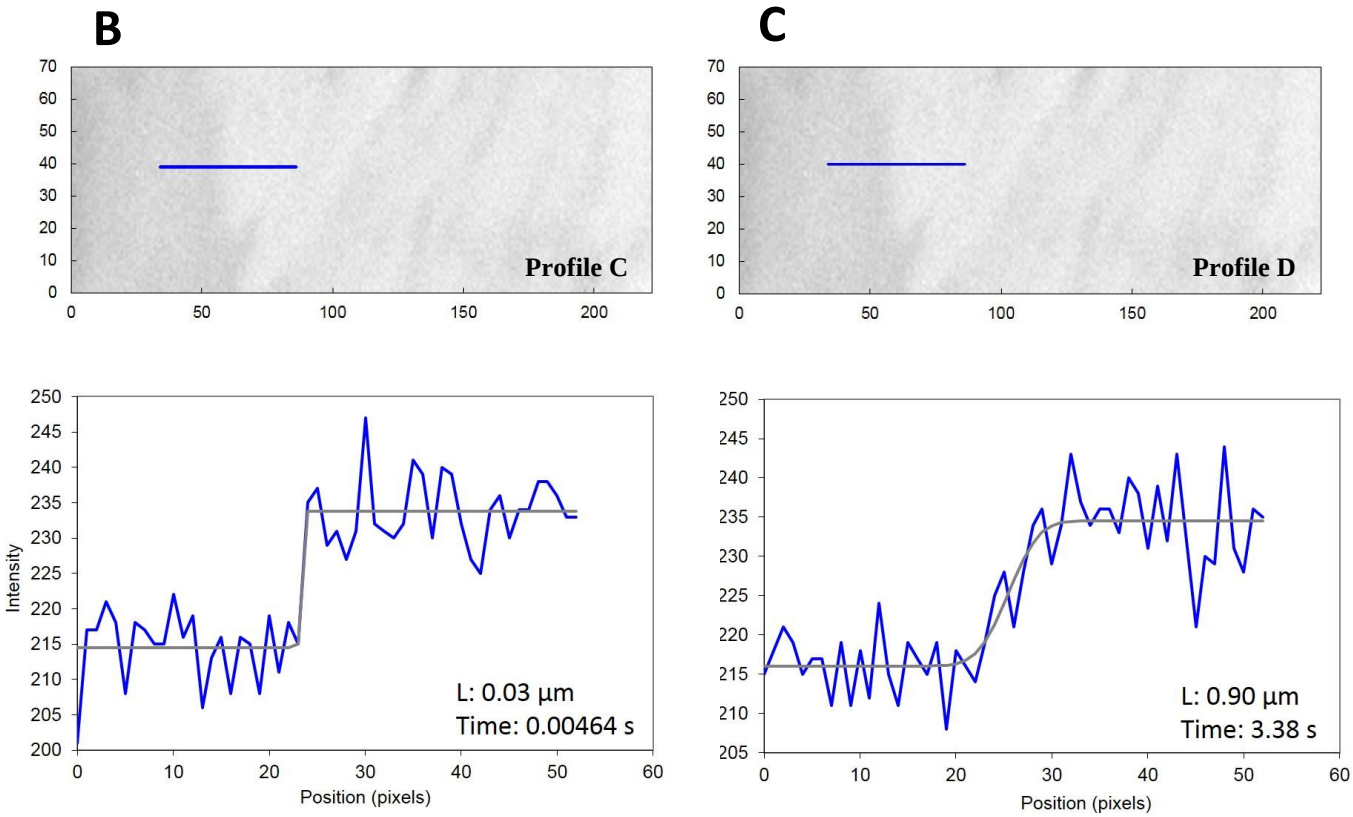

CHAPTER 4

DISCUSSION

The data presented above are combined in this section with the observations and results of previous petrological and geochemical work to test, expand upon, and refine interpretations and speculations concerning processes in the PST chamber prior to, and possibly during, eruption. Previous relevant studies include:

(1) The textural and geochemical study from Pamukcu et al. (2013) of outflow (distal and proximal) and intracaldera tuff proposed that the magmatic plumbing system that fed the eruption was zoned in composition, texture, and temperature – where the intracaldera trachyte represents the remobilized cumulate of the PST. Their results showed that the inferred shallower portions of the system had a relatively simple cooling history prior to eruption, in contrast to deeper portions that experienced a major late-stage heating event. They suggest that a decompression event probably occurred very near the time of eruption.

(2) Frazier (2013) evaluated the petrogenetic processes by which the PST magma was formed. Whole rock Nd, Sr, Hf, and Pb and zircon Hf and O isotope compositions of the trachytic (intracaldera and outflow) and rhyolitic outflow PST are almost indistinguishable. Isotopic data are consistent with the interpretation that the elemental and textural distinctions between early and late-erupted material were generated by crystal-melt segregation post original emplacement of the PST magma body in the shallow crust (closed system processes).

(3) Barry et al. (2015) analyzed bulk-rock geochemistry of tuff samples from all five zones of the PST at and near Kingman. Their results showed that the lower four are relatively homogeneous in major and trace elemental chemistry whereas the upper Tp5 is distinctly and uniquely trachyte. The tuffs that comprise the lower four zones increase upward in phenocryst content from ~5 to 20% and increase in pumice size and abundance. Paleomagnetic data confirms the interpretation of a single, short-lived eruptive pulse for the entire eruption of the PST.

(4) Pamukcu et al. (2015) applied a series of geobarometry techniques to the high-silica rhyolite PST in Tp3. Pressure estimates using rhyolite-MELTS phase-equilibria geobarometer range from 185 to 230 MPa, based on the equilibrium between melt, quartz, and two feldspars and using matrix glass compositions of the high-silica rhyolite PST. Rhyolite-MELTS estimates are consistent with estimates based on projection onto the haplogranitic ternary (250 ± 50 MPa). Amphibole-geobarometry gave pressure ranges of ~220, 210, and 190 MPa (Anderson & Smith (1995), Blundy & Holland (1990), and Holland & Blundy (1994), respectively).

Below we expand on the observations and interpretations established in previous studies.

4.1 Estimated Pre-Eruptive Conditions

4.1.1 Zircon and Apatite Saturation Thermometry

Zircon and apatite saturation temperatures based on average glass compositions are summarized in **Table 4 (**zircon: calibrations of both Watson & Harrison (1983) and Boehnke et al. (2013); apatite: Harrison & Watson 1984). Zircon temperatures calculated from Watson & Harrison (1983) are higher than those using Boehnke et al. (2013). The discrepancy between the

results yielded by the two calibrations is temperature sensitive: relatively small at higher temperatures (~25 °C at ~900 °C), but systematically increasing toward lower T (~50 °C at ~750 °C)(Table 5; Boehnke et al. 2013). Temperatures estimated by apatite saturation thermometry are broadly similar to the calculated zircon saturation temperatures. The three high-silica rhyolite glasses (Low-Zr rhyolite) (KWF Fo 1E, KWF Fo 2A, and KWF Fo 3B) yielded zircon saturation temperatures of 763-771 and 713-722 °C (Watson & Harrison (1983) and Boehnke et al. (2013), respectively), and 745-755 ºC for apatite saturation. Temperatures for the high-silica rhyolite are consistent with those estimated by Pamukcu et al. (2013): ~742 °C (rhyolite-MELTS), 770-780 °C (zircon saturation, Watson and Harrison 1983 calibration), and 769 ± 20 °C (Zr-in-sphene, Hayden at al., 2008 thermobarometer). The trachyte glasses give higher and more variable zircon saturation temperatures: 853-921 and 814-894 °C (Watson & Harrison 1983, Boehnke et al. 2013, respectively), and 803-890 °C (apatite saturation). The samples containing multiple glass populations record strong temperature contrasts among glasses. In WSB Fo 1, the temperature difference between glasses A and B is 39 °C (921-882 and 894-852 °C, Watson & Harrison, 1983, Boehnke et al., 2013, respectively), and 25 °C (873-848 °C; apatite saturation). WSB Fo 31 shows an even greater contrast among the three glasses. The A-B-C glass zircon temperatures are 918-897-862 and 887-867-829 °C (Watson & Harrison, 1983 and Boehnke et al., 2013, respectively), and 900-890-878 °C (apatite saturation).

Table 4.

Sample	Sample Type	Zircon Saturation		Apatite Saturation
		Watson & Harrison (1983)	Boehnke et al. 2013	Harrison & Watson (1984)
WSB Fo 8	trachyte fiamma	901	872	840
WSB Fo 3	trachyte fiamma	900	874	840
MLPT 5D	trachyte pumice	862	828	880
KPP MF 5	trachyte pumice	853	814	890
SWA 01A	trachyte pumice	915	890	890
WSB Fo 20	trachyte fiamma	884	855	848
WSB Fo 23	trachyte fiamma	862	826	803
WSB Fo 3b	trachyte fiamma	886	857	848
GJ Fo 1	trachyte fiamma	889	861	858
WSB Fo 1 A	trachyte fiamma	921	894	873
WSB Fo 1 B	trachyte fiamme	882	852	848
WSB Fo 31 A	trachyte fiamme	918	887	870
WSB Fo 31 B	trachyte fiamme	897	867	890
WSB Fo 31 C	trachyte fiamme	862	829	878
KWF Fo 1E	Low-Zr pumice	771	722	750
KWF Fo 2A	Low-Zr pumice	767	717	755
KWF Fo 3B	Low-Zr pumice	763	713	745

Table 4. Zircon and apatite saturation thermometry based on glass concentrations of zirconium and phosphorous (respectively).

4.1.2 Amphibole Geobarometry

Because of its sensitivity to pressure, the composition of amphibole – specifically, the abundance of Al – has proven to be useful in geobarometry (e.g., Hammarstrom and Zen 1986). The Al-in-hornblende geobarometer is applicable to rocks containing the mineral assemblage: amphibole + plagioclase + biotite + quartz + alkali feldspar + ilmenite/titanite + magnetite + apatite. We apply a new calibration of the barometer by Mutch et al. (2016) to analyses of amphibole in our samples. These samples and analyses meet the preferred criteria for

application of the geobarometer (phase assemblage; rims of phenocrysts in apparent textural equilibrium with melt and other phenocrysts; temperatures ~725 ± 75 °C).

Pressure estimates obtained from average rim compositions of amphibole (analyzed by SEM-EDS) within pumice from each of the lower four zones of the high-silica rhyolite PST at the KWF locality range from 210 to 220 MPa (~7.6 to 8.2 km depth)(**Table 5**). In Table 6, we compare these results to those of Pamukcu et al. (2015) for outflow pumice from Tp3, which were determined using analyses by electron microprobe; the pressures range correspondingly from 190 to 220 MPa (~7.0 to 8.3 km depth). Rims of single amphibole crystals that we analyzed from three samples (GJ Fo 1, WSB Fo 31, and WSB Fo 3b) from two locations (Grasshopper Junction and Warm Springs Butte) yielded pressures of 200 to 210 MPa (~7.3 to 7.8 km depth); all three amphiboles analyzed are enclosed by high-silica rhyolite glass and each sample contains one amphibole.

Table 5

Sample	PST Zone	Analytical Method	Al wt%	Al-in-formula	Mutch et al. (2016) (MPa)	Depth (km)
GJ Fo 1	(uncertain)	SEM-EDS	6.43	1.1	210	7.6
WSB Fo 31	Tp5		6.31	1.06	200	7.3
WSb Fo 3b	Tp5		6.5	1.1	210	7.8
KWF Fo 5	Tp4		6.55	1.16	220	8.2
KWF Fo 10	Tp3		6.17	1.1	210	7.6
KWF Fo 3B	Tp2		6.73	1.15	220	8.1
KWF Fo 1E	Tp1		6.73	1.15	220	8.1
KPST01K-1	Tp3	EMP	5.96	1.03	190	7.0
KPST01K-3	Tp3		6.73	1.16	220	8.3
KPST01K2-1	Tp3		6.49	1.12	210	7.9
KPST01K2-2	Tp3		6.45	1.11	210	7.8
KPST01K2-3	Tp3		6.1	1.05	200	7.2
KPST01K2-7	Tp3		6.32	1.09	210	7.6
KPST01K2-13	Tp3		6.18	1.07	200	7.4
KPST01K2-14	Tp3		6.62	1.14	220	8.1
KPST01K2-15	Tp3		6.24	1.08	200	7.4
KPST01N2-1	Tp3		6.61	1.14	220	8.1

Table 5. Pressure calculations based on Al-in-hornblende geobarometer (Mutch et al 2016) for PST high-silica rhyolite outflow zones. KWF samples from this study, KPST01K and KPST01N samples from Pamukcu et al 2015.

4.1.2 Bulk Water Content

Rhyolite-MELTS model simulations using bulk whole-rock compositions (WSB Fo 3, WSB Fo 1, WSB Fo 20, and WSB Fo 23) suggest a water content of ~2 wt % H_2O for the magmas represented by the trachyte fiamme. The MELTS results at this water content are within range of appropriate crystal-liquid proportions (30-40 vol % solids), temperature (850-900°C), glass composition (70 – 72 wt % SiO_2), and pressure (assuming a deeper estimate for the cumulate of ~230 MPa; based on Pamukcu et al. 2015) (**Figure 23**). Estimates of H_2O content

are consistent with those of Pamukcu et al. (2013) for rhyolite-MELTS simulations of bulk water content (~1 wt%) for intracaldera trachyte fiamme; deciding upon 1 versus 2 wt % H_2O is primarily dependent upon the model confining temperature (> 900 °C versus < 900 °C), which likely varied in space and time.

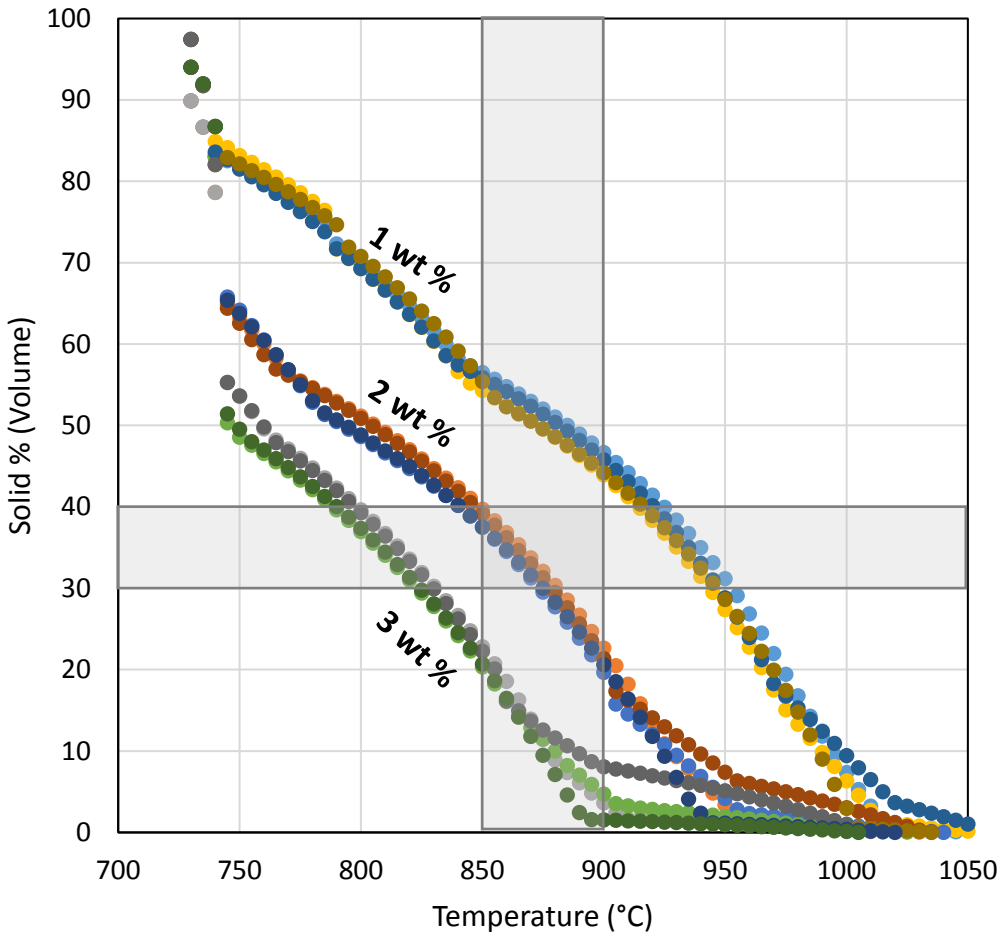

Figure 23. Rhyolite-MELTS simulations modeling four bulk whole-rock compositions at varying water content (1, 2, and 3 wt % H2O). Range of temperatures from mineral saturation thermometry for all four samples is ~850-900°C at a solid fraction of ~30-40 % vol.

4.2 Crystal Accumulation

This study adds substantially more whole-rock analyses to the existing data set for PST, especially for outflow trachytes, and it provides the first large set of trachytic glass analyses and the first data for zones Tp1, Tp2, and Tp 4 (glass analyses for Tp 1 and Tp2 and phenocryst compositions for all four zones) (Pamukcu et al., 2015, presented a large data set from Tp3). With these additional data we can evaluate more fully and add detail to previous models of crystal accumulation and subsequent heating. We also present the first trace element models to evaluate the plausibility of the cumulate hypothesis.

The major and trace element compositions of the trachytes and high-silica rhyolites are consistent with expectations for cumulates and extracted melts, respectively, given the observed phenocryst assemblages (e.g. Bachl et al., 2001; Deering & Bachmann, 2010). The bulk fiamme compositions of the trachytes are extremely rich in feldspar and accessory mineral components (e.g. concentrations up to 1421 ppm, 239 ppm Sr, 629 ppm Zr, and 432 Ce in trachytic fiamme) (**see Fig 12**), supporting accumulation (Pamukcu et al., 2013). The considerable compositional variation seen across trachyte bulk fiamme and pumice concentrations does not require mixing with a separate more mafic magma. The variability can either be attributed to varying proportions of phases in the cumulate(s) – that is, the phases were likely not accumulated in uniform proportions – and/or to variable effectiveness of melt extraction (crystal-melt segregation) during the remobilization process.

4.2.1 Trace Element Modeling

The variability in concentrations between whole-rock trachyte and the HSR rhyolite compositions can be explained by in-situ differentiation – where the cumulate represents the crystal-enriched, melt depleted residue from which melt was extracted to produce the crystal-poor, high-silica rhyolite magma of the PST. Results from the simple trace (dispersed) element model for fraction crystallization show that the modeled elements match the compositional patterns of the proposed products (**Figure 24**).

We assume perfect fractional crystallization from melt with the composition of mean PST magma. The starting point was a uniform parental PST melt with the composition of mean PST ignimbrite estimated from major and trace element analyses of pumice and fiamme (**Table 2c**). We further assume that the crystals that grew from this parental melt did not equilibrate internally, such that perfect fractional crystallization was achieved, and that they accumulated to form the crystal-rich cumulate represented by trachyte pumice and fiamme. While this cannot be entirely accurate, this assumption of fractional crystallization is most closely representative of processes taking place at shallower, and presumably faster crystallization processes. This model cumulate contained trapped melt with the composition of mean outflow HSR rhyolite. In the model, the remainder of this evolved melt formed a crystal-poor cap that is represented by the voluminous outflow rhyolite.

The trace element model shows elemental enrichments and corresponding depletion in the model cumulate and extracted melt, relative to estimated mean trace-element concentrations in HSR and trachyte pumice and fiamme. The model patterns all follow the general trend of the observed HSR and trachyte (cumulate?) compositions, with depletions in Sr, Ba, Zr, and light and middle REE and enrichment in U, Th, Nb, and Rb model melt and HSR and complementary

enrichments and depletions in model cumulate and trachyte. Those models generated based on PST bulk magma with proportions of ~60% HSR ~10% LSR, and ~30% trachyte most closely reproduce the patterns of the trachyte and HSR rhyolite.

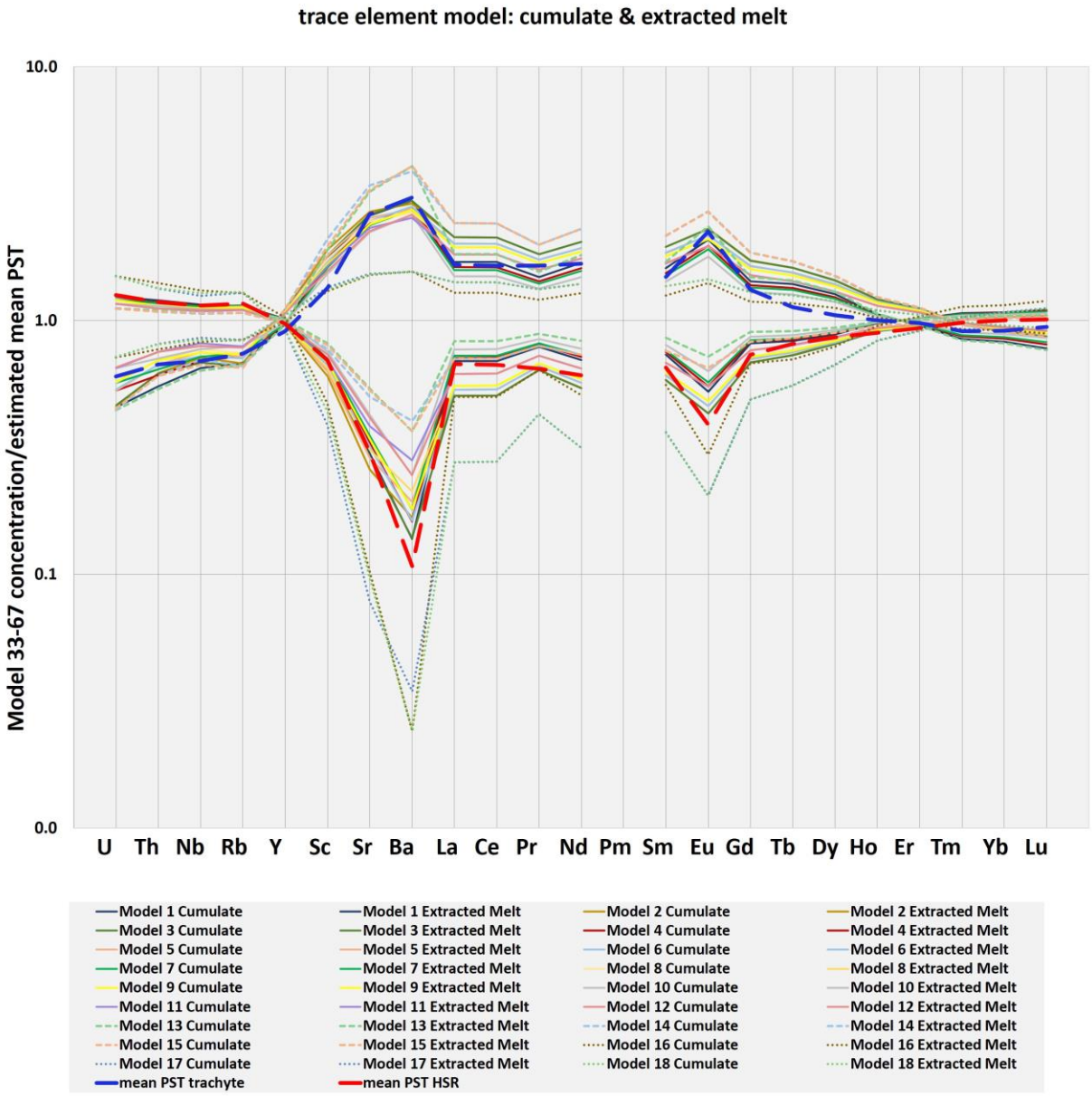

Figure 24. Model cumulate and extracted melt elemental concentrations are plotted as ratios to the concentration of the estimated mean PST. Trace element model supports the notion of the Low-Zr melt of the PST deriving from melt extraction from a crystal-rich cumulate. Explanation for each model is found in **Table 6**.

Table 6

Key	Parental PST bulk magma and Bulk D Mode
Model 1	HSR~60%, Trachyte~30%, LSR~10%, 2% H2O , Bulk D Mode #1
Model 2	HSR~60%, Trachyte~30%, LSR~10%,, 2% H2O , Bulk D Mode #2
Model 3	HSR~60%, Trachyte~30%, LSR~10%,, 2% H2O , Bulk D Mode #3
Model 4	HSR~60%, Trachyte~30%, LSR~10%,, 3% H2O , Bulk D Mode #1
Model 5	HSR~60%, Trachyte~30%, LSR~10%,, 3% H2O , Bulk D Mode #2
Model 6	HSR~60%, Trachyte~30%, LSR~10%,, 3% H2O , Bulk D Mode #3
Model 7	HSR~60%, Trachyte~30%, LSR~10%,, 4% H2O , Bulk D Mode #1
Model 8	HSR~60%, Trachyte~30%, LSR~10%,, 4% H2O , Bulk D Mode #2
Model 9	HSR~60%, Trachyte~30%, LSR~10%,, 4% H2O , Bulk D Mode #3
Model 10	HSR~60%, Trachyte~30%, LSR~10%,, 5% H2O , Bulk D Mode #1
Model 11	HSR~60%, Trachyte~30%, LSR~10%,, 5% H2O , Bulk D Mode #2
Model 12	HSR~60%, Trachyte~30%, LSR~10%,, 5% H2O , Bulk D Mode #3
Model 13	HSR~75%, Trachyte ~15%, LSR ~10% , 3% H2O , Bulk D Mode #1
Model 14	HSR~75%, Trachyte ~15%, LSR ~10% , 3% H2O , Bulk D Mode #2
Model 15	HSR~75%, Trachyte ~15%, LSR ~10% , 3% H2O , Bulk D Mode #3
Model 16	HSR~25%, Trachyte ~65%, LSR ~10% , 3% H2O, Bulk D Mode #1
Model 17	HSR~25%, Trachyte ~65%, LSR ~10% , 3% H2O, Bulk D Mode #2
Model 18	HSR~25%, Trachyte ~65%, LSR ~10% , 3% H2O, Bulk D Mode #3

Table 6. Model explanation; The trace elements for both the model cumulate and extracted melt are generated using a parental PST magma (Frazier, 2013) with varying water content, a Bulk D, Padilla & Gualda (2016) partition coefficients calculated for the PST. HSR = Low-Zr samples; LSR = High-Zr in this study.

4.3 Reheating

Petrographic and chemical evidence presented by Pamukcu et al. (2013) and in this study indicates that the trachyte was subjected to reheating shortly before eruption, presumably a result of injection of hotter, more mafic magma. Pamukcu et al. (2013) documented Ti enrichment in zircon edges in intra-caldera trachyte fiamme that suggests temperatures during final growth exceeded ~900 °C, far hotter than initial growth of these crystals, and also much hotter than the crystallization temperatures for zircon in outflow. These authors also identified edges in sphene that are REE- and Zr-enriched relative to crystal cores. These characteristics suggest a reheating event with higher temperatures that resulted in resorption of REE-rich sphene and chevkinite (Pamukcu et al., 2013).

The increase in temperature is also indicated by the resorbed and embayed shapes of the phenocrysts present to varying degrees in all trachytic samples. The partial dissolution of phases led to the variable, often extreme, enrichment of elements in the melt (glass) that accompanied partial dissolution of feldspars, biotite, and accessory phases (e.g. up to ~4000 ppm Ba, 400 ppm Sr, 800 ppm Zr, 900 ppm P, 500 ppm Ce).

Huber et al. (2012) suggest a substantial amount of enthalpy is required in large systems for the reactivation of a cumulate. The variability of trace element concentrations together with variable temperatures on sample to sample scale shows the inefficiency of heat transfer and that adequate time post-rejuvenation was not reached in order to fully attain homogeneous compositions.

4.4 Compositional Variability and Local Evidence for Open-System Processes: Consequences of Dynamics of Cumulate Remobilization

Mafic input, indicated by the presence of sparse but widespread mafic magmatic enclaves (basaltic andesite, andesite) in outflow (Pamukcu et al., 2013; Flansburg et al., 2014; Flansburg, 2015), probably provided the necessary heat for sufficient partial dissolution to remobilize the cumulate. It is important to evaluate the possibility of mafic magma input as a potential contributor to compositional heterogeneity of melt in the trachyte magmas, recorded in glass compositions.

Two mechanisms could have led to geochemical heterogeneities in melt compositions as a result of a reheating event. One hypothesis suggests that heterogeneity was a result of mingling and effective diffusive mixing of a hotter, more mafic magma with the resident rhyolitic PST magma. The alternative hypothesis is that geochemical heterogeneities in melts were a consequence of partial melting (dissolution) of the cumulate crystal-mush of the PST, following mafic magmatic underplating (cf. Huber et al., 2011; Sliwinski et al., 2017). The high-T melts of crystal-enriched cumulate would differ from the dominant rhyolite melt, and variations in temperature and potentially in bulk composition within the cumulate would lead to further variability.

Significant chemical (diffusive) mixing is unlikely for several reasons. First, in the PST we do not see large-scale evidence for a mingling event. A far greater volume of relatively mafic magma input than observed enclaves in the outflow would be required to accomplish the magnitude of heating that is evident in the trachyte, suggesting that most of the putative mafic input remained at deeper levels. Furthermore, elemental enrichment patterns of the trachyte

glasses compared to rhyolite glasses are inconsistent with substantial addition of mafic melt components. Also, the lack of wide-spread dissolution and resorption in the high-silica rhyolites indicates that the heating event was not felt by the entire system (Pamukcu et al., 2013). Finally, whole rock and zircon isotope compositions for all PST compositions (trachyte, High-Zr rhyolite and Low-Zr rhyolite) are relatively homogenous and very different from those of plausible mantle-derived magmas, inconsistent with appreciable mafic chemical input (McDowell et al., 2016; Frazier, 2013).

The chemically closed system hypothesis requires no physical mixing between the PST magma and the inferred mafic magma, only an influx of heat from the underplating intrusion. The case for underplating versus physical mixing is also reasonable since density and rheological contrasts between the invading and resident magmas would inhibit upward propagation of the more mafic magma; therefore, cumulate remelting likely occurred with minimal mass transfer.

We interpret the compositions of trachyte phenocrysts and glasses as recording significant reheating, partial dissolution of the accumulated phases, and late self-mingling. The evidence for partial dissolution of trachyte phenocrysts suggests that a reduction in crystal fraction following magma recharge played an important role in reactivation. The observed phenocryst content is much lower than the expected crystal fraction at the time of initial melt extraction from cumulate. Pamukcu et al. (2013) estimated a melt fraction of ~15-20% prior to reheating, suggesting that close to 50 wt % of the cumulate crystals dissolved during the heating event, assuming the cumulate was mobilized *en masse* to form the ~35% phenocryst-65% liquid trachyte magma. This crude estimate assumes the original trapped melt within the cumulate was at or near water saturation (~5.5 wt % SiO_2) and that the bulk cumulate as a whole contained ~1 wt % H_2O (based on rhyolite-MELTS modeling).

Variability in dissolution textures in phenocrysts and the large range of glass trace element concentrations suggest that phenocrysts responded in diverse ways to reheating. This is likely to reflect uneven heating, which may have been a function of the geometry of mafic intrusion into the cumulate and/or a variable pattern of repeated recharge events. The thermo-mechanical reactivation of the crystal mush would have led to heterogeneities in degree of partial dissolution of the crystal mush due to ineffectiveness of heat transfer from an underplating mafic injection (Huber et al., 2011).

The textures and range of compositions found in the two samples containing multiple glass populations suggest that these melts were interacting prior to eruption and the preservation of heterogeneities can be used to constrain timescales of reactivation. The rare phenocrysts and clusters of phenocrysts encompassed by less silicic glass within a more silicic host glass appear to represent fragments of more intensely heated cumulate that were entrained during eruption. The extremely short timescales indicated by the sharp compositional contacts between the contrasting glasses support this idea of very rapid entrainment and subsequent cooling. Even though the times calculated from the diffusional modeling appear to be unrealistically short, the sharpness of the boundaries strongly imply very short timescales.

Cohesive cumulate fragments indicate that crystal-rich magmas can be entrained and transported during the eruption processes. Sliwinski et al. (2017) suggested that small fragments of mush located immediately above the reactivated portion of the mush are likely to be entrained during eruptions. This overpressure build-up within the barely rigid portion of the mush positioned at the reactivation front can mechanically destabilize portions of the mush, permitting entrainment during eruption (Huber et al., 2011).

4.5 Possible Eruption Trigger

It is apparent that the PST cumulate experienced a late-stage heating event, which may have contributed to the onset of eruption. The presence of hotter recharge magma at the base of the cumulate is supported by textural, mineralogical, and geochemical features indicative of reheating (e.g. crystal dissolution indicate be phenocryst textures and compositions of trachytic glasses, high Ti-rim growth on zircons, high zircon and apatite saturation temperatures for the trachyte glasses) as well as by the presence of sparse mafic magmatic enclaves.

Rejuvenation is associated with reduction of the crystal fraction below the mechanical locking point by partial dissolution of crystals as a result of hot replenishment. This increase in melt fraction decreases effective viscosity and, owing to volume increase, increases the internal overpressure within the cumulate mush (e.g. "mush defrosting" of Mahood, 1990; Sliwinski et al., 2017). Overpressurization is commonly credited as the eruption triggering mechanism for many other supereruption scaled systems (e.g. Ammonia Tanks Tuff, Deering et al., 2011; Carpenter Ridge Tuff, Bachmann et al., 2014).

Overpressurization resulting from a rejuvenation event requires sufficient transfer of heat. The effect that a single replenishing event will have on the cumulate depends on several factors, including the relative size, the geometry, and the compositions of both the recharge magma and the cumulate mush as well as the average crystal fraction of the mush. Although rejuvenation likely results from a replenishment event (given the right conditions), rejuvenation within the chamber does not necessarily require replenishment (e.g. external forces - earthquakes).

Considering that these large systems almost certainly experience multiple replenishment and subsequent rejuvenation events over their thermal lifetime that do not trigger eruptions – or

at least not large eruptions – the question arises of what specific conditions are necessary for triggering of supereruptions. Evidence of large scale mafic input and mingling is common in the plutonic record, notably including examples in Miocene intrusions of the Colorado River extensional corridor (e.g. Aztec Wash, Falkner et al., 1995 and Harper et al., 2004; Post-PST caldera intrusion, McDowell et al., 2014), yet indications of their erupted volcanic counterparts are less common, including in the PST. As pointed out in Tramontano et al. (2017), the conditions for triggering an eruption requires a series of events where the system is already in a state prone to eruption.

4.6 PST as a Modified "Standard Model"

Ignimbrites that show gradational compositional zoning from early- to late-erupted deposits are a common product of supereruptions (Bachmann & Bergantz, 2008b). Well-studied examples include the Bandelier Tuff (Wolff & Ramos, 2003), the Carpenter Ridge Tuff (Bachmann et al., 2014), and the Huckelberry Ridge Tuff (Wilson, 2008). Field relations in these cases demonstrate that the initial eruption taps crystal-poor rhyolitic melt and that later the eruption transitions to a more crystal-rich, less-differentiated magma. The geometry most commonly inferred from these zoned deposits is a single chamber that comprises a melt-rich cap that grades to an underlying crystal-rich cumulate zone, recently referred to as the "Standard Model" (Gualda & Ghiorso, 2013).

Two alternative models to the simple, single chamber (Standard Model) envision reservoirs with either vertically stacked chambers or with multiple discrete bodies that are separated laterally and/or vertically. The "stacked chamber" model of Bindeman & Valley

(2003) (see also Deering et al., 2011) for the Ammonia Tanks tuff proposes that the cumulate and melt-rich cap erupted sequentially from two distinctly different chambers. The cumulate remains in a lower chamber until erupted after the extracted melt-rich magma erupts from an upper chamber. This model is consistent with eruptions sequence of the PST.

A second alternative postulates a "complex magma reservoir configuration," where multiple discrete magma lenses are tapped during eruption. The discrete magma bodies have little to no connection and are distributed laterally and/or vertically (e.g. Cooper et al., 2012; Cashman & Giordano, 2014; Bishop Tuff, Gualda & Ghiorso (2013); Taupo Volcanic Zone; Bégué et al., 2014). Although we cannot rule this possibility out, we see no evidence to support it, and the strong evidence suggesting a direct connection between trachyte cumulate and high-silica rhyolite is difficult to explain in the complex reservoir model.

The simplest reservoir geometry to explain the Peach Spring Tuff remains a version of the Standard Model: a single, relatively simple, vertically stratified chamber with a crystal-rich base and massive high-silica crystal-poor upper zone (Pamukcu et al., 2013). The field relations are consistent with a single magma chamber, where the abrupt composition gap between PST high-silica rhyolite outflow and overlying Tp5 and intracaldera trachyte suggesting top-down evacuation of the initial, crystal-poor high silica rhyolite cap and ending with the crystal-rich basal mush. The stacked-chamber model also works but the added complexity is not required. As noted in the preceding paragraph, the complex reservoir model cannot be ruled out, but it appears to create unnecessary complication and we see no evidence that would favor it over the Standard Model.

Our model of rhyolite melt extraction (PST outflow) from cumulate crystal mush of intermediate composition (trachytic pumice) is shown in **Figure 25.** Given an estimated caldera

diameter of ~26 km (Ferguson et al., 2013) and an estimated erupted volume of ~1000 km^3, we calculate a ~2 km thickness for the erupted PST magma body. The relatively narrow range of pressures in Pamukcu et al. (2015) for Tp3 together with amphibole barometry for the high-silica rhyolite from Tp1-Tp4 is consistent with the suggestion that magmas involved in large, caldera-forming supereruptions are typically stored in sill-like bodies, with aspect ratios of 1/5 to 1/10 (Bachmann & Bergantz, 2008b). A sill-like geometry supports the model of melt extraction from the cumulate in generating a large volume cap of crystal-poor rhyolitic melt on geologically relevant timescales (~10^5 y) because it optimizes melt extraction by reducing the average vertical distance traveled by the viscous melt (Bachmann & Huber, 2016).

In our interpretation, the reheating of the crystal-rich "rigid sponge" by injection of mafic magma reduced melt fraction sufficiently to "unlock" the rigid material at the base of the chamber (**Figure 25b**). The reheating event generates the thermal gradient and leads to a reduction in crystal fraction by partially dissolving crystals in the magma chamber prior to eruption. It is also clear that the eruption of the cumulate followed the initial eruption of the HSR, but whether the eruption of the cumulate was synchronous with the caldera collapse is unclear (e.g. caldera collapse at Ossipee ring dyke, New Hampshire; Kennedy & Stix, 2007).

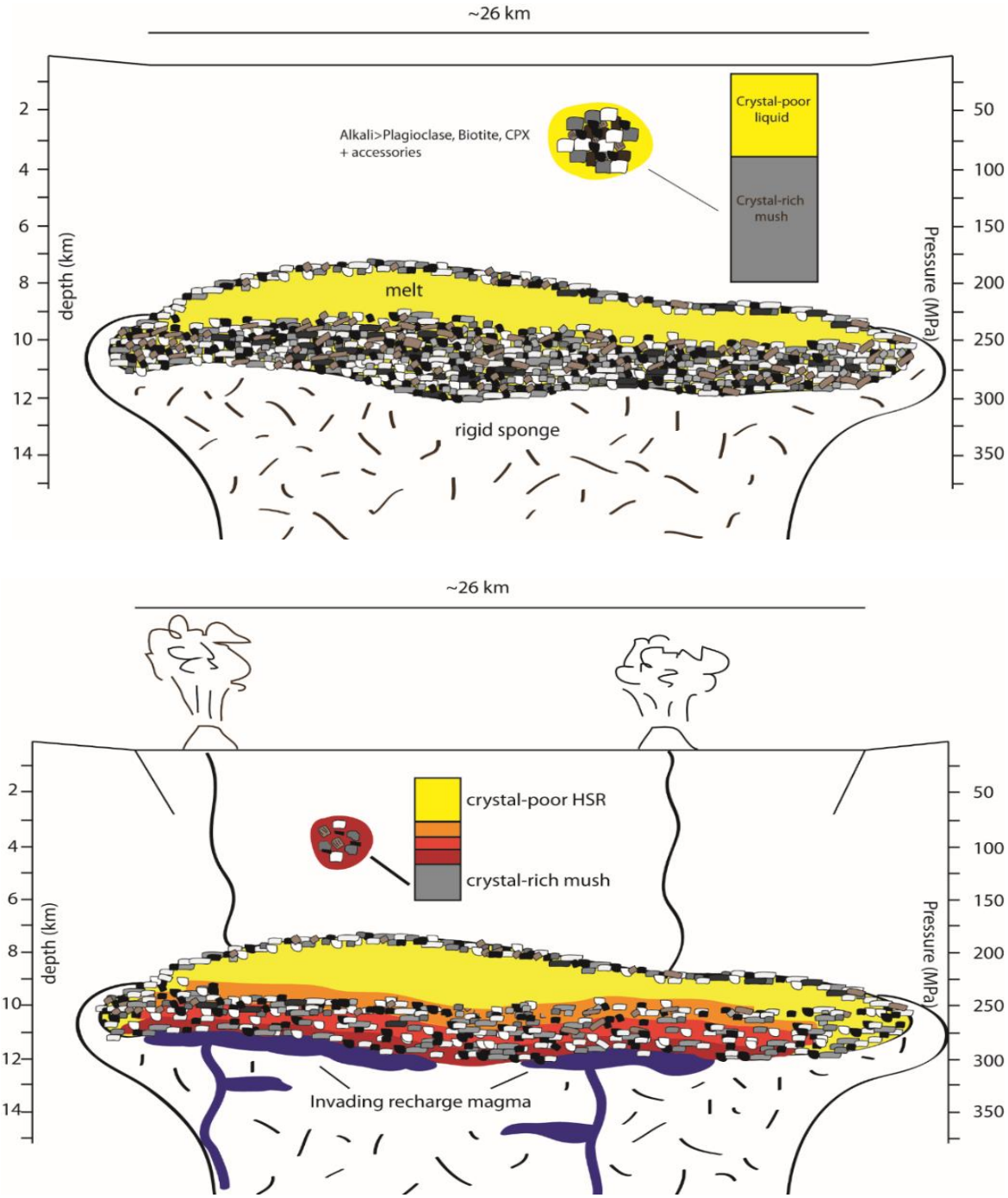

Figure 25. (A) Initial conditions of melt extraction from a crystal-rich basal cumulate generating a thin cap of evolved crystal-poor melt; (B) Invading recharge magma leads to partial dissolution of cumulate phases; uneven heat transfer from underplating hotter, more mafic recharge generates variability in elemental enrichment and temperatures recorded in the melt. The crystal fraction is sufficiently reduced for eruption of the cumulate, following the eruption of the high-silica rhyolite PST.

CHAPTER 5

CONCLUSIONS

Crystal accumulation and efficient melt extraction, followed by partial dissolution of cumulate and consequent remobilization, represent the main processes responsible for the generation of contrasts (compositional, crystal-fraction, and thermal) seen in the PST. The zonation of the PST magma body and geochemical characteristics of the magma can be inferred from the eruption sequence, phenocryst assemblage and abundance, and elemental data. The textures and variable geochemical signatures reveal the dynamics of processes relating to the assembly and disassembly of the cumulate mush of the PST.

Summary of PST events and processes:

(1) Crystal Accumulation and Melt Extraction (**Figure 25A**): The major and trace element compositions of the trachytes and high-silica rhyolites are consistent with expectation for cumulate and extracted melts, respectively, given the observed phenocryst assemblage; this notion is supported by the trace element models for trachyte as cumulate and HSR as extracted melt from an initial parental PST composition. The variability in whole-rock concentrations can be attributed to varying proportions of phases accumulated in the cumulate(s) and/or variable effectiveness of crystal-melt segregation.

(2) Reheating and Rejuvenation (**Figure 25B**): Petrographic and chemical evidence suggest that the trachyte was subjected to reheating shortly before eruption. The reheating led to partial dissolution of phases shown as variable disequilibrium textures, including resorbed and embayed

shapes of the phenocrysts. It also led to extreme enrichments of elements in the melt (glass) (e.g. Ba, Sr, Zr, P, and Ce). The variability in elemental enrichments along with variable temperatures recorded in the glasses (e.g. zircon and apatite saturation thermometry) suggests that heat transfer from a hotter, more mafic magma was inconsistent. We see no field or petrographic evidence of a large-scale mingling event with the replenishing magma. Furthermore, the isotopic compositions for PST whole rocks and zircons are relatively uniform, suggesting closed system processes. The geochemical heterogeneities in the melt composition are likely a result of partial dissolution of the cumulate crystal-mush following heating resulting from mafic magmatic underplating.

(3) Eruption (**Figure 25C, 25D**): The late-stage heating event likely contributed to the onset of eruption. This event provided the thermal energy necessary to reduce the crystal fraction below the mechanical lock point via partial dissolution of phases, sufficiently decrease effective viscosity and increase the internal overpressure within the cumulate mush. Eruption triggering resulting from destabilization of the cumulate could have initiated the eruption of the high-silica rhyolite portion of the chamber.

(4) We propose a single, relatively simple chamber geometry for the PST where the high-silica rhyolite chamber directly overlies the cumulate base. The eruption of the high-silica rhyolite is interpreted to represent a single, geologically instantaneous event, with the eruption taking place for a minimum of 2.5-10 hours (Roche et al., 2016). The eruption of the cumulate (outflow Tp5 and intracaldera) may have been synchronous with the caldera collapse.

(5) Timescales (**Figure 25E**): Tp5 fiamme record sharp compositional contacts between contrasting glasses consistent with entrainment of cumulate fragments during eruption. The

preservation of multiple glass populations and mingling textures suggest brief interactions between melts prior to eruption.

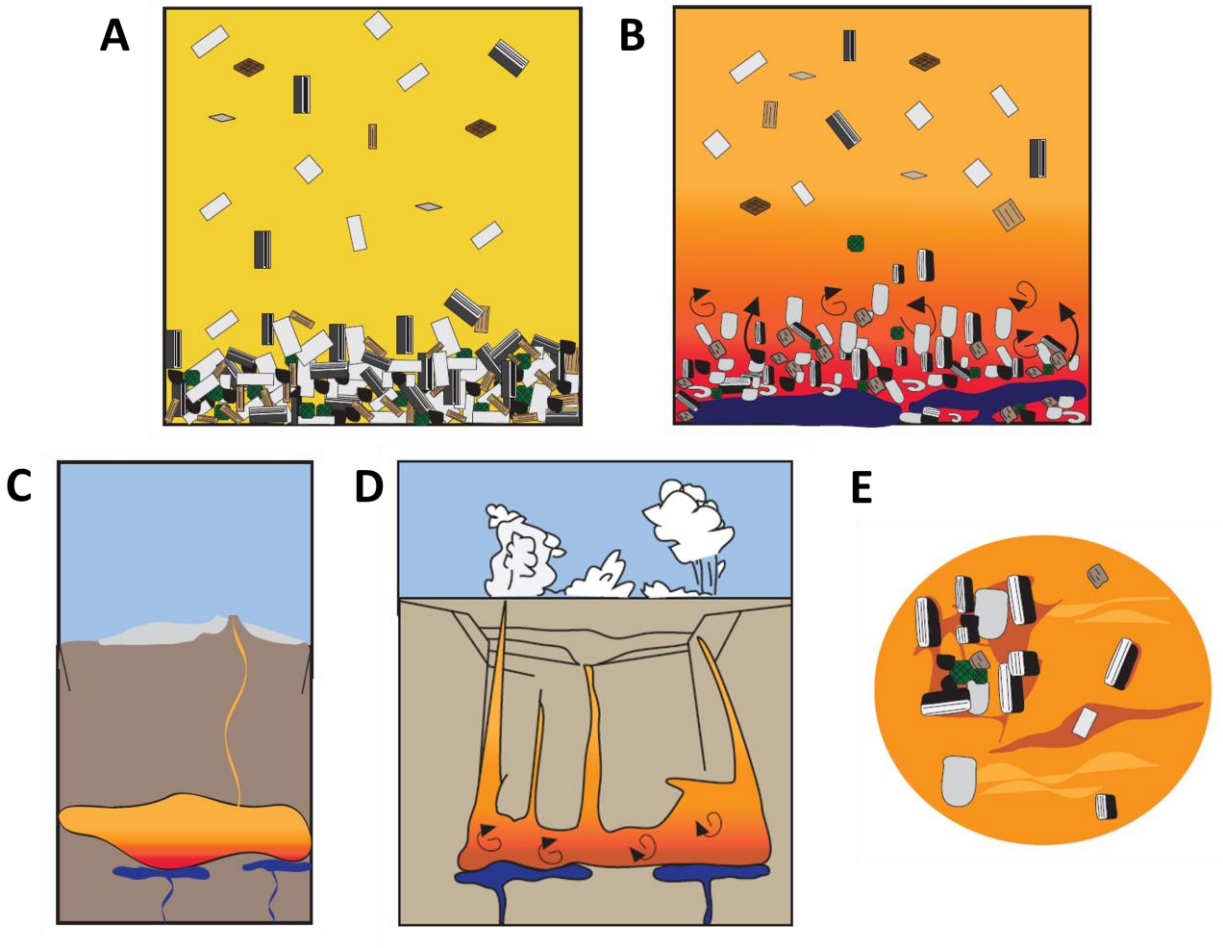

Figure 25. Extremely simplified schematic of processes within the PST magma chamber. (A) Accumulation and melt extraction form the high-silica rhyolite upper lens; original trapped melt is more evolved in composition; (B) Intrusion of replenishing magma leads to rejuvenation of cumulate mush; partial dissolution of the cumulate phases leads to geochemical heterogeneities; (C) Eruption initiates with expulsion of the upper, crystal-pool high-silica rhyolite portion of the PST; (D) Eruption of the cumulate follows the eruption of the HSR PST; (E) Cumulate fragments are entrained during eruption of Tp5; multiple melt populations preserved in fiamme suggest interaction shortly before eruption.

5.1 Comparison to Other Zoned Ignimbrites

The Peach Spring Tuff shares a number of features with many other zoned ignimbrites observed globally (thermal, compositional, and crystal fraction gradients) including the Ammonia Tanks Tuff (Deering et al., 2011), and Carpenter Ridge Tuff (Bachmann et al., 2014). A growing body of evidence indicated by the ignimbrite deposits of these large volumes of relatively crystal-poor magmas suggest that in situ crystal-liquid separation into a lower crystal-rich cumulate zone and upper eruptible lenses at relatively shallow depths (5-10 km in most regions) is common in upper-crustal magma reservoirs (Bachmann et al., 2014). The presence of a late-erupted crystal-rich capping ignimbrite also suggests that recharge and subsequent rejuvenation is important in the remobilization of the chamber cumulate. Sufficient reduction below the rheological lock up is necessary for the eruption of crystal-rich magmas.

APPENDIX

A.

sample	Location	northing	easting	unit name	field notes/other
WSB Fo 1	Warm Springs Butte	3865844	744321	Tp5	zone 1: uppermost PST (last erupted?), densely welded with black fiamme; lithics poor unit
WSB Fo 3	Warm Springs Butte	3865777	744314	Tp5	zone 3: welded, orange/pink matrix with crystal rich fiamme and crystal rich light tan pumice; lithics poor unit
WSB Fo 3b	Warm Springs Butte	3865777	744314	Tp5	
WSB Fo 4	Warm Springs Butte	3865777	744314	Tp5	zone 3: welded, orange/pink matrix with crystal rich fiamme and crystal rich light tan pumice; lithics poor unit
WSB Fo 5	Warm Springs Butte	3865794	744309	Tp5	zone 3: welded, orange/pink matrix with crystal rich fiamme and crystal rich light tan pumice
WSB Fo 6	Warm Springs Butte	3865777	744314	Tp5	zone 3: welded, orange/pink matrix with crystal rich fiamme and crystal rich light tan pumice; lithics poor unit
WSB Fo 7	Warm Springs Butte	3865919	744314	Tp5	Zone 2: vitrophyre zone; lithics poor
WSB Fo 8	Warm Springs Butte	3865824	744327	Tp5	zone 1: uppermost PST (last erupted?), densely welded with black fiamme; lithics poor unit
WSB Fo 9	Warm Springs Butte	3865744	744314	Tp5	zone 3: welded, orange/pink matrix with crystal rich fiamme and crystal rich light tan pumice
WSB Fo 10	Warm Springs Butte	3865744	744314	Tp5	zone 3: welded, orange/pink matrix with crystal rich fiamme and crystal rich light tan pumice; lithics poor unit
WSB Fo 11	Warm Springs Butte	3865680	744497		found at the contact between CCT and PST; first erupted material (FOR COMPARISON TO UPPER)
WSB Fo 12	Warm Springs Butte	3865680	744497	base of section; above CCT	
WSB Fo 20	Warm Springs Butte	3865830	744300	Tp5	crystal-rich, orange pumice; brick orange section at base, above ~hilltop~ section;
WSB Fo 21	Warm Springs Butte	3865830	744300	Tp5	
WSB Fo 22	Warm Springs Butte	3865815	744331	Tp5	whole rock from tiger-stripe, densely welded, fiamme section
WSB Fo 23	Warm Springs Butte	3865815	744331	Tp5	

WSB Fo 24	Warm Springs Butte	3865810	744328	Tp5	whole rock from brick-red, less-welded section (below WSB-Fo 22 & 23), contains a poor crystal-rich orange pumice
WSB Fo 25	Warm Springs Butte	3865841	744244	Tp5	small pumice from *hilltop* zone, below WSZ; closer to contact (within 5 feet)
WSB Fo 26	Warm Springs Butte	3865841	744244	Tp5	whole rock from *hilltop* zone, below WSZ
WSB Fo 27	Warm Springs Butte	3865851	744237	Tp5	small pumice from *hilltop* zone, below WSZ (further from contact ~15 feet down)
WSB Fo 28	Warm Springs Butte	3865884	744233	Tp5	whole rock from WSZ directly above contact
WSB Fo 29	Warm Springs Butte	3865884	744233	Tp4	whole rock from *hilltop* directly below contact
WSB Fo 30	Warm Springs Butte	3865939	744334	>Tp5?	upper fall deposit of PST?
WSB Fo 31	Warm Springs Butte	3865934	744328	Tp5	crystal-rich, blue flame fiamme from tiger stripe section above vitrophyre; close to top of the section
WSB Fo 32	Warm Springs Butte	3865751	744347	Tp5	crystal-rich, blue flame fiamme from tiger stripe section below vitrophyre
WSB Fo 33	Warm Springs Butte	3865680	744120	Tp5	crystal-rich blue flame fiamme; from the lowest faulted section (within pass used to climb up along the faulted escarpment)
WSB Fo 34	Warm Springs Butte	3865751	744347	Tp5	
WSB Fo 35	Warm Springs Butte	3865751	744347	Tp5	
CS Fo 1	Caliche Springs	3867319	753916	>Tp4	
CS Fo 2	Caliche Springs	3867319	753916	>Tp4	
CS Fo 3	Caliche Springs	3867319	753916	>Tp4	found within one exposed wash, lithics present but not abundant; section is unwelded; dual pumice populations
CS Fo 4	Caliche Springs	3867319	753916	>Tp4	
CS Fo 5	Caliche Springs	3867319	753916	>Tp4	
CS Fo 6	Caliche Springs	3867319	753916	>Tp4	
KPP MF 1	Kingman Property	3892673	773092	Tp3	whole pumice sample
KPP MF 2	Kingman Property	3892663	773097	Tp3	
KPP MF 3	Kingman Property	3892673	773092	Tp3	whole pumice sample
KPP MF 4	Kingman Property	3892663	773097	Tp3	pumice intact with PST matrix
KPP MF 5	Kingman Property	3892663	773092	Tp3	whole pumice sample

KPP MF 6	Kingman Property	3892593	773128	Tp3	whole pumice sample
KPP MF 7	Kingman Property	3892663	773097	Tp3	whole pumice sample
KPP MF 8	Kingman Property	3892593	773128	Tp3	whole pumice sample
MF WSW 1a	Warm Springs West	3864205	740073	-	pumice collected from wash (exposed clean surface)
MF WSW 1b	Warm Springs West	3864205	740073	-	
MF WSW 1c	Warm Springs West	3864205	740073	-	
MF WSW 1d	Warm Springs West	3864205	740073	-	
MF WSW 1e	Warm Springs West	3864205	740073	-	
GJ Fo1	Grasshopper Junction	3905378	739594	>Tp4	vitrophyre section; above a crystal-rich section (hard to find fiamme within this section)
GJ Fo 2	Grasshopper Junction	3905153	739609	>Tp4	whole rock containing fiamme ; below vitrophyre section
PSTG 100 C	Times Gulch (Intra-Caldera)	3879833	731317	Intra-Caldera	welded, crystal-rich (~15% modal) red fiamme
KWF Fo 1A	Kingman Wind Farm	3893556	766601	Tp1	pumice; near the base of zone that overlies basal surge; slightly squished pumice, sparse phenocrysts
KWF Fo 1B	Kingman Wind Farm	3893556	766601	Tp1	
KWF Fo 1C	Kingman Wind Farm	3893556	766601	Tp1	
KWF Fo 1D	Kingman Wind Farm	3893556	766601	Tp1	
KWF Fo 1E	Kingman Wind Farm	3893556	766601	Tp1	
KWF Fo X	Kingman Wind Farm	3893556	766601	Tp1	
KWF Fo 2 A	Kingman Wind Farm	3893404	766755	Tp2	pumice; lowest "section" within zone (below the welded, fiamma containing); pumice are relatively unwelded; zone is pumice rich (~15%) ; presumably transition from hilltop into slaughterhouse
KWF Fo 2 B	Kingman Wind Farm	3893404	766755	Tp2	
KWF Fo 2 C	Kingman Wind Farm	3893404	766755	Tp2	
KWF Fo 3A	Kingman Wind Farm	3893404	766755	Tp2	whole rock of welded, fiamme containing; middle "section" within zone (below the vitrophyre)
KWF Fo 3B	Kingman Wind Farm	3893404	766755	Tp2	
KWF Fo 4	Kingman Wind Farm	3893404	766755	Tp2	vitrophyre; upper "section" within zone; SAME AS KWF Fo 6!
KWF Fo 5	Kingman Wind Farm	3893433	766731	Tp4	pumice; HUGE (up to 2-3ft in diameter); unsquashed and highly vesiculated
KWF Fo 6	Kingman Wind Farm	3893560	766591	Tp2	vitrophyre; collected above the holy moses site; sawmill based on relative stratigraphy

KWF Fo 10	Kingman Wind Farm	3894356	767507	Tp3	
KWF Fo 11	Kingman Wind Farm	3894356	767507	Tp3	
KWF Fo 12	Kingman Wind Farm	3894303	767539	Tp3	pumice; light grey, dense
KWF Fo 13	Kingman Wind Farm	3894356	767507	Tp3	
KWF Fo 14	Kingman Wind Farm	3894356	767507	Tp3	
CS Fo 20	Caliche Springs	3867340	754002	Tp4/Tp3	whole rock containing pumice; mildly welded; possibly from top of slaughterhouse/base of hilltop??
CS Fo 21	Caliche Springs	3867409	753844	Tp4/Tp3	grey puffy pumice; unwelded section; possibly from top of slaughterhouse/base of hilltop??
CS Fo 22	Caliche Springs	~3867436~	~753893~	-	FLOAT - vitrophyre found on the climb down; must be a horizon above…
SWA Fo 1A	Warm Springs Wilderness (SWA)	3873031	749241	-	grey pumice; variable sizes (~10cm), puffy, biotite rich (~5%); multiple pumice populations (color based: white, gray, and black); crumbly, caliche infilled (sad) outcrop; relative stratigraphy puts this at the bottom of the section (above basalt and visibly PST above this section)
SWA Fo 1B	Warm Springs Wilderness (SWA)	3873031	749241	-	
SWA Fo 1C	Warm Springs Wilderness (SWA)	3873031	749241	-	
SWA Fo 1D	Warm Springs Wilderness (SWA)	3873031	749241	-	
PM-MF 1	Piute Mountains	3848372	670532	Tp2	vitrophyre
SM-MF 1	Sacramento Mountains	3855296	702916	-	densely welded tuff
TM-MF 1	Thimble Mountain	3882546	746678.2		crystal-rich black blob within welded tuff
TM-MF 2	Thimble Mountain	3882522	746622.2		bulk rock with fiamme (no black crystal-rich blob)
TM-MF 3	Thimble Mountain	3882522	746622.2		crystal-rich black blob within welded tuff
TM-MF 4	Thimble Mountain	3882666	746586.2		mafic lava; present below PST section
TM-MF 5	Thimble Mountain	3882608	746633.2		below PST; possible fall deposit?
TM-MF 6	Thimble Mountain	3881045	747521.2		crystal-rich black blob within welded tuff
TM-MF 7	Thimble Mountain	3881045	747521.2		particularly crystal-rich black blob within welded tuff

TM-MF 8	Thimble Mountain	3881157	747547.2		particularly crystal-rich black blob within welded tuff
GV MF 1	Golden Valley	3898718.9	756806.3	Tp5	crystal-rich, tiger stripe, densely welded
GV MF 2	Golden Valley	3898718.9	756806.3	Tp5	
GV MF 3	Golden Valley	3898718.9	756806.3	Tp5	vitrophyre
TG MF L1	Times Gulch (Intra-Caldera)	3882001	730425.2	Intra-Caldera	intracaldera, above the lower breccia of Charles Ferguson; densely welded with fiamme
TG MF U1	Times Gulch (Intra-Caldera)	3881837	730675.2	Intra-Caldera	
TG MF U2	Times Gulch (Intra-Caldera)	3881837	730675.2	Intra-Caldera	intracaldera, above the upper breccia klippe of Charles Ferguson; densely welded with fiamme
TG MF U3	Times Gulch (Intra-Caldera)	3881837	730675.2	Intra-Caldera	
TG MF U4	Times Gulch (Intra-Caldera)	3881837	730675.2	Intra-Caldera	
TG MF UL1	Times Gulch (Intra-Caldera)	3881815.7	730672.32	Intra-Caldera	intracaldera, section below upper breccia
WSW MF 1	Warm Springs West	3864757	741236	Tp5	
WSW MF 2	Warm Springs West	3864757	741236	Tp5	crystal-rich, tiger stripe, densely welded , above vitrophyre
WSW MF 3	Warm Springs West	3864757	741236	Tp5	
WSW MF 4	Warm Springs West	3864755	741219	Tp5	vitrophyre
WSW MF 5	Warm Springs West	3864757	741236	Tp5	crystal-rich, tiger stripe, densely welded , above vitrophyre

B.

Hand Sample – Matrix Descriptions

Sample	Unit, Zone	Description	Matrix					
			Welding	Color	Phenocryst %	Crystal Sizes	Mineralogy	Lithics
WSB Fo 1	Tp5	black fiamme, crystal rich, ~25% crystals, ~10cm length	heavily welded; dominated by fiamme; tiger striped appearance (glassy)	Off orange/brown; dominated by black fiamme	~20%	1mm >> 2mm	feldspar >> biotite > CPX >	few present; 1.2 cm at the largest
WSB Fo 3	Tp5	crystal rich fiamme ~6cm in length, crystal rich pumice ~10%	lesser degree of welding; more of a chalky appearance	Peachy orange; zero black, glassy fiamme	25% total: ~10-12% for crystal sizes 1mm-1.5mm; with hand lens ups the %	2mm - .5 mm (most between 1-.5mm in size)	feldspars (2mm-.5mm) >> biotite (2mm-1mm) >	sparse, ~1-2%
WSB Fo 7	Tp5	vitrophyre zone	vitrophyre zone	Black matrix	~20% total; (two crystals at 3mm) 2mm-1mm crystals of feldspars account for ~7%;	3mm-.25mm (most within 1mm-.25 mm)	feldspars (3mm-.5mm)>>> biotite (.5mm)>> CPX or orange (not sure if crystals? Or pumice?)	none visible
WSB Fo 8	Tp5	black fiamme, crystal rich, ~15%, halved sample	heavily welded; dominated by fiamme; tiger striped appearance (glassy)	Off orange/brown; dominated by black fiamme	~16-18% total; (most at ~1mm in size accounting for 10% of phenos)	1% 4mm feldspars; most between 2mm-1mm; .5mm biotites and CPX	feldspar>>>biotite > CPX>	~ 2%; 2cm largest; no visible dominating size; range of sizes

WSB Fo 20	Tp5	orange/blue flame pumice/fiamme section	lesser- to moderate degree of welding; more of a chalky appearance	Peachy orange; zero black, glassy fiamme	~15-20% total	largest ~1.5 mm; feldspars range 1.5-.5 mm; biotite ~1.5-mostly .5mm;	feldspar>> biotite	sparse, ~1-2% @ 1.5-2mm in size
WSB Fo 23	Tp5	tiger-striped fiamme section	heavily welded; dominated by fiamme; tiger striped appearance (glassy)	Off orange/brown; dominated by black fiamme	~20-25%	largest ~ 4mm (1%); ranges from 4mm-.5mm; 15% ~1mm	feldspar feldspars ~ 4mm-.5 mm >>>biotite ~1-.5mm >> CPX ~1mm-.5mm > small .5mm orange crystals	not necessarily abundant, but large! 1.5 cm - 2mm
WSB Fo 27	Tp4	pumice	nonwelded	white, ashy (like sugar crystals)	~<10%?	~2mm euhedral feldspar; biotite ~3mm	feldspar>>biotite	small ~ 1mm
WSB Fo 28	Tp5	WSZ sample from directly above contacts with lower *hilltop* zone	poorly-moderately welded	maroon/purple + light brown mix	~10-15%?	2mm feldspar; most ~1mm; biotite ~.5mm	feldspar>>>biotite	1-2%; 7 mm - 1 mm ; more abundant than most of WSZ
WSB Fo 29	Tp4	*Hilltop* sample from directly below contact with upper WSZ	moderately-welded; 'baked' appearance; contains both fiamme AND pumice	grey/light tan mix	~10%	1mm feldspar; 1.5 biotite; most 1mm-.5 mm	feldspar>>biotite> PYX	~3-4%; 2mm-1mm in size
WSB Fo 31	Tp5	WSZ sample within tiger stripe welded section, near top of the section	heavily welded; dominated by fiamme; tiger striped	Off orange/brown; dominated by black fiamme	~20-25%	largest ~ 4mm (1%); ranges from 4mm-.5mm;	feldspars ~ 4mm-.5 mm >>>biotite ~1-.5mm >> CPX ~1mm-.5mm > small .5mm orange crystals	not necessarily abundant, but large!

			appearance (glassy)			15% ~1mm		1.5 cm - 2mm
CS Fo 1	-	crystal rich pumice ~5cm in length, interior light pink crystal content ~5% rimmed by a light tan crystal content ~7%; black glassy pumice ~2cm in length	Poorly to none	~peachy/sk in color	~10 %	~1- 0.5 mml most a 0.5 mm; ~2 % @ 1 mm	feldspar>>biotite	~1 %, small, 2-5 mm
CS Fo 4	-	crystal rich pumice ~7cm in length, matrix of pumice is pink (no rim present) crystal content ~7% with crystal sizes ~1.5mm	Poorly to none					
CS Fo 6	-	black glassy pumice ~3cm in length; crystal rich pumice ~5cm in length with pink matrix	Poorly to none					
KPP MF 2	Tp3	pumice, white matrix, crystal poor ~2%, frothy, crystals ~2mm within vesicles	NA - Whole Pumice	White/Gray				
KPP MF 5	Tp3	pumice, orange/tan matrix	NA - Whole Pumice	Orange				

GJ Fo 1	-	vitrophyre zone	vitrophyre zone	black, glassy	~20% total; 10-13% feldspar; 5% biotite; 3% CPX	3mm-1mm feldspar dominating; 2mm-.5mm biotite mostly around .5 mm size; 1mm - .5mm CPX	feldspar>>>>biotite>CPX	~1% at 2mm-1mm sizes
GJ Fo 2	-	welded zone; stratigraphically below the vitrophyre zone	densely welded, fiamme rich zone	medium brown/tan	20-25% total;		feldspar>>biotite>	
KWF Fo 5	Tp4	Toddler Sized Pumice	NA - Whole Pumice	light grey				
KWF Fo 6	Tp2	vitrophyre zone (bulk tuff + pumice)	partial welding (hasn't lost all pore space)	black to brown	~15 % total	6mm-.5 mm feldspars;	feldspar	1-2% with 7mm sizes
KWF Fo 4	Tp2							
KWF Fo 3B	Tp2	bulk tuff + pumice/fiamme	partial welding	brown with black fiamme	~10-12%	4mm-m5 mm feldspars; mafics .5 - 1 mm	feldspars>>>mafic	1-2% with up to 6 mm sizes
KWF Fo 2A	Tp2	fibrous pumice ; very glassy with crystalline/spongy texture	NA - Whole Pumice	light tan				
KWF Fo 1E	Tp1	fibrous pumice	NA - Whole Pumice	white - pinkish				
SWA Fo 1A	-	Fibrous/dense pumice	NA – Whole Pumice	Dark grey				

Hand Sample – Pumice/Fiamme Descriptions

Sample		Fiamme/Pumice		
	Size of Fiamme/Pumice (LxH)	**Phenocryst %**	**Crystal Sizes**	**Mineralogy**
WSB Fo 1	Fiamme: (8cm X 1.2cm) < (5cm x 1.2) <<<< main size ~ (2cm x 2mm)	in the larger fiamme: ~30-35%	feldspar: 3mm - 1mm; CPX: .5mm	feldspar>>>> CPX
WSB Fo 3	[Fiamme (blue glassy): 5.8cm x 1.6 cm; 6.5 cm x 2cm] [Orange/tan pumice: 3.5 cm x 4cm; 1cm x .5cm; most sizes ~ 2mm- 1mm]	Fiamme: ~35% ; Pumice: 3-5%	Feldspar: 2mm - 1mm; biotite: 3mm - 1mm	fiamme: feldspar >> biotite >> CPX, small orange crystal… ; pumice: feldspar > biotite
WSB Fo 7				
WSB Fo 8	black glassy crystal-rich fiamme: (8cmx 3cm) << (4cm x 1cm)	in the crystal-rich: ~15-20%	feldspar: 3mm-1mm; biotite: .5mm; CPX: .5mm	feldspar>>> biotite> CPX
WSB Fo 20	large orange, crystal-rich with blue flame center: ~6cm in diameter; multiple small ~7mm x 2mm orange pumice within matrix;	~>25% in large orange pumice; ~5% biotite	feldspar: 4mm - .5mm ; biotite 2mm-1 mm; found 1 CPX at .25 mm	feldspar>>biotite>>CPX

WSB Fo 23	black glassy crystal-rich fiamme ~8 cm (was cut out for ts); dominated by small (2 cm x 6 mm) - (5 mm x .5 mm) fiamme;	in the 2 cm fiamme: ~15-18% with 10% feldspar	feldspar ~1mm-.5mm; biotite ~.5 mm; CPX ~.5mm	feldspar>>>>biotite>CPX
WSB Fo 27	white puffy pumice! Grey bands within with a preferred orientation?	~2-3% total	feldspar at 4% modally, sizes ~3mm-1mm; 1% biotite ~.5mm	feldspar>>biotite
WSB Fo 28	small, 1 cm x 3 mm sized black fiamme things???			
WSB Fo 29	red, significantly more crystal-rich fiamme; largest at 3.5 cm x .5 cm; few small (mildly crystalline) pumice and minor puffy pumice	~15% crystals (hard to really tell because fiamme are altered)	feldspar at 4mm-1mm; biotite ~.5mm	feldspar>>>biotite>small red crystal
WSB Fo 31	small, black glassy crystal-rich fiamme (~20 mm)was cut out for ts);	in the 2 cm fiamme: ~15-18% with 10% feldspar	feldspar ~1mm-.5mm; biotite ~.5 mm; CPX ~.5mm	feldspar>>>>biotite>CPX
CS Fo 1	~4 cm - 0.5 cm; most are ~ 2 cm	orange pumice: ~3% ; white pumice : ~0-5 %	~0-5 %	feldspar>>biotite
CS Fo 4				
CS Fo 6				

KPP MF 2		2-3% phenocrysts + voids ~3%	feldspar: 4mm-1mm (most around 2mm; biotite: 2mm-.5mm; cpx: .25mm	feldspar >>biotite (.5% total modal) > CPX(one spot)
KPP MF 5		30-35% crystals in voids ; matrix has ~2%, but the voids make up ~30% of total pumice	feldspar: 4mm-.5 mm (most around 1mm in size); biotite: 1mm-.5mm	feldspar (20-25% modal) >> biotite (~5%)
GJ Fo 1				
KWF Fo 5		~ 7-10%	feldspar: 5 - .5 mm (most around 2mm) ; biotite ~.5 mm-1mm	feldspar (5-7%) (sanidine>>plagioclase) >> biotite
KWF Fo 6	2 cm length x 2mm height;			
KWF Fo 4				
KWF Fo 3B	2 cm length x 2mm height;			
KWF Fo 2A		~ 5 %	feldspars: 5mm! Most around 1-2 mm in size; mafic mineral .5 - 1mm	feldspar (5%) >>> mafic mineral ~1%
KWF Fo 1E		~1-2%	feldspars:1mm max; mafic mineral .5 - .25 mm	feldspar (1.5%) >>> biotite (.5%)
SWA Fo 1A		~10-12%	Feldspars: ~1-0.5 mm; biotite: 0.5 mm	Feldspar (7%)>>biotite(~1%)

C.

Glass

RGM-1	Na2O	MgO	Al2O3	SiO2	P2O5	K2O	CaO	TiO2	FeO	Total
Standard	**4.11**	**0.28**	**13.85**	**74.20**	**0**	**4.35**	**1.16**	**0.27**	**1.74**	**100.00**
1	4.09	0.25	13.81	74.14	0	4.42	1.27	0.4	1.62	100
2	4.13	0.29	14.01	74.06	0	4.34	1.24	0.3	1.63	100
3	4.24	0.28	13.89	73.9	0	4.39	1.14	0.34	1.84	100
4	4.12	0.3	14.03	74.04	0	4.25	1.15	0.2	1.92	100
5	4.15	0.27	13.92	74.32	0	4.44	1.15	0	1.75	100
6	4.08	0.3	13.8	74.03	0	4.27	1.17	0.33	2.03	100
7	4.12	0.3	13.82	74.03	0	4.27	1.2	0.38	1.89	100
8	4.18	0.26	13.94	74.06	0	4.23	1.28	0.35	1.69	100
9	4.01	0.3	13.8	74.5	0	4.36	1.11	0.22	1.69	100
10	4.06	0.28	13.75	74.32	0	4.2	1.27	0.37	1.75	100

Mineral Standards

Albite	Na2O	MgO	Al2O3	SiO2	K2O	CaO	TiO2	FeO	Sum
SPI Reported Value	11.59		19.54	68.52	0.22	0.13			100
SEM-EDS ANALYSIS									
1	11.95	0.01	20.52	66.78	0.14	0.49	0	0.1	100
2	12.01	0	20.24	67.15	0.15	0.42	0.03	0	100
3	12.01	0	20.33	66.93	0.12	0.53	0	0.07	100
4	12.09	0.02	20.15	67.25	0.16	0.27	0	0.06	100

Orthoclase	Na2O	MgO	Al2O3	SiO2	K2O	CaO	TiO2	FeO	Total
SPI Reported Value	0.47		16.88	64.67	15.96			1.99	100
SEM-EDS ANALYSIS									
1	0.94	0.01	16.75	64.21	15.51	0.08	0	1.63	100
2	0.94	0.02	16.96	64.71	15.39	0.04	0.1	1.84	100
3	0.93	0.02	16.85	64.86	15.53	0.06	0.01	1.74	100
4	0.99	0	17.07	64.69	15.48	0.02	0	1.75	100

Plagioclase An-65	Na2O	MgO	Al2O3	SiO2	K2O	CaO	TiO2	FeO	SrO	BaO	Total
SPI Reported Value	4.35	0.13	28.53	54.21	0.41	11.8	0.07	0.37	0.08	0.01	100
SEM-EDS ANALYSIS											
1	4.44	0.12	29.81	51.15	0.36	11.98	0	0.42		1.72	100
2	4.5	0.07	29.79	51.23	0.44	12.03	0.13	0.45		1.36	100
3	4.56	0.02	30.11	52.15	0.39	12.11	0.15	0.5			100
4	4.56	0.09	30.05	52.33	0.33	12.18	0.13	0.33			100

Biotite	H2O	Na2O	MgO	Al2O3	SiO2	K2O	CaO	TiO2	MnO	FeO	Sum
SPI Reported Value	4.11		19.52	15.13	38.72	9.91	0.01	1.77	0.04	10.72	100
Anhydrous		0	20.37	15.79	40.41	10.34	0.01	1.85	0.04	11.19	100
SEM-EDS ANALYSIS											
1		0.08	20.26	16.49	39.49	11.03	0.03	1.59		11.04	100
2		0.07	20.25	16.45	39.31	10.92	0.07	1.66	0.25	11.04	100
3		0.07	20.25	16.27	39.61	10.86	0.18	1.61		11.16	100
4		0.12	21.1	16.49	39.86	10.97	0.05	1.65		9.76	100

Diopside	Na2O	MgO	Al2O3	SiO2	K2O	CaO	TiO2	FeO	MnO	Total
SPI Reported Value		18.62	0.09	55.37		25.73	0.08	0.05	0.05	100
SEM-EDS ANALYSIS										
1	0	19.29	0.02	54.6	0	25.83	0.06	0.19		100
2	0	19.18	0	54.83	0	25.96	0.01	0.02		100
3	0.02	19.21	0.08	54.63	0.04	25.81	0.06	0.15		100
4	0.04	19.1	0.05	54.61	0.05	26.03	0.12	0		100

Magnetite	Na2O	MgO	Al2O3	SiO2	K2O	CaO	TiO2	V2O5	FeO	Cr2O3	Total
SPI Reported Value									99.79	0.2	100
SEM-EDS ANALYSIS											
1	0.07	0.14	0.18	0.06	0.05	0	0.27	0.37	98.85		100
2	0.13	0.09	0.21	0.07	0.04	0	0.1	0.4	98.96		100
3	0.02	0.22	0.12	0.15	0.03	0	0.04	0.46	98.96		100
4	0	0.12	0.18	0.13	0.01	0.01	0.1	0.45	99		100

Quartz	Na2O	MgO	Al2O3	SiO2	K2O	CaO	TiO2	FeO	Total
SPI Reported Value				100					100
SEM-EDS ANALYSIS									
1	0	0	0.04	99.85	0	0	0.02	0.09	100
2	0	0	0	99.88	0.04	0	0	0.08	100
3	0	0.06	0	99.89	0	0	0.04	0.01	100
4	0	0	0	99.97	0.02	0	0	0	100

Apatite	F	Na2O	MgO	Al2O3	SiO2	P2O5	SO3	K2O	CaO	TiO2	FeO	Sum
SPI Reported Value	3.74			0.09	0.47	41.39	0.49		53.97	0.05		100
SEM-EDS ANALYSIS												
1	1.18	0.31	0.04	0.03	0.14	39.41	0.36	0.03	54.69	0	0.05	95.06
2	1.12	0.3	0.02	0	0.18	39.4	0.46	0.02	54.83	0	0.1	95.31
3	1.09	0.45	0	0.06	0.1	39.42	0.58	0.07	54.7	0	0.07	95.43
4	1.17	0.19	0.06	0.02	0.12	39.29		0.03	55.36	0	0.04	95.12

	RGM-1	GeoRem_RGM-1	NIST-612	GeoRem_NIST612	NIST-610	GeoRem_NIST610
Li	258.10	60.7	40.88	40.2	485.14	468
B	31.68	27.4	37.60	34.3	356.86	350
Na	27876.86		95850.35		95454.46	
Mg	1586.17		60.38	68	465.94	432
Al	73149.47		10490.73		10014.00	
Si	347013.96		336999.97		328329.13	
P	172.23		48.06	46.6	343.05	413
K	36985.63		61.19	62.3	487.11	464
Ca	8724.40		85189.60		81928.34	
Sc	12.79	4.74	45.30	39.9	441.53	455
Ti	1452.56		42.88	44	434.62	452
V	11.13	11.76	37.64	38.8	442.59	450
Cr	2.83	4.45	34.87	36.4	405.90	408
Mn	260.05		36.58	38.7	433.81	444
Fe	105.99		38.39	51	457.64	458
Co	1.82	2.043	34.05	35.5	405.59	410
Ni	6.42	3.41	37.89	38.8	444.55	458.7
Cu	9.83	11.09	37.62	37.8	430.81	441
Zn	35.18	33.2	37.12	39.1	456.84	460
Ga	25.71	16.06	36.46	36.9	438.49	433
Ge	1.27	1.26	37.08	36.1	426.94	447
Se	2.48	0.006	14.14	16.3	109.27	138
Rb	150.01	149.5	31.70	31.4	432.22	425.7
Sr	101.62	104.8	76.08	78.4	498.32	515.5
Y	21.17	23.48	38.90	38.3	450.53	462
Zr	209.56	227.9	38.32	37.9	440.39	448
Nb	7.66	9.13	34.59	38.9	419.84	465
Cs	9.38	10.1	40.40	42.7	361.37	366
Ba	768.33	826.8	36.48	39.3	424.66	452
La	23.80	22.94	37.84	36	457.92	440
Ce	44.50	46.01	37.82	38.4	448.49	453
Pr	4.79	5.285	36.26	37.9	430.49	448
Nd	18.97	19.19	35.93	35.5	431.28	430
Sm	3.88	3.968	37.71	37.7	451.09	453
Eu	0.60	0.622	37.07	35.6	461.57	447
Gd	3.48	3.682	36.27	37.3	420.58	449
Tb	0.58	0.597	38.20	37.6	443.19	437
Dy	3.44	3.667	35.46	35.5	426.88	437
Ho	0.74	0.763	38.71	38.3	449.99	449
Er	2.15	2.293	36.54	38	426.51	455
Tm	0.32	0.362	36.36	36.8	420.61	435
Yb	2.58	2.468	40.17	39.2	462.40	450
Lu	0.36	0.397	36.44	37	435.29	439
Hf	5.64	6.032	36.57	36.7	418.17	435
Ta	0.72	0.95	31.62	37.6	377.13	446
Tl	0.63	0.99	14.26	14.9	61.28	59.6
Pb	23.46	23.37	36.55	38.57	413.81	426

Th	14.10	14.56	38.15	37.79	451.40	457.2
U	5.57	5.58	36.69	37.38	458.07	461.5

D.

Bulk whole-rock major and trace elemental chemistry

Sample	WSB Fo 1	WSB Fo 3	WSB Fo 7	WSB Fo 8	WSB Fo 20	WSB Fo 23	WSB Fo 27	WSB Fo 28	WSB Fo 29	KPP MF 2
Whole-Rock Composition Same Description	trachyte fiamme	trachyte fiamme	trachyte vitrophyre	trachyte fiamme	trachyte fiamme	trachyte fiamme	low-Zr rhyolite pumice	trachyte bulk tuff	trachyte bulk tuff	low-Zr rhyolite pumice
Major Oxides, wt%, normalized to 100%										
SiO2	66.76	66.60	67.07	66.75	66.03	67.96	75.61	67.75	67.66	73.82
Al2O3	16.82	16.27	16.62	16.58	15.63	16.26	12.77	16.02	15.52	13.28
Fe2O3(T)	2.87	3.00	2.67	3.09	2.76	2.64	1.49	2.52	2.51	1.44
MnO	0.08	0.08	0.07	0.08	0.08	0.07	0.03	0.07	0.07	0.07
MgO	0.65	1.18	0.55	0.69	1.53	0.54	0.15	0.79	0.75	0.79
CaO	1.76	2.35	1.67	1.74	3.76	1.44	0.56	2.19	2.26	1.32
Na2O	3.66	3.12	3.85	3.81	2.93	3.58	3.05	3.94	3.74	2.66
K2O	6.75	6.77	6.85	6.63	6.68	6.97	6.13	6.17	6.91	6.37
TiO2	0.51	0.51	0.50	0.51	0.48	0.46	0.21	0.44	0.44	0.22
P2O5	0.15	0.13	0.14	0.14	0.13	0.08	0.00	0.11	0.13	0.03
Trace elements, ppm										
Au		4		4						
Ag	1	1	0.9	0.6	0.8	0.9				
As	3	3	4	4	3	3	2	3	2	7
Ba	1421	993	1244	1043	1005	1018	32	944	835	167
Be	3	2	3	3	2	3	3	3	3	5
Bi	0.1	0.1	0.1	0.2	0.1	0.2				0.3
Br	1.6				4.4					3.9
Co										6.6
Cr	10.8	62.8	21.4	12	54.7	16	67.9	20	50.9	3.4
Cs	1.6	1.8	1.3	1.6	1.5	1.6	0.3	0.9	0.7	3.5
Cu	4	12	4	4	10	3	5	6	7	9
Ga	21	20	21	21	19	21	20	22	21	20
Ge	1.6	1.6	1.6	1.7	1.4	1.7	2.1	1.7	1.6	1.6
Hf	11.7	12.8	13	11.3	10.3	11	4.7	9.6	9.6	6.9
Hg	< 1	< 1	< 1	< 1	< 1	< 1	< 1	< 1	< 1	< 1
In	< 0.1	< 0.1	< 0.1	< 0.1	< 0.1	< 0.1	< 0.1	< 0.1	< 0.1	< 0.1
Ir	< 1	< 1	< 1	< 1	< 1	< 1	< 1	< 1	< 1	< 1
Mo	3	4	3	3	4	3	3	< 2	3	5
Nb	15.1	15.4	16.7	14.7	13	17	16.2	17.6	17.5	23.6
Ni	2	6	4	4	6	3	5	6	7	4
Pb	27	24	26	72	17	27	21	27	24	29
Rb	134	116	128	130	119	147	151	103	147	224
S	0.011	0.034	0.015	0.024	0.101	0.005	0.003	0.007	0.017	0.026
Sb	0.5	0.6	0.6	0.3	0.5	0.6	0.2	0.4	0.2	0.9
Sc	7.52	7.94	7.52	8.18	7.53	6.91	3.25	6.62	6.45	3.38

Sn	2	2	2	2	2	2	1	2	1	3
Sr	289	223	242	229	240	196	14	239	185	41
Ta	1.61	1.16	1.34	1.34	1.21	1.46	2.22	1.59	1.53	2.25
Th	20.1	18.7	20.4	20.4	19	21.2	25.4	22.3	21.7	32.3
U	2.92	2.37	2.79	2.83	2.55	3.05	3.41	3.34	3.61	5.95
V	23	20	22	21	21	18	< 5	17	17	7
Y	34	32	33	35	30	35	29	35	35	32
Zn	61	53	61	67	50	55	26	55	61	61
Zr	579	504	484	546	479	508	174	422	429	225
La	159	168	173	170	172	159	61	141	136	64.1
Ce	318	335	336	334	340	310	118	274	269	131
Pr	34.9	36	36.9	35.9	36.1	34.2	12.6	30.7	29.6	13.4
Nd	120	123	125	124	124	117	41.5	106	101	43
Sm	17.9	18	18.6	18.7	18.1	18	7.25	16.6	16.1	7.8
Eu	3.22	2.96	3.29	3.21	3.05	2.92	0.642	2.61	2.37	0.637
Gd	11.4	11.3	11.5	11.5	10.9	11.4	6.05	10.9	10.4	6.28
Tb	1.41	1.35	1.46	1.4	1.36	1.45	0.89	1.42	1.42	0.99
Dy	7.3	6.76	7.18	7.22	6.89	7.49	5.39	7.66	7.43	5.63
Ho	1.29	1.19	1.25	1.32	1.19	1.34	1.05	1.43	1.33	1.12
Er	3.7	3.5	3.53	3.68	3.41	3.75	3.06	3.83	3.71	3.49
Tl	0.62	0.63	0.54	0.77	0.92	0.89	0.25	0.58	0.45	1.36
Tm	0.493	0.484	0.504	0.52	0.469	0.521	0.464	0.554	0.514	0.521
Yb	3.19	2.89	3.16	3.07	3.07	3.31	2.87	3.45	3.13	3.4
Lu	0.459	0.443	0.456	0.458	0.455	0.514	0.432	0.49	0.482	0.513

Bulk whole-rock major and trace elemental chemistry cont.

Sample	KPP MF 5	GJ Fo 1	GJ Fo 2	SWA Fo 1A	KWF Fo 5	KWF Fo 10	KWF Fo 4	KWF Fo 3B	KWF Fo 2A	KWF Fo 1E
Whole-Rock Composition	trachyte	trachyte	trachyte	trachyte	low-Zr rhyolite	low-Zr rhyolite	low-Zr rhyolite	low-Zr rhyolite	low-Zr rhyolite	low-Zr rhyolite
Same Description	pumice	vitrophyre	bulk tuff	pumice	pumice	pumice	vitrophyre	bulk tuff	pumice	pumice
Major Oxides, wt%, normalized to 100%										
SiO2	67.90	68.96	70.09	68.34	71.56	73.91	73.87	73.92	75.20	74.29
Al2O3	16.32	16.03	14.95	17.62	15.01	13.14	13.55	13.53	13.06	14.25
Fe2O3(T)	2.64	2.69	2.69	3.10	1.49	1.78	1.66	1.64	1.38	1.48
MnO	0.07	0.07	0.05	0.06	0.06	0.07	0.07	0.06	0.07	0.07
MgO	0.60	0.63	0.44	1.99	0.17	0.27	0.29	0.75	0.24	0.47
CaO	1.18	1.54	1.12	2.01	0.49	1.47	0.86	1.03	0.60	0.68
Na2O	3.42	4.58	3.92	2.48	4.46	3.73	3.54	3.06	2.93	2.77
K2O	7.28	4.91	6.18	3.81	6.51	5.29	5.88	5.74	6.29	5.73
TiO2	0.52	0.49	0.45	0.54	0.23	0.27	0.28	0.27	0.22	0.25
P2O5	0.07	0.11	0.10	0.06		0.05				
Trace elements, ppm										
As	2	4	11	2	5	5	7	6	7	6
Ba	424	952	857	1182	61	130	117	109	51	42
Be	2	3	3	3	5	5	5	4	5	5
Bi	0.3	0.1	0.1	0.2						
Cr	8.3	39	17.8	33.7	8.9	12.2	18.1	12.7	5.6	5.9
Cs	3.5	4	1.3	1.8	2.1	1.9	2.9	2.7	3	3.2
Cu	6	5	4	10	7	7	3	4	8	4
Ga	22	22	22	22	23	19	20	21	20	21
Ge	1.8	1.7	1.6	1.8	1.8	1.7	1.6	1.7	1.7	1.6
Hf	14.5	12.1	11.4	13.7	6.9	6	7.3	6.9	6.7	7.3
Nb	19.5	19.9	21.3	21.6	27.6	25.7	24.9	24.4	28.7	27.1
Ni	2	4	7	8	4	4	3	5	2	2
Pb	27	26	26	20	32	32	28	36	30	30
Rb	123	317	147	132	256	215	206	195	216	198
S	0.014	0.006	0.012	0.011	0.004	0.016	0.017	0.053	0.005	0.003
Sb	0.3	0.4	0.5	0.5	0.5	0.6	0.7	0.7	0.6	0.7
Sc	8.86	7.59	6.91	9.09	4	4.37	4.42	4.39	3.42	3.8
Sn	2	2	2	4	4	1	3	7	4	2
Sr	93	198	164	349	16	35	52	54	10	14
Ta	1.38	1.44	1.68	1.41	2.28	2.12	2.05	2.06	2.15	2.26
Th	21.8	20.6	22.5	21.8	34.2	29.8	30.4	31.5	33.2	32.2
U	2.35	2.92	3.56	2.88	5.41	4.53	5.79	5.53	6.5	5.5

V	22	19	25	26	8	10	12	14	7	8
Y	38	33	38	34	33	26	36	36	32	34
Zn	60	57	62	57	50	50	56	68	49	55
Zr	629	497	454	596	207	206	250	231	205	239
La	219	167	137	159	78.1	68.8	78.3	79.1	65.9	69.8
Ce	432	323	267	325	142	132	151	152	129	139
Pr	46.9	34.9	30.5	34.5	14.6	13.6	15.8	16.3	12.9	14.6
Nd	161	119	107	118	47	43.2	53.2	53.1	41.2	49.2
Sm	23.6	17.6	17.9	17.5	8.07	7.7	9.58	9.55	7.59	8.77
Eu	3.44	3.08	2.53	3.06	0.726	0.788	0.887	0.819	0.572	0.766
Gd	14	11	11.8	10.9	6.3	5.81	7.53	7.43	6.11	6.95
Tb	1.74	1.39	1.65	1.44	0.92	0.87	1.14	1.07	0.95	1.09
Dy	8.54	7.09	8.62	7.2	5.64	5.1	6.79	6.57	5.53	6.25
Ho	1.54	1.27	1.57	1.28	1.09	0.97	1.25	1.26	1.09	1.19
Er	4.1	3.64	4.27	3.63	3.32	2.97	3.81	3.61	3.34	3.52
Tl	1	2.09	1.02	1.45	0.46	0.6	0.92	0.86	0.78	0.76
Tm	0.572	0.512	0.584	0.509	0.485	0.434	0.526	0.518	0.487	0.512
Yb	3.59	3.14	3.6	3.28	3.35	3.02	3.55	3.59	3.37	3.32
Lu	0.559	0.469	0.523	0.498	0.528	0.454	0.549	0.543	0.523	0.518

E.

Glass Trace Element Geochemistry

Sample	WSB Fo 1	WSB Fo 1 A	WSB Fo 1 B	WSB Fo 3	WSB Fo 3b	WSB Fo 8	WSB Fo 20	WSB Fo 23
Glass Composition	high-Zi rhyolite	trachyte	high-Zi rhyolite	high-Zi rhyolite	high-Zi rhyolite	high-Zi rhyolite	high-Zi rhyolite	high-Zi rhyolite
Same Description	fiamme; mount	fiamme	fiamme	fiamme; mount	fiamme	fiamme	fiamme	fiamme
				Trace element averages, ppm				
Li	10.78	13.71	13.03	4.06	4.48	9.89	7.41	11.05
B	19.01	22.69	30.32	17.26	28.37	18.55	126.75	25.35
Na	23664	25744	24652	24608	23761	25674	21030	25062
Mg	2336	3658	2193	1894	2099	1919	2527	1314
Al	92721	87646	82653	102520	80712	99907	82026	79881
Si	329545	316410	339548	334874	335341	335018	335403	335060
P	286	862	206	192	246	174	234	139
K	55365	67403	67928	55403	62586	55842	62918	63650
Ca	9212	11168	7265	7927	7627	7770	7786	5909
Sc	19.58	14.97	13.30	17.72	13.51	19.01	12.72	14.10
Ti	2438	2677	1948	2321	2117	2471	2031	1933
V	13.12	17.80	9.94	8.27	8.86	9.09	8.90	6.28
Cr	0.26	4.10		0.31		0.29	1.77	
Mn	559	664	483	561	506	570	448	540
Fe	118	136	87	105	83	98	91	89
Co	1.13			0.62	0.59	0.71	0.66	0.52
Ni	0.44	6.79	9.09	0.33	0.36	0.47	1.18	0.38
Cu	2.06	9.70	7.30	1.28	3.50	0.96	8.85	0.88
Zn	65.32	103.75	59.60	57.28	55.61	55.09	56.53	57.73
Ga	82.14	49.89	27.72	47.18	25.92	53.87	25.71	19.86
Ge	2.05	1.48	1.58	2.19	1.55	2.23	1.55	1.47
Rb	160	152	156	160	146	174	152	193
Sr	180.21	218.07	140.06	79.70	88.87	75.91	97.62	21.20
Y	32.28	33.02	31.18	40.03	30.72	38.17	31.02	35.31
Zr	570	721	441	520	461	556	448	375
Nb	28	20	26	29	24	29	24	25
Cs	1.69	1.55	1.71	1.75	1.68	1.76	1.74	1.50
Ba	965	2292	640	427	551	531	546	110
La	147.53	178.01	132.41	173.40	159.20	191.72	148.70	131.63
Ce	266.33	322.02	246.50	303.30	301.62	336.67	276.34	257.97
Pr	29.83	35.29	25.36	35.23	30.99	37.84	29.10	27.22
Nd	101.15	132.46	91.35	123.41	109.72	129.75	104.40	98.75
Sm	14.31	18.21	13.36	18.22	15.36	18.18	14.78	15.94
Eu	2.86	3.98	2.32	2.69	2.78	2.89	2.35	2.03
Gd	13.22	11.45	8.67	14.30	9.93	14.46	9.74	9.93
Tb	1.36	1.37	1.13	1.70	1.24	1.66	1.20	1.42
Dy	6.32	6.97	6.05	8.14	6.39	7.78	6.23	7.21
Ho	1.28	1.32	1.17	1.64	1.19	1.58	1.18	1.37
Er	3.23	3.31	3.13	4.06	3.08	3.90	3.12	3.52
Tm	0.49	0.46	0.46	0.61	0.44	0.58	0.44	0.48
Yb	3.20	3.27	3.21	3.90	3.06	3.79	3.03	3.33
Lu	0.50	0.48	0.46	0.61	0.45	0.59	0.45	0.48

Hf	12.70	14.95	10.54	12.52	10.81	13.02	10.66	9.50
Ta	1.37	0.90	1.26	1.48	1.12	1.45	1.19	1.20
Tl	1.02	0.94	0.83	0.73	0.59	1.01	0.78	0.91
Pb 204	32.96	38.82	31.27	32.01	30.75	34.28	23.96	31.74
Tl	1.03	0.91	0.83	0.75	0.55	1.02	0.82	0.90
Pb 206	35.89	41.26	33.63	35.00	31.83	37.19	25.27	34.55
Pb 207	33.92	38.67	31.98	32.80	29.43	34.98	23.69	32.28
Pb 208	36.49	40.45	33.33	35.06	31.16	37.50	24.70	34.13
Th	22.65	16.33	22.37	25.60	20.94	26.04	21.26	19.74
U	3.66	2.33	3.60	3.49	3.05	3.52	3.09	2.85

Glass Trace Element Geochemistry cont.

Sample	WSB Fo 31 A	WSB Fo 31 B	WSB Fo 31 C	MLPT 5D	PST SWA 01A	KPP MF 5	GJ Fo 1	KWF Fo 3B	KWF Fo 2A	KWF Fo 1E
Glass Composition	trachyte	high-Zi rhyolite	high-Zi rhyolite	high-Zi rhyolite	trachyte	high-Zi rhyolite	high-Zi rhyolite	low-Zr rhyolite	low-Zr rhyolite	low-Zr rhyolite
Same Description	fiamme	fiamme	fiamme	pumice	pumice	pumice	fiamme in vitrophyre	fiamme in bulk tuff	pumice; mount	pumice; mount
					Trace element averages, ppm					
Li	18.40	13.29	10.03	19.95	6.78	34.49	15.02	27.00	23.27	16.24
B	340.96	97.10	128.3	16.31	259.92	17.33	35.77	47.64	35.75	35.63
Na	27677	26226	23080	22525	31262	25284	34432	22715	22834	22984
Mg	4562	2775	2083	4256	5282	3488	2097	421	446	598
Al	87912	83638	78292	93569	92475	90318	83617	63647	65465	67457
Si	313792	333284	347494	331415	319752	332630	340062	358339	358760	358012
P	1333	320	211	362	508	303	220	29	38	34
K	66213	65980	62948	53399	48740	56521	44315	55763	49771	51194
Ca	15592	8532	6095	7028	11576	6159	7212	3050	3476	3490
Sc	14.49	13.45	12.01	9.50	10.87	9.08	14.02	9.87	10.57	11.39
Ti	2692	2133	1580	2480	3216	2345	2022	731	722	746
V	21.55	12.78	7.73	7.36	16.53	7.50	9.36	1.10	1.08	1.30
Cr	23.06	8.41	10.71	5.59	1.49	3.15	6.06	1.61	5.23	1.90
Mn	587	589	451	585	562	487	540	481	512	500
Fe	144	102	82	153	230	153	87	44	42	45
Co	29.69	11.59		1.42	1.64	101.0	13.60	0.21	1.63	0.38
Ni	12.08		9.31	3.53	0.90	6.27	7.23	0.18	0.92	0.39
Cu	30.10	10.84	6.53	10.41	29.00	28.19	7.16	1.53	2.78	1.70
Zn	93.57	69.81	52.24	31.34	61.57	30.00	63.47	55.35	49.86	37.36
Ga	47.77	33.30	28.12	23.55	42.69	20.54	25.92	17.82	17.89	18.75
Ge	1.56	1.59	1.66	1.54	1.28	1.45	1.79	1.54	1.51	1.57
Rb	157	164	174	221	143	145	447	239	229	235
Sr	285.23	166.9	117.8	35.16	212.79	24.44	72.72	2.39	2.09	3.51
Y	32.41	30.31	26.91	41.02	28.30	39.17	32.08	18.67	19.45	20.52
Zr	754	538	356	357	623	353	455	116	123	127
Nb	19	24	29	30	22	30	25	33	33	34
Cs	1.49	1.73	2.32	1.69	1.15	1.62	3.76	3.41	3.27	3.41
Ba	2161	1093	680	138	1617	79	498	3	4	7
La	164.79	146.8	98.25	143.5	152.50	126.2	148.39	42.48	44.83	46.89
Ce	286.43	271.4	178.8	288.6	304.27	253.6	271.75	77.11	78.02	80.57
Pr	32.12	27.70	18.08	31.87	31.53	28.33	28.65	6.51	6.64	6.93
Nd	119.40	103.1	62.93	112.1	109.88	99.84	104.04	18.35	18.76	20.07
Sm	16.47	15.10	9.33	17.48	14.83	16.15	15.13	2.74	2.86	3.01
Eu	4.18	2.78	1.60	2.28	3.31	1.79	2.46	0.17	0.19	0.20
Gd	10.47	8.89	6.15	12.34	9.85	11.77	9.78	2.31	2.29	2.42

Tb	1.27	1.12	0.83	1.54	1.09	1.48	1.27	0.37	0.39	0.41
Dy	6.57	6.17	4.75	8.82	6.00	8.44	6.73	2.40	2.51	2.65
Ho	1.23	1.14	0.96	1.59	1.09	1.50	1.24	0.56	0.59	0.60
Er	3.11	2.97	2.54	4.26	2.89	3.99	3.31	1.76	1.84	1.91
Tm	0.44	0.43	0.43	0.59	0.41	0.56	0.46	0.29	0.30	0.32
Yb	3.09	2.95	2.80	3.73	2.81	3.70	3.22	2.35	2.42	2.46
Lu	0.45	0.48	0.43	0.54	0.41	0.53	0.47	0.36	0.36	0.37
Hf	15.42	12.47	9.14	10.58	13.90	10.37	10.84	4.84	5.00	5.26
Ta	0.90	1.18	1.41	1.71	1.20	1.75	1.19	1.50	1.52	1.57
Tl	0.42	0.39	0.50	4.48	0.81	0.99	3.06	0.89	0.74	0.68
Pb 204	37.47	31.24	28.92	41.29	41.23	28.21	31.39	33.43	31.24	29.21
Tl	0.42	0.37	0.50	4.56	0.82	0.95	3.16	0.90	0.74	0.69
Pb 206	37.24	33.16	30.95	41.90	43.53	29.71	34.01	36.13	33.31	30.68
Pb 207	35.25	30.93	28.66	39.48	41.16	28.42	32.91	34.48	31.25	29.11
Pb 208	37.16	32.43	29.62	42.61	42.99	29.89	33.97	35.64	32.45	30.94
Th	15.17	22.25	26.33	22.96	15.84	22.03	21.62	28.10	29.48	30.65
U	2.36	3.39	4.76	2.95	2.17	2.98	3.20	6.50	6.33	6.54

F.

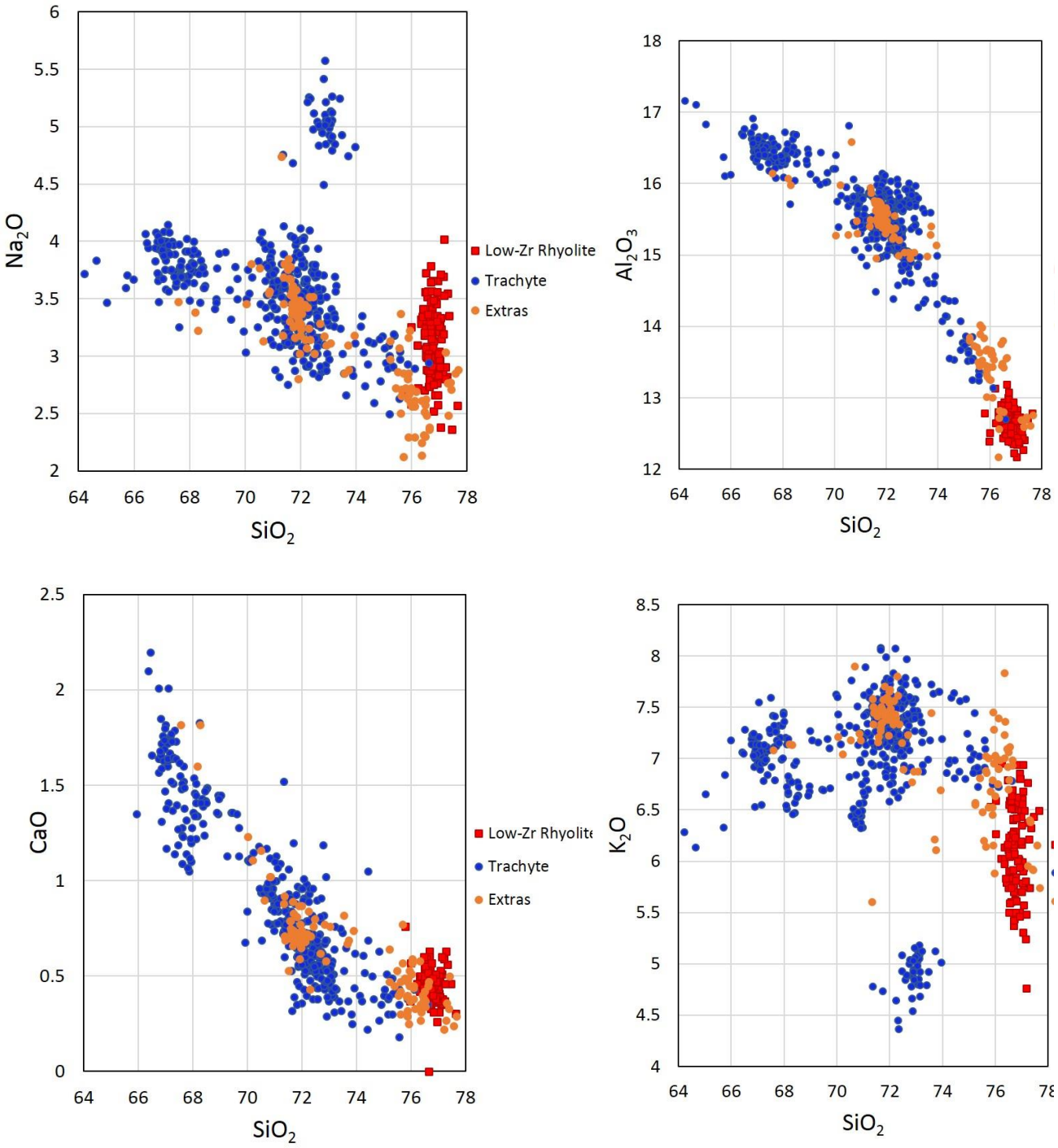
Na2O
SiO2
Low-Zr Rhyolite
Trachyte
Extras
Al2O3
SiO2
CaO
SiO2
Low-Zr Rhyolite
Trachyte
Extras
K2O
SiO2

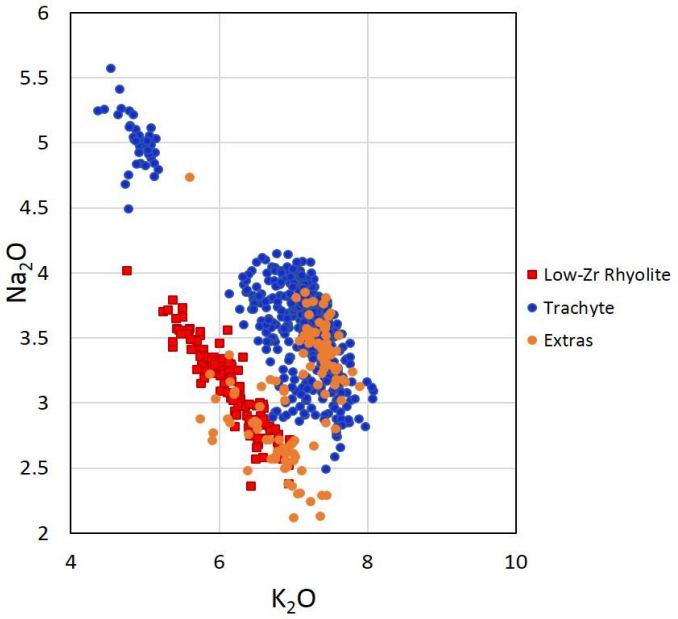
6
5.5
5
4.5
4
3.5
3
2.5
2
4
6
8
10
Na_2O
K_2O
Low-Zr Rhyolite
Trachyte
Extras

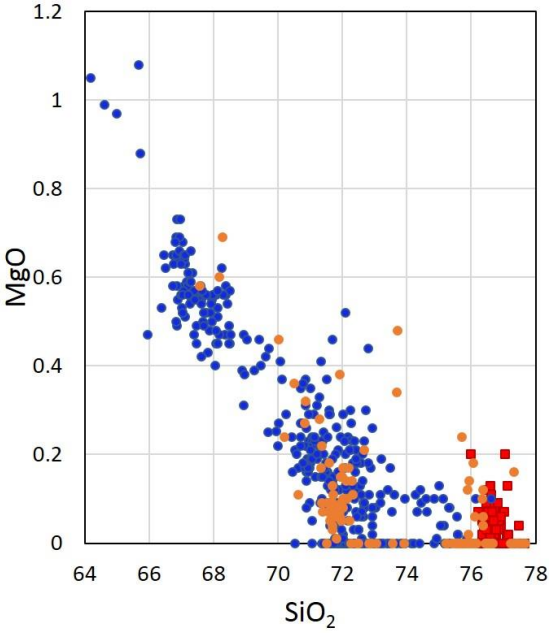
1.2
1
0.8
0.6
0.4
0.2
0
64
66
68
70
72
74
76
78
MgO
SiO_2

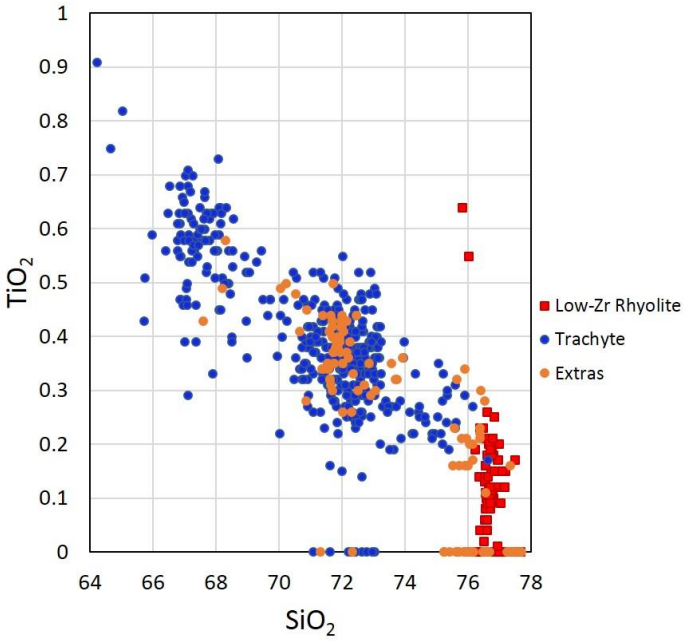
1
0.9
0.8
0.7
0.6
0.5
0.4
0.3
0.2
0.1
0
64
66
68
70
72
74
76
78
TiO_2
SiO_2
Low-Zr Rhyolite
Trachyte
Extras

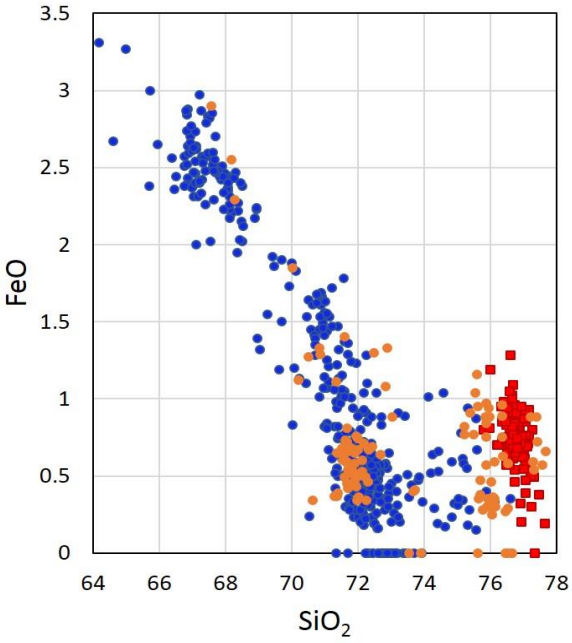
3.5
3
2.5
2
1.5
1
0.5
0
64
66
68
70
72
74
76
78
FeO
SiO_2

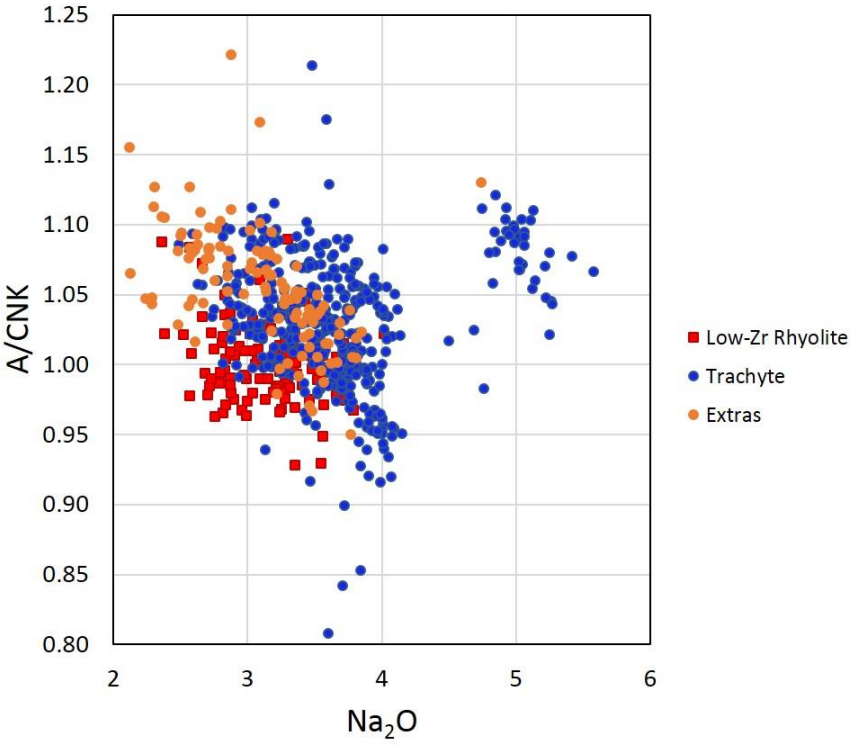
1.25
1.20
1.15
1.10
1.05
1.00
0.95
0.90
0.85
0.80
A/CNK
2
3
4
5
6
Na2O
Low-Zr Rhyolite
Trachyte
Extras

REFERENCES

Anderson, J.L., and Smith, D.R. (1995) The effects of temperature and fO2 on the Al-in-hornblende barometer. *Am Mineral* Vol 80: 549-559

Bachl, C.A., Miller, C.F., Miller, J.S., Faulds, J.E. (2001) Construction of a pluton: Evidence from an exposed cross-section of the Searchlight pluton, Eldorado Mountains, Nevada. *Geological Society of America Bulletin* Vol 113: 1213-1228

Baker, Don R. (1990) Chemical interdiffusion of dacite and rhyolite: anhydrous measurements at 1 atm and 10 kbar. Application of transition state theory, and diffusion in zoned magma chambers. *Contrib Mineral Petrol* Vol 104: 407-423

Baker, Don R. (1991) Interdiffusion of hydrous dacitic and rhyolitic melts and the efficacy of rhyolite contamination of dacitic enclaves. *Contrib Mineral Petrol* Vol 106: 462-473

Barboni, M., Boehnke, P. Schmitt, A.K., Harrison, M.T., Shane, P., Bouvier, A. Baumgartner, L. (2016) Warm storage for arc magmas. *PNAS* Vol 113(49): 13959-13964

Barry, Erin E., Winslow, Heather B., Miller, Calvin F., Claiborne, Lily L., Ferguson, Charles A., Gomez, Carlos D., Varga, Robert J., Lackey, Jade, S. (2015) Magma Chamber Zonation and Eruptive Inversion in the Peach Springs Tuff: Geochemical and Paleomagnetic Evidence. *Geological Society of America, Abstracts with Programs* Vol 47:7, p 538

Bachmann, O. Dungan, M.A., and Lipman, P.W. (2002) The Fish Canyon magma body, San Juan volcanic field, Colorado: Rejuvenation and eruption of an upper-crustal batholith. *Journal of Petrology* Vol 43: 1469-1503

Bachmann, O., and Bergantz, G. (2003) Rejuvenation of the Fish Canyon magma body: A window into the evolution of large-volume silicic magma systems. *Geology* Vol 31: 789-792

Bachmann, O., and Bergantz G.W., (2004) On the origin of crystal-poor rhyolites: Extracted from batholitic crystal mushes. *Journal of Petrology* Vol 45: 1565-1582

Bachmann, O., Bergantz, G. (2008a) Deciphering Magma Chamber Dynamics from Styles of Compositional Zoning in Large Silicic Ash Flow Sheets. *Reviews in Mineralogy & Geochemistry* Vol 69: 651-674

Bachmann, O., Bergantz, G. (2008b) The Magma Reservoirs That Feed Supereruptions. *Elements* Vol 4: 17-21

Bachmann, O., Deering, C.D., Lipman, P.W., Plummer, C. (2014) Building zoned ignimbrites by recycling silicic cumulates: insight from the 1000km^3 Carpenter Ridge Tuff, CO. *Contrib Mineral Petrol* Vol 167: 1025

Bachmann, O. and Huber, C. (2016) Silicic magma reservoirs in the Earth's crust. *American Mineralogist* Vol 101: 2377-2404

Bergantz G.W., Schleicher, J.M., Burgisser A. (2015) Open-system dynamics and mixing in magma mushes. *Nature Geoscience Letters* Vol 8: 793-797

Bindeman, Ilya N., and Valley, John W. (2003) Rapid generation of both high- and low-$\delta^{18}O$, large-volume silicic magmas at the Timber Mountain/Oasis Valley caldera complex, Nevada. *GSA Bulletin* Vol 115: 581-595

Bégué, F., Deering, C.D., Gravley, D.M., Kennedy, B.M., Chambefort, I., Gualda, G.A.R., Bachmann, O. (2014) Extraction, Storage, and Eruption of Multiple Isolated Magma Batches in the Paired Mamaku and Ohakuri Eruption, Taupo Volcanic Zone, New Zealand. *Journal of Petrology* Vol 55: 1653-1684

Blundy, J.D., and Holland, T.J.B. (1990) Calcic amphibole equilibria and a new amphibole-plagioclase geothermometers. *Contrib Mineral Petrol* Vol 104: 208-224

Boehnke, Patrick., Watson, E. Bruce., Trail, Dustin., Harrison, Mark T., Schmitt, Axel K. (2013) Zircon saturation re-revisited. *Chemical Geology* Vol 351: 324-334

Buesch, David C., (1992) Incorporation and redistribution of locally derived lithic fragments within a pyroclastic flow. *Geology Society of America Bulletin* Vol 104: 1178-1193

Buesch, D.C., and Valentine, G.A. (1986) Peach Springs Tuff and volcanic stratigraphy of the southern Cerbat Mountains, Kingman, Arizona. In: Nielson JE, Glazner AF (eds) Cenozoic stratigraphy, structure, and mineralization in the Mojave Desert. *Geological Society of America Guidebook Vol Cordilleran,* Section pp 7-1

Cashman, Katharine V., and Giordano, Guido (2014) Calderas and magma reservoirs. *Journal of Volcanology and Geothermal Research* Vol 288: 28-45

Cooper, Kari M. and Kent, Adam J.R. (2014) Rapid remobilization of magmatic crystals kept in cold storage. *Nature* Vol 506(7489): 480-483

Cooper, Kari M. (2017) What Does a Magma Reservoir Look Like? The "Crystal's-Eye View. *Elements* Vol 13: 23-28

Cooper, George F., Wilson, Colin J.N., Millet, Marc-Alban, Baker, Joel A., Smith, G.C. (2012) Systematic tapping of independent magma chambers during the 1 Ma Kidnappers supereruption. *Earth and Planetary Science Letters* Vol 313-314: 23-33

Deering, C. D., Bachmann, O., Vogel, T.A. (2011) The Ammonia Tanks Tuff: erupting a melt-rich rhyolite cap and its remobilized crystal cumulate. *Earth and Planetary Science Letters* Vol 310: 518-525

Deering, C.D., Bachmann, O. (2010) Trace element indicators of crystal accumulation in silicic igneous rocks. *Earth and Planetary Science Letters* Vol 297: 324-331

Falkner, Claudia M., Miller, Calvin F., Wooden, Joseph L., Heizler, Matthew T. (1995) Petrogenesis and tectonic significance of the calc-alkaline, bimodal Aztec Wash pluton, Eldorado Mountains, Colorado River extensional corridor. *Journal of Geophysical Research* Vol 100: 10,453-10,476

Ferguson, C.A. (2008) Silver Creek caldera, probable source of the Miocene Peach Spring Tuff, Oatman Mining District, Arizona. *Geological Society of America, Abstracts with Programs* 40: 33

Ferguson, C.A., McIntosh, W.C., and Miller, C.F., (2013) Silver Creek caldera – the tectonically dismembered source of the Peach Spring Tuff. *Geology* Vol 41: 3-6

Ferguson, C.A., and Cook, J.P. (2015) Geologic map of the Kingman 7 ½' Quadrangle, Mohave County, Arizona. Arizona Geological Survey Digital Geologic Map DGM-113, scale 1:24,000

Ferguson, Charles (2016) The Peach Spring Tuff, its source caldera, and implications for structural geology of the Colorado River Extensional Corridor. *Arizona Geological Society 2016 Fall Field Trip*

Flansburg, Megan E., Miller, C.F., McDowell, Susanne M., Cribb, Warner J., Bailey, Christopher (2014) Priming For Supereruption: The Hot Pre-Peach Spring Tuff Lava Flows and Peach Spring Tuff Mafic Enclaves, Black Mountains, Arizona. *Geological Society of America, Abstracts with Programs* Vol 46:6 p.512

Flansburg, Megan E. (2015) Priming for Supereruption: the hot pre-Peach Spring Tuff lavas and Peach Spring Tuff magmatic enclaves, Black Mountains, Arizona. *Undergraduate Honors Theses,* College of William and Mary

Frazier, William O., (2013) Petrochemical constraints on generation of the Peach Spring Tuff Supereruption Magma, Arizona, Nevada, California. *M.S. Thesis*, Vanderbilt University

Foley, Michelle L., Miller, Calvin, F., Wulff, Andrew H., McDowell, Susanne M., Covey, Aaron K. (2014) Dynamics of Destabilization: Pumiceous Evidence of Reheated, Remelted, and Remobilized Cumulate from the Base of a Supervolcano Magma Chamber. *Geological Society of America, Abstracts with Programs* Vol 46:6, p.510

Glazner, Allen. Nielson, Jane E., Howard, Keith A., Miller, David M. (1986) Correlation of the Peach Springs Tuff, a large-volume Miocene ignimbrite sheet in California and Arizona. *Geology* Vol 14: 840-843

Gualda, Guilherme A.R., Pamukcu, Ayla S., Ghiorso, Mark S., Anderson Jr, Alfred T., Sutton, Stephen R., Rivers, Mark L. (2012a) Timescales of Quartz Crystallization and the Longevity of the Bishop Giant Magma Body. *PLoS ONE* Vol 7: e37492

Gualda, Guilherme A.R., Ghiorso, Mark S., Lemons, R.V., Carley, Tamara L. (2012b) Rhyolite-MELTS: a modified calibration of MELTS optimized for silica-rich, fluid bearing magmatic systems. *Journal of Petrology* Vol 53: 875-890

Gualda, Guilherme A.R., and Ghiorso, Mark S. (2013) The Bishop Tuff giant magma body: an alternative to the Standard Model. *Contrib Mineral Petrol* Vol 166: 755-775
Gualda, Guilherme A.R., Sutton, Stephen R. (2016) The Year Leading to a Supereruption. *PLoS ONE* Vol 11:7

Hammarstrom, J.M., and Zen, E. (1986) Aluminum in hornblende: An empirical igneous geobarometer. *American Mineralogist* Vol 71: 1297-1313

Harper, Brian E., Miller, Calvin F., Koteas, G.C., Cates, Nicole L., Wiebe, Robert A., Lazzareschi, Daniel S., Cribb, Warner J. (2004) Granites, dynamic magma chamber processes and pluton construction: the Aztec Wash pluton, Eldorado Mountains, Nevada, USA. *Transactions of the Royal Society of Edinburgh: Earth Sciences* Vol 95: 277-295

Harrison, Mark T., Watson, Bruce, E. (1984) The behavior of apatite during crustal anataxis: Equilibrium and kinetic considerations. *Geochemica et Cosmochimica Acta* Vol. 48: 1467-1477

Hildreth, W. (1981) Gradients in silicic magma chambers: Implications for lithospheric magmatism. *Journal of Geophysical Research* Vol 86(B11): 10153-10192

Hildreth, W.S. (2004) Volcanological perspectives on Long Valley, Mammoth Mountain, and Mono Craters: Several contiguous bus discrete systems. *Journal of Volcanology and Geothermal Research* Vol 136: 169-198

Hildreth, Wes and Wilson, Colin J.N. (2007) Compositional zoning of the Bishop Tuff. *Journal of Petrology* Vol 48: 951-999

Hillhouse, J.W., and Wells, R.E. (1991) Magnetic fabric, flow directions, and source area of the lower Miocene Peach Springs Tuff in Arizona, California, and Nevada. *Journal of Geophysical Research* Vol 96: 12,443-12,460

Holland, T.J.B., and Blundy, J.D (1994) Non-ideal interactions in calcic amphiboles and their bearing on amphibole-plagioclase thermometry. *Contrib Mineral Petrol* Vol 116: 433-447
Huber, C., Bachmann, O., Dufek, J. (2011) Thermo-mechanical reactivation of locked crystal muses: melting-induced fracturation and assimilation processes in magmas. *Earth and Planetary Science Letters* Vol 304: 443-454

Huber, C., Bachmann, O., Dufek, J. (2012) Crystal-poor vs. crystal-rich ignimbrites: a competition between stirring and reactivation. *Geology* Vol 40: 115-118

Kennedy, Ben. Stix, John (2007) Magmatic processes associated with caldera collapse at Ossipee ring dyke, New Hampshire. *GSA Bulletin* Vol 119: 3-17

Koyaguchi, Takehiro and Kaneko, Katsuya (2000) Thermal evolution of silicic magma chambers after basalt replenishments. *Transactions of the Royal Society of Edinburgh: Earth Sciences* Vol 91: 47-60

Mahood G.A. (1990) Second reply to comment of R.S.J. Sparks, H.E. Huppert, and C.J.N. Wilson on "Evidence for long residence times of rhyolitic magma in the Long Valley magmatic system: the isotopic record in the precaldera lavas of Glass Mountains." *Earth and Planetary Science Letters* Vol 99: 395-399

McCracken, R., Miller, C.F., Buesch, G., Gualda, G.A.R., Covey, A. (2012) Glass and mineral analyses from the first deposits of Peach Spring Supereruption (SW USA) illuminate initial tapping of a zoned magma chamber. *AGU Annual Fall Meeting,* Abstract V31C-2803

McDowell, Susanne M., Miller, Calvin F., Mundil, R., Ferguson, Charles A., Wooden, Joseph L. (2014) Zircon evidence for a ~200 k.y. supereruption-related thermal flare-up in the Miocene southern Black Mountains, western Arizona, USA. *Contrib Mineral Petrol* Vol 168:1031

McDowell, Susanne M., Overton, Sarah., Fisher, Christopher M., Frazier, William O., Miller, Calvin F., Miller, Jonathan S., Economos, Rita C. (2016) Hafnium, oxygen, neodymium, strontium, and lead isotopic constraints on magmatic evolution of the supereruptive southern Black Mountains volcanic center, Arizona, U.S.A.: A combined LASS zircon-whole-rock study. *American Mineralogist* Vol. 101 311-327

Miller, Calvin F., Wark, David A. (2008) Supervolcanoes and their Explosive Supereruptions. *Elements.* Vol 4: 11-16, DOI: 10.2113/GSELEMENTS.4.1.11

Miller, Calvin, F. (2016) Eruptible magma. *PNAS* Vol 113: 13941-13943

Mutch, E.J.F., Blundy, J.D., Tattich, B.C., Cooper, F.J., Brooker, R.A. (2016) An experimental study of amphibole stability in low-pressure granitic magmas and a revised Al-in-hornblende geobarometers. *Contrib Mineral Petrol* 171:85

Nielson, J.E., Lux, D.R., Dalrymple, G.B., and Glazner, A.F. (1990) Age of the Peach Springs Tuff, Southeastern California and Western Arizona. *Journal of Geophysical Research* Vol 95: 571-580

Padilla, Abraham, J., and Gualda, Guilherme A.R. (2016) Crystal-melt elemental partitioning in silicic magmatic systems: An example from the Peach Spring Tuff high-silica rhyolite, Southwest USA. *Chemical Geology* Vol 440: 326-344

Pallister, J.S., Hoblitt, R.P., Reyes, A.G. (1992) A Basalt trigger for the 1991 eruption of Pinatubo volcano? *Nature* Vol 356: 426-428

Pamukcu, Ayla S., Carley, Tamara L., Gualda, Guilherme A.R., Miller, Calvin F., Ferguson, Charles A. (2013) The Evolution of the Peach Spring Giant Magma Body: Evidence from Accessory Mineral Textures and Compositions, Bulk Pumice and Glass Geochemistry, and Rhyolite-MELTS Modeling. *Journal of Petrology* Vol 54, No 6: 1109-1148

Pamukcu, Ayla S., Gualda, Guilherme A.R., Ghiorso, Mark S., Miller, Calvin F., McCracken, Reba G. (2015) Phase-equilibrium geobarometers for silicic rocks based on rhyolite-MELTS—Part 3: Application to the Peach Spring Tuff (Arizona-California-Nevada, USA). *Contrib Mineral Petrol* 169:33

Rampino, M.R., and Self, S. (1992) Volcanic winter and accelerated glaciation following the Toba super-eruption. *Nature* Vol 359: 50-53

Roche, O., Buesch, D.C., and Valentine, G.A., (2016) Slow-moving and far-travelled dense pyroclastic flows during the Peach Spring super-eruption. *Nature Communications* Vol 7: 1-8

Sliwinski, J.T., Bachmann, O., Dungan, M.A., Huber, C., Deering, C.D., Lipman, P.W., Martin, L.H.J., Liebske, C. (2017) Rapid pre-eruptive thermal rejuvenation in a large silicic magma body: the case of the Masonic Park Tuff, Southern Rocky Mountain volcanic field, CO, USA. *Contrib Mineral Petrol* Vol 172:30

Sparks, S.R.J., Sigurdsson, H., Wilson, L. (1997) Magma mixing-mechanism for trigger acid explosion eruptions. *Nature* Vol 5609: 315-318

Sparks, R.S.J., Self, S., Grattan, J.P., Oppenheimer, C., Pyle, D.M., Rymer, H. (2005) Super-eruptions: global effects and future threats. *Report of a Geological Society of London Working Group*, The Geological Society, London, 24 pp

Tramontano, S., Gualda, G.A.R., Ghiorso, M.S. (2017) Internal triggering of volcanic eruptions: tracking overpressure regimes for giant magma bodies. *Earth and Planetary Science Letters* Vol 472: 142-151

Varga, R.J., Faulds, J.E., Snee, L.W., Harlan, S.S., Bettison0Varga, L., (2004) Miocene Extension and Extensional Folding in an Anticlinal Segment of the Black Mountains Accommodation Zone, Colorado River Extensional Corridor, Southwestern USA. *Tectonics* Vol 23. No. 11

Watson, Bruce E., Harrison, Mark T. (1983) Zircon saturation revisited: temperature and composition effects in a variety of crustal magma types. *Earth and Planetary Science Letters* Vol 64: 295-304

Wilson, Colin J.N. (2008) Supereruptions and Supervolcanoes: Processes and Products. *Elements* Vol 4: 29-34

Wolff, J.A., and Ramos, F.C. (2003) Pb isotope variations among Bandelier Tuff feldspars: No evidence for a long-lived silicic magma chamber. *Geology* Vol 31: 533-536

Wolff, J.A., Ellis, B.S., Ramos, F.C., Starkel, W.A., Boroughs, S., Olin, P.H., and Bachmann, O. (2015) Remelting of cumulates as a process for producing chemical zoning in silicic tuffs: A comparison of cool, wet, and hot, dry rhyolitic magma systems. *Lithos* Vol 236-237: 275-286

Young, R.A., and Brennan, W.J. (1974) Peach Springs Tuff: It's bearing on structural evolution of the Colorado Plateau and development of Cenozoic drainage in Mohave County, Arizona. *Geological Society of America Bulletin* Vol. 85: 83–90